Università degli Studi di Catania

Dottorato di Ricerca in Fisica – XXII ciclo.

CLAUDIO CHIBBARO

Mono-crystalline Silicon Photovoltaic Cells: Innovative Technologies toward low Series Resistance

PhD Thesis

PhD Coordinator:
Prof. Francesco Riggi

Tutor:
Prof. Pietro Baeri

Contents

Introduction

An increasing consensus of scientific opinion now agrees that occurring global climate change is caused in large part by human activities and, if left unopposed, it will have catastrophic environmental consequences. The scientific evidence on the need for urgent action on the problem of global warming has today become realistic and convincing. This evidence is reflected also in the conclusions of the Intergovernmental Panel on Climate Change (IPCC), an U.N. institution of more than 1000 scientists providing information to policy makers.

To keep rising temperatures within acceptable limits, mankind needs to significantly reduce, as soon as possible, greenhouse gas emissions (in particular carbon dioxide CO_2) related especially to the present dependence on fossil fuels in energy production. Thus, climate change requires a global energy revolution based on new solutions in the way that energy is produced and distributed. Future solutions are already available today and lie in an intensive use of existing renewable sources.

Inside this context, photovoltaic energy represents a realistic accessible opportunity to accelerate the end of this Petroleum Age and to satisfy the energy requirement of our society by means of a sustainable technology which offers several advantages, in spite of few and acceptable drawbacks.

The role of the photovoltaic energy inside the big picture of the social, economical and environmental questions regarding the global energy production is illustrated in the **chapter 1**.

The resistance offered today to the development of the photovoltaic energy production on global scale resides mainly in its high costs. Although a photovoltaic module gives back in only few years the energy used to be manufactured, at the present it requires some tens of years to return economically its cost. The building cost of a photovoltaic power plant is much expensive in comparison with that one of an equivalent traditional thermal plant. For example, the cost of a portable oil-stoked electric generator with an output power of 1KW is about one order of magnitude less of the price of a power-correspondent photovoltaic module.

Today, comprehensive cost of energy produced by a conventional silicon wafer-based PV cell is about 2÷5$/Watt. So, in respect of the price of energy traditionally produced by fossil fuels, photovoltaic does not appear economically cost-effective in the short-term.

However, removing the costs related to energy source supplying, the economical benefits connected to solar energy could be observed as time goes by. In fact, considering that a photovoltaic device provides electric power within the time of about twenty years (its common lifetime), energy produced by a photovoltaic module having a power peak of 1W during its entire life is about 30KWh. From this point of view, the price of energy production by photovoltaic generators becomes few cents of dollars per KWh. Adding the costs of modules

manufacturing and installation, of the conversion from direct to alternate current and of system maintenance, a comprehensive price of about 10 cents of dollar per KWh is finally obtained.
Others financial considerations, concerning invested capital time return, profits variation due to inflation and so on must be obviously taken into account to privates' investments. From these, the need of government financial supports to validate economical investments in photovoltaic energy production rises.
Nevertheless, a complete estimation of the global costs related to energy production by burning fossils including also environmental and healthy effects (normally not included in standard economical indexes), makes photovoltaic a real and actual reasonable alternative to conventional technologies. Unfortunately, the irresponsible modern logic of capital short-term profit imposes a competition strictly connected to the economical standard parameters which do not evaluate long-term consequences.
Therefore, photovoltaic energy manufacturer today are hardly working in order to reduce considerably the price of produced electric power. Even if technological developments suggest that a target cost of few cents per Watt produced by photovoltaic cells could be reached in the next future by new emerging photovoltaic technologies, first generation devices (single junction, wafer-based cells) still represent the majority of available photovoltaic equipments on the market and crystalline silicon is the most common material used to produce the cells.
The working principles and the electrical characteristic of a single junction silicon photovoltaic cell are explained in **chapter 2**.
The electric performance of a photovoltaic cell depends on several parameters, often interdependent between themselves. Whatever should be the structure of a cell, the optimization of its structural parameters is necessary to get the higher achievable efficiency. With this purpose, a simulation program of photovoltaic devices electrical behaviour has been developed for exploring the full range of silicon wafer-based cells design options to find the best manufacturing process flow. The realized simulation program has been used to analyze the most important parameters determining silicon photovoltaic cell performance, with the purpose of improving physical and geometrical factors influencing device efficiency.
The simulation program and the relative results are illustrated inside **chapter 3**.
From an industrial prospective, the use of a simulation program is an indispensable R&D technique because it provides several advantages in terms of both cost saving and response time velocity. The primary interest of the main industries engaged in the photovoltaic field is now to remain inside the production sphere of the most common first generation cells, with the principle purposes of finding novel design alternatives directed toward product quality, manufacturing cost reduction and energy saving.
In **chapter 4** a real silicon photovoltaic cell industrial manufacturing process is described. The illustrated manufacturing line has been planned and realized in

Catania, by means of a collaboration between Meridionale Impianti (M.I.) S.p.A., UniCt (University of Catania), Advanced Technology Solutions (A.T.S.) S.r.l. and Meridionale Impianti Welding Technology (M.I.W.T) S.r.l.. The project, financed by the Technologic Innovation Fund (F.I.T.) is entitled "*R&D program directed toward the realization of novel high efficiency photovoltaic cells and modules*".

Data obtained by research and simulation activities have permitted to create a prototype productive line, aimed at production of high efficiency and low-cost first generation silicon photovoltaic cells. In order to reach higher quality at lower cost, some innovative solutions have been adopted inside the manufacturing flow to optimize the process steps. The principal innovation concerns the deposition of a thin layer of transparent conductive oxide on cell surface as both front contact and passivation. The deposited film has been optically and electrically characterized with the purpose of getting the best process parameters set up. An evaluation of its effects on cell performance has been also evaluated.

Results are reported again in **chapter 4**.

One of the most important improvement obtained by using a transparent conductive oxide as surface coating was the decreasing of electrical parasitic resistance due to front contact. The measurement of these very low resistances (in the order of few mΩ) involved several problems regarding measures accuracy and repeatability. The experimental evaluation of such resistance values demonstrated the inadequacy of standard measurement methods because of some their intrinsic limits.

Consequently a new procedure has been developed and realized to overcome these limits. The description of this novel measurement procedure and a series of tests to verify its reliability are reported in **chapter 5**.

1. The Role of Photovoltaic inside the Global Energy Production

1.1 - ENERGY ISSUE OVERVIEW

It is well known that people quality of life is directly connected to energy availability. Various statistical indexes show the correlation between energy consumption and human average lifetime, death rate, life expectancy and educational achievement. As the most versatile form of energy we have is electricity, access to and consumption of electricity is closely related with quality of life. Figure 1.1 shows, for example, the Human Development Index (H.D.I.) for over 60 countries (including about 90% of the Earth's population) as a function of annual per capita electricity use [1].
The H.D.I. measures inter-country development levels on the basis of three so-called "deprivation" indicators: life expectancy, adult literacy and the logarithm of purchasing power.

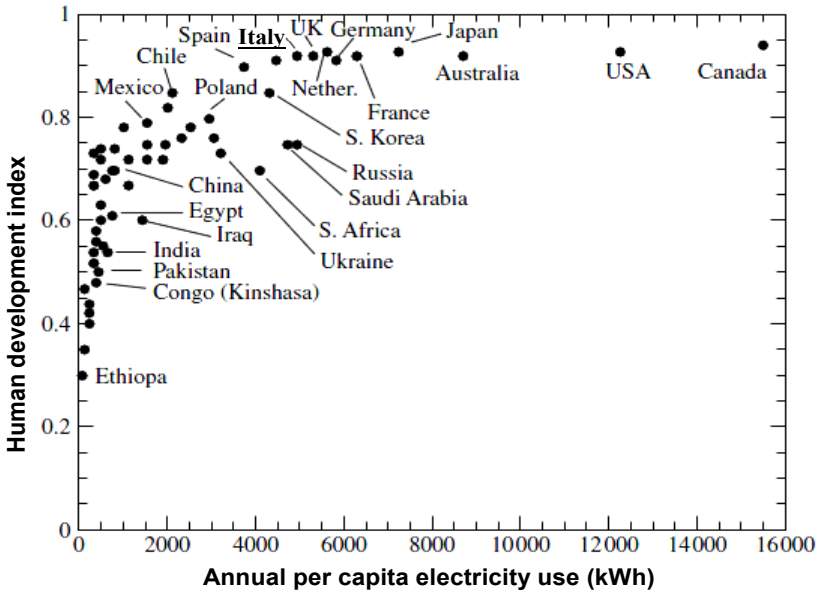

Figure 1.1 Human development index (H.D.I.) versus per capita kWh usage. [1]

The growing aspirations of an increasing world population are expected to enlarge world energy demand, even if strong attempts have been made to improve energy efficiency. To progress the quality of life in many countries, as measured by their H.D.I., global electricity consumption demand will raise in

the next future by factors of 10 or more, from a few hundred to a few thousand kilowatt-hrs (KWh) per year.
As shown in figure 1.2, the present annual world consumption increasing is about 3%: in 1996 world energy consumption was ~$1.1 \cdot 10^5$TWh while ten years later was ~$1.4 \cdot 10^5$TWh [2]. The International Energy Outlook 2009 (IEO2009) developed by the U.S. Energy Information Administration (E.I.A.) reports a scenario in which total world consumption of marketed energy is projected to increase by 44% from 2006 to 2030, if current laws and policies will remain unchanged throughout the entire period. The largest increase in energy demand is expected for the developing countries, dominated by Chinese and Indian economies.

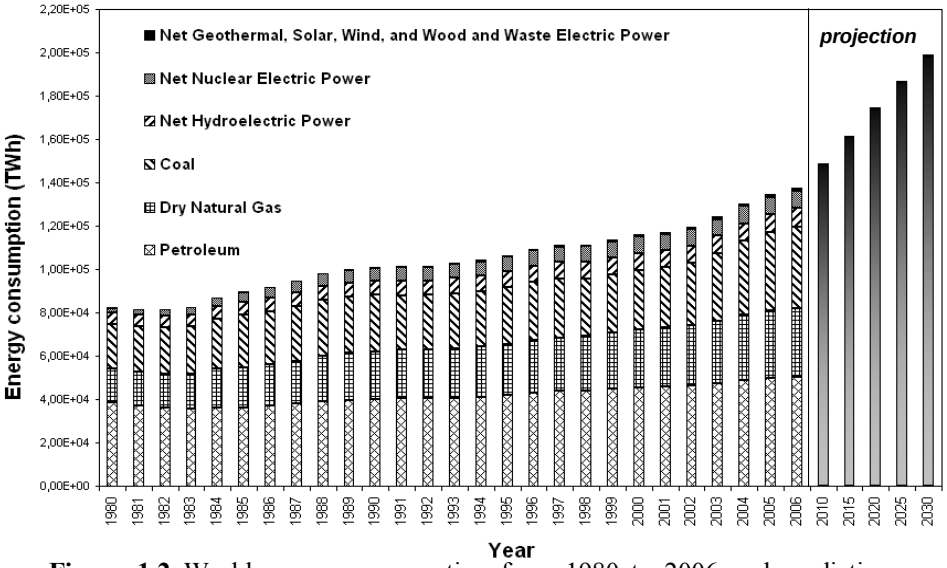

Figure 1.2 World energy consumption from 1980 to 2006 and predictions. Total world consumption of marketed energy is projected to increase by 44% from 2006 to 2030. [2]

One of the most critical question mankind has to answer quickly at present, is how to satisfy this energy request. In fact, especially during the last few years, increasing demand and growing consumption has posed several challenges: ensuring sufficient, reliable and safe energy supplies, develop new energy sources (making adequate investments in new technologies) and, above all, dealing with environmental effects.
Therefore, energy issue occupies today a central role in global economy and countries development.

1.1.1 – Fossil fuels

Figure 1.2 shows that majority of energy production today is entrusted to fossil fuels: chemical energy stored in fossil fuels (such as coal, fuel oil, natural gas or

oil shale) is converted at first into thermal energy by burning process, then in mechanical energy and, finally, in electricity. The conversion efficiency of this process chain has obtained a continuous improvement and now globally it is about 40%. Electric energy production by fossil fuels today is the less expensive and covers more than half of energy world demand.
On the other hand, this kind of energy is polluting, non-renewable, non-sustainable and finally not widely available.
Figure1.3 shows the world proved petroleum reserves known at the end of 2008. On the base of actual consumption, according to oil companies' reports, is estimated that petroleum could end within next 50 years, natural gas within 60 years and coal within about 200 years [3].

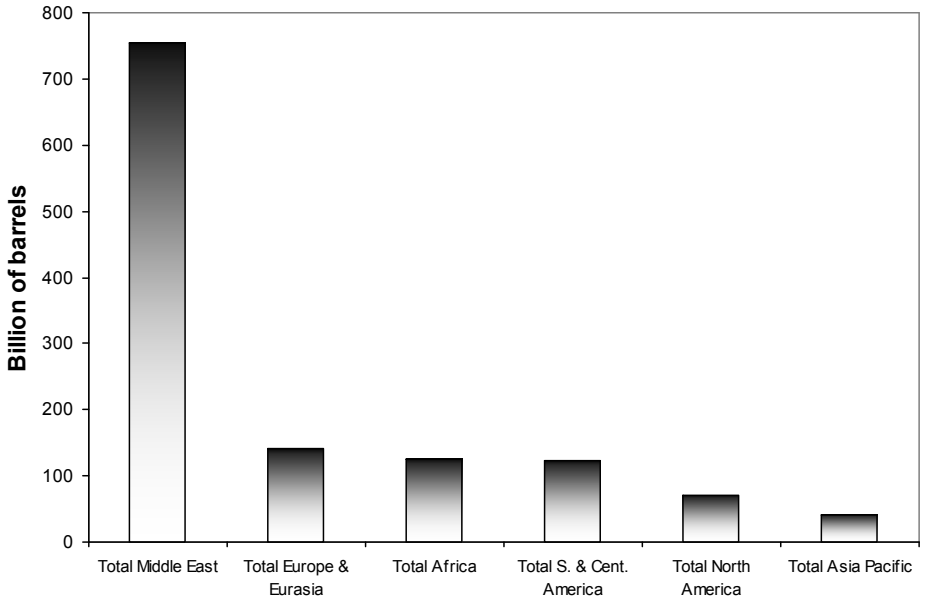

Figure 1.3 World proved petroleum reserves at end 2008. [3]

Nevertheless, these evaluations are optimistic because do not take in account three important factors: real entity of existent reserves, periodical production increment and difficulty in fossil extraction from exhaustion deposits. Resources valuation is not an exact science and every assertion must be provided with a probability degree. OPEC members often enlarge their reports because fossil fuel exportable quantity is proportional to reserves.
Realistic valuations report that global petroleum reserve amount to about 1000 billion of barrels.
Moreover, it's important to note that a critical phase that could destabilize present consumption rate of fossil fuels will begin not only when reserves will be exhaust, but when production will be reduced. According to the M.King Hubbert model, for any given geographical area, the rate of petroleum

production tends to follow a bell-shaped curve with a peak followed by a decreasing. Petroleum annual production from 1930 and Hubbert predictions are shown in figure 1.4 [4].

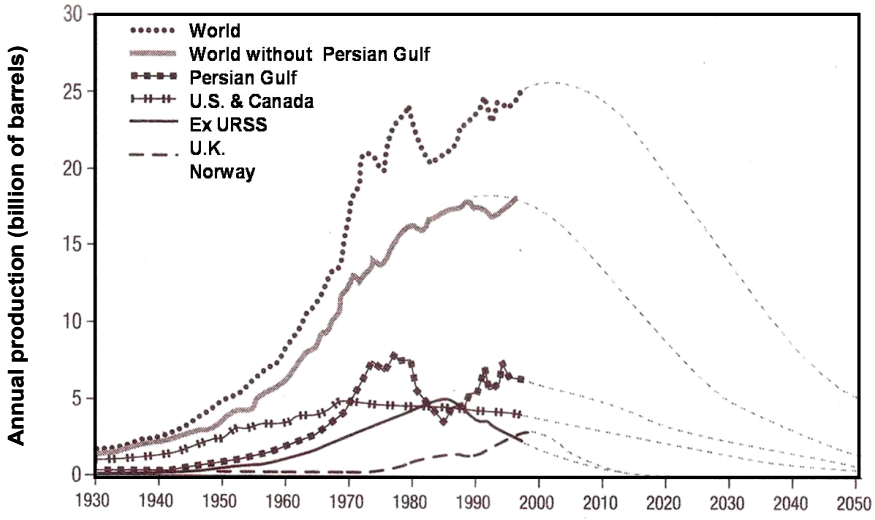

Figure 1.4 World petroleum productions (with prediction). According to M.King Hubbert model, for any given geographical area the rate of petroleum production tends to follow a bell-shaped curve with a peak followed by a decreasing. [4]

For every area, peak is expected to occur before 2015. At the present, this decreasing has not been still observed because technological improvements have allowed exploiting offshore oilfield more and more deep and fossil deposits with less quality.
However, only few deposits under the ocean abyss and the Antarctic sea remain to be explored and new important deposits improbably will be located. Yet, the recent environmental disaster due to the explosion of the BP platform "Deepwater Horizon" occurred in the Gulf of Mexico has underlined the risks connected to offshore oil extraction.
As shown in figure 1.5 natural reserves appear in evident decline: 80% of petroleum produced today comes from deposits discovered before 1973 and, for this reason, already widely exploited [4].

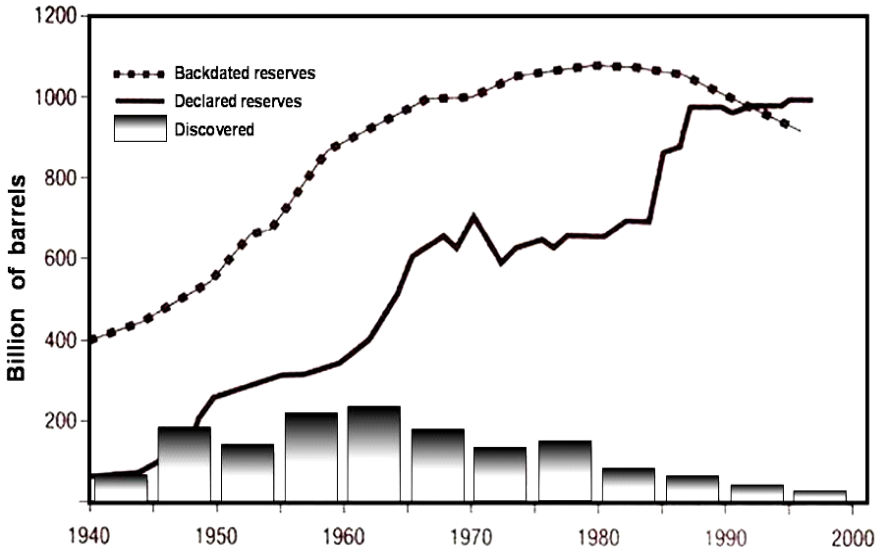

Figure 1.5 World petroleum reserves. 80% of petroleum produced today comes from deposits discovered before 1973. [4]

In spite of that, petroleum global demand is growing continuously and its consumption is increasing, especially in developing countries. Once exceeded the peak of figure 1.4, petroleum production will reduce and exporting countries will be forced to increase prices. So, if petroleum demand will not reduce, in the next future prices will grow very quickly and fossil fuel energy production will not be still economically favourable.
Economical long-term analysis and environmental effects (as will be described inside paragraph 1.2) impose to accelerate the end of this Petroleum Age in order to investigate new kinds of energy production.

1.1.2 – Nuclear power

Today, the most used alternative to fossils fuels is the nuclear energy: in 2009 about 15% of the world's electricity came from nuclear power. This kind of electric energy production is based on controlled nuclear reaction and the most widely used fuel by nuclear plants is Uranium-235, suitable for nuclear fission because its atoms are easily split apart. Even if uranium is quite common, U-235 is relatively rare because less of 1% of uranium ore contains U-235. So, to be used in energy production, uranium must be processed ("enrichment") to increase the concentration of U-235.
The cost of electricity from nuclear energy is somewhat higher than the cost of electricity by fossils. Amount of the cost comes not from the fuel source but from building and monitoring the plant: the economics of nuclear power are primarily influenced by the high initial investment required to construct a plant. To pay off this cost, it is more profitable to run the plants as long as possible, or

construct additional reactor blocks inside existing facilities. In 2009, new nuclear power plant construction costs were rising faster than the costs of other types of power plants. In actual market, nuclear power does not appear cost competitive with coal and natural gas.

Today, around the world, nuclear energy production is attracting new interest as countries need to increase the diversity of their energy supplies and improve energy availability, providing alternative to fossil fuels. However, there is considerable uncertainty associated with nuclear power. Uranium is not a renewable source (like fossils) although it is a common metal found in rocks all over the world. It is considered that at actual utilization rate, Uranium reserves will exhaust in about 100÷200 years [5].

In addition, nuclear energy have some intrinsic unresolved issues that restrict its future development. These issues concern above nuclear weapons proliferation, radioactive waste disposal and plant safety.

Manufacturing a nuclear bomb requires fissile material, either Uranium-235 or Plutonium-239. Most nuclear reactors use Uranium as a fuel and produce Plutonium during their operation. It is practically impossible to protect a large reprocessing plant to prevent the diversion of Plutonium to nuclear weapons. A small-scale Plutonium separation plant can be built in four to six months, so any country with an ordinary reactor can produce nuclear weapons relatively quickly.

The result is that nuclear power and nuclear weapons have grown up together. Since international controls on nuclear proliferation began, Israel, India, Pakistan and North Korea have all obtained nuclear weapons, demonstrating the link between civil and military nuclear power. Also the United Nations Intergovernmental Panel on Climate Change (representing the work of 2,500 scientists from more than 130 countries) has notified that the security danger of trying to face climate change with a global fast reactor programme (using Plutonium fuel) "would be colossal". IPCC specifies that to solve the twin questions of climate change and nuclear weapons proliferation it is necessary to phase out nuclear power and promote sustainable energy [6].

Concerning the issue of radioactive waste disposal, the supporter of nuclear industry declare that nuclear waste can be 'disposed' by burying it deep underground. This method is a false solution, because it does not guarantee forever the isolation of radioactive material from the environment: a deep dump only slows down the release of radioactivity into the environment. The most dangerous waste is the highly radioactive waste (or spent) fuel removed from nuclear reactors, which stays radioactive for hundreds of thousands of years. There are about 270,000 tonnes of spent nuclear waste fuel in storage, much of it at reactor sites. Spent fuel is accumulating at around 12,000 tonnes per year, with approximately a quarter of that going for reprocessing (process that leaves behind a highly radioactive liquid waste). No country in the world has a definitive solution for high level waste. The only real solution is to stop producing the waste.

A nuclear and radiation accident is defined by the International Atomic Energy Agency as "an event that has led to significant consequences to people, the environment or the facility. Examples include lethal effects to individuals, large radioactivity release to the environment, or reactor core melt." [7]. Windscale (1957), Three Mile Island (1979), Chernobyl (1986) and Tokaimura (1999) are only a few of the hundreds of nuclear accidents which have occurred to date. A nuclear chain reaction must be kept under control and dangerous radiation must be contained within the reactor with radioactive products isolated from humans and carefully managed. Nuclear reactions generate high temperatures, and fluids used for cooling are often kept under pressure. Together with the intense radioactivity, these operating conditions make the reactor a very complex tool to manage, where to prevent every potential accident type (coolant losses, equipments failure, human errors, etc.) is impossible.

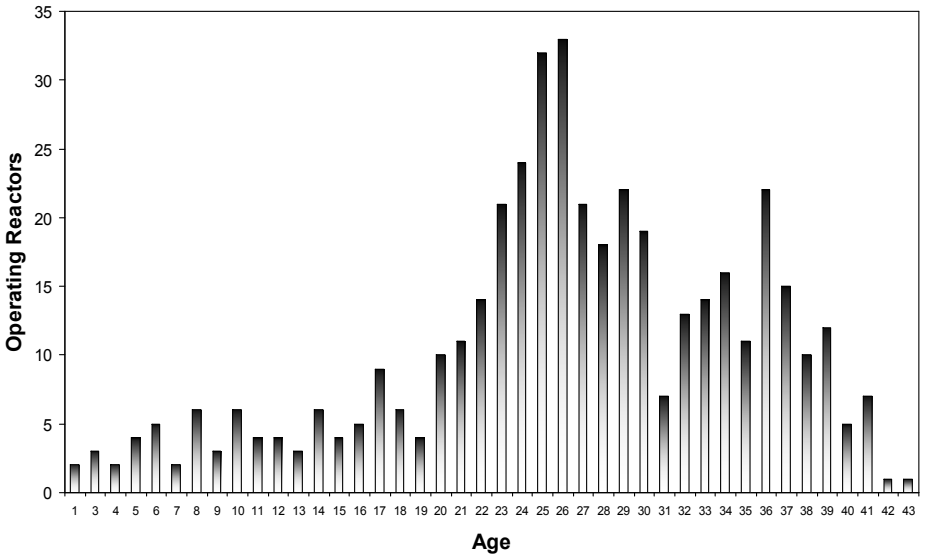

Figure 1.6 Nuclear operating reactors by age. Most of the world's reactors are more than 20 years old. Many utilities are attempting to extend their life from the about 40 years they were originally designed for, to around 60 years. [5]

As shown in figure 1.6, most of the world's reactors are more than 20 years old and, consequently, they are more subjected to age related failures. Many utilities are attempting to extend their life from the about 40 years they were originally designed for, to around 60 years posing new risks [5] [7].
Table 1.1 summarize costs and some limitations and externalities of fossils and nuclear power generation: traditional resources are finite, polluting, and not long-term economically favourable. So it seems clear that to face electricity consumption increasing requirement there is the necessity to find alternative energetic sources, renewable and easily available [2] [8].

Table 1.1 - Traditional Power Generation		
Method	**Cents/kWh**	**Limitations and Externalities**
Gas Currently supplies around 15% of the global electricity demand.	3.9 - 4.4 Cents$/kWh	A relatively high percentage of the cost/KWh is derived from the cost of the fuel. Due to the current (and projected future) upwards trend in gas prices, there is uncertainty around the cost / KWh over the lifetime of plants. Gas burns more cleanly than coal, but the gas itself (largely methane) is a potent greenhouse gas.
Coal Currently supplies around 38% of the global electricity demand.	4.8 - 5.5 Cents$/kWh	To build new coal plants in the developed world is increasingly difficult due to environmental requirements governing the plants. The supply of coal is plentiful, but the coal generation method is perceived to make a larger contribution to air pollution than the rest of the methods combined.
Nuclear Currently supplies around 24% of the global electricity demand.	11.1 - 14.5 Cents$/kWh	Political difficulties in using nuclear in some nations. Risk of widespread (and potentially lethal) contamination upon containment failure. Fuel is plentiful, but problematic. Waste disposal remains a significant problem, and de-commissioning is costly.

1.2 - ENVIRONMENTAL EFFECTS AND GLOBAL WARMING

Production and consumption of any type of energy have environmental consequences. Effects of this kind of human activities are well known for a lot of time, but only in last decades the risks connected to these effects have been realized.
During most of human history (and certainly before human beings emerged as a dominant species in the whole world) all climate changes were the direct result of only natural forces. This condition changed with the start of the industrial revolution, when new agricultural and industrial practices began to modify atmospheric chemical composition altering the global climate.
Population growth, deforestation, factory farming, and the widespread use of fossil fuels are creating an excess of greenhouse gases in the atmosphere, contributing to a more and more evident global climate changing. Evidence of this change is shown in figure 1.7 where Carbon dioxide (CO_2) variations from 400 thousand of years ago to today (fig.1.7a) and temperature change from 1900 to 1990 (fig.1.7b) are plotted [8].

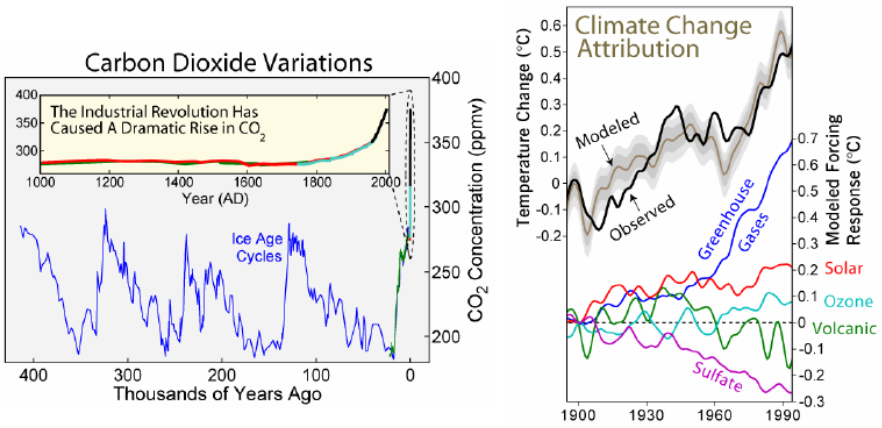

Figure 1.7 a) World CO_2 variations from 400 thousand of years ago to today. b) Temperature changes from 1900 to 1990. Most of the observed temperature increase since the middle of the 20th century was caused by increasing concentrations of greenhouse gases resulting from human activities. [8]

Global surface temperature increased 0.74±0.18°C within the 20th century, in accordance with the greenhouse gas concentration trend. This observed increase in the average temperature of the Earth's near-surface air and oceans since the mid-20th century is defined "global warming".

The IPCC report published in February 2007 stated that human activity "very probably" has been the primary cause of global warming since 1950. The IPCC report illustrates that human activity has been a major contributor to climate change since the start of the industrial revolution in the mid-1700s and that most of the observed temperature increase since the middle of the 20th century was caused by increasing concentrations of greenhouse gases resulting from human activity. The report concludes that variations in natural phenomena such as solar radiation and volcanoes produced most of the warming from pre-industrial times to 1950 and had a small cooling effect after. These basic conclusions have been supported by more than 40 scientific societies and academies of science, including all of the national academies of science of the major industrialized countries.

Climate model projections summarized in the latest IPCC report indicate that the global surface temperature will probably rise from 1.1 to 6.4 °C during the twenty-first century. The uncertainty in this estimate arises from the use of models with differing sensitivity to greenhouse gas concentrations and the use of differing estimates of future greenhouse gas emissions. Most studies focus on the period up to the year 2100. However, warming is expected to continue beyond 2100 even if emissions stop, because of the large heat capacity of the oceans and the long lifetime of Carbon dioxide in the atmosphere [6] [8].

An increase in global temperature will cause sea levels to rise and will change the amount and pattern of precipitation, probably including expansion of

subtropical deserts. The continuing retreat of glaciers, permafrost and sea ice is expected, with warming being strongest in the Arctic. Other possible effects include increases in the intensity of extreme weather events, species extinctions, and changes in agricultural yields.
Political and public debate continues regarding climate change, and what actions to take in response. Most national governments have signed and ratified the Kyoto Protocol aimed at reducing greenhouse gas emissions. In figure 1.8 the annual Carbon emission by Region, from 1800 to 2000 is shown [8].

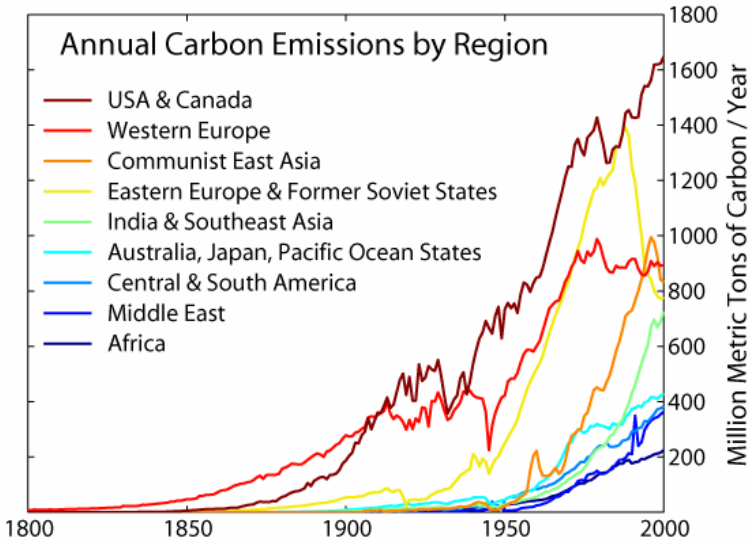

Figure 1.8 Annual Carbon emission (fossil fuels burning) by Region. [8]

Consequently renewed attention is now given to the development and utilization of renewable sources of energy in response to the growing interest in climate change and secure and affordable supplies of energy for economic and social development. If expected growing world energy demand will be met only with fossil fuels, carbon dioxide emissions will increase considerably, not decreasing as implied by the IPCC report.

1.3 – RENEWABLE ENERGY

Renewable energy is defined as energy generated from natural resources (such as sunlight, wind, rain, tides and geothermal heat) which are renewable (naturally replenished constantly) not depleted, and that minimize environmental impact.
Renewable energy flow to the Earth's land surface is thousands of times greater than mankind's present rate of total energy use. The use of only a small fraction

of this resource would provide humanity with an alternative and environmentally path to meet future energy needs. The question is if this flow of energy can be converted to electricity at acceptable costs in a sustainable manner. Table 1.2 illustrates costs, limitations and externalities of conventional renewable power generation [2] [6] [8].

Table 1.2 - Conventional Renewable Power Generation

Method	Cents/kWh	Limitations and Externalities
Wind Currently supplies approximately 1.4% of the global electricity demand. Wind is considered to be about 30% reliable.	4.0 - 6.0 Cents/kWh	Wind is currently the only cost-effective alternative energy method, but has several problems. Wind farms are highly subject to lightning strikes, have high mechanical fatigue failure, are limited in size by hub stress, do not function well, if at all, under conditions of heavy rain, icing conditions or very cold climates, and are noisy and cannot be insulated for sound reduction due to their size and subsequent loss of wind velocity and power.
Geothermal Currently supplies approximately 0.23% of the global electricity demand. Geothermal is considered 90-95% reliable.	4.5 – 30 Cents/kWh	New low temperature conversion of heat to electricity is likely to make geothermal substantially more plausible and less expensive. Generally, costs diminish as plant dimension increases. Cost also depends on the depth to be drilled and on the temperature at the depth. The higher the temperature, the lower the cost per KWh. Cost may also be affect by where the drilling is to take place as concerns distance from the grid and another factor may be the permeability of the rock.
Hydro Currently supplies around 19.9% of the global electricity demand. Hydro is considered to be 60% reliable.	5.1 - 11.3 Cents/kW-h	Hydro is currently the only source of renewable energy making substantive contributions to global energy demand. Hydro plants, however, can (obviously) only be built in a limited number of places, and can significantly damage aquatic ecosystems.
Solar Currently supplies approximately 0.8% of the global electricity demand.	10 - 30 Cents/kWh	Solar power has been expensive, but soon is expected to drop to as low as 3.5 cents/kW-h.

An evaluation of the potential contribution of renewable energies concludes that, given adequate support, renewable energy technologies could meet much of the growing demand at prices lower than those usually forecast for conventional energy. As presented in figure 1.9 and figure 1.10, in a renewables-intensive

global energy scenario, renewable energy could account by the middle of the twenty-first century for three-fifths of the world's electricity market and two-fifths of the market for fuels used directly [9].

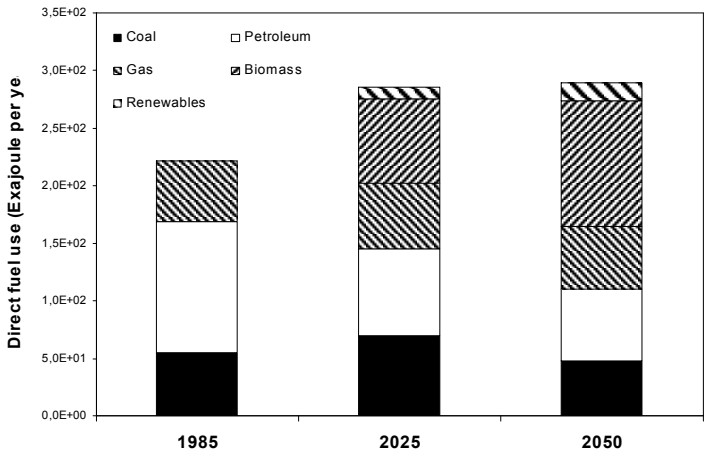

Figure 1.9 The renewables-intensive global energy scenario, 1985-2050: electricity generation. [9]

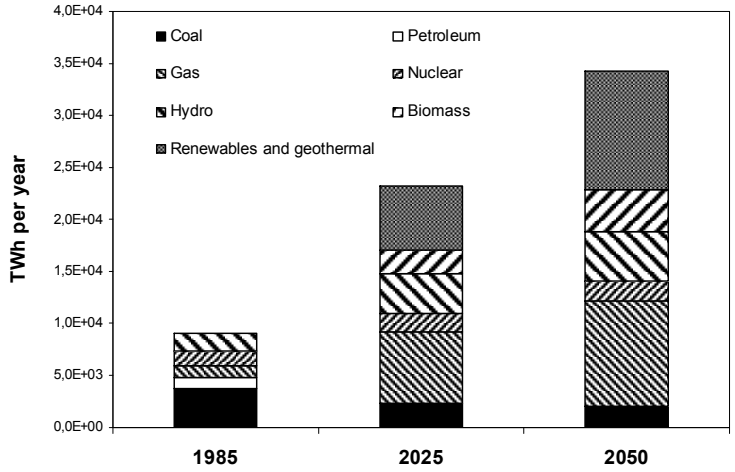

Figure 1.10 The renewables-intensive global energy scenario, 1985-2050: direct fuel use. [9]

Moreover, a transition to a renewables-intensive energy economy would provide environmental and other benefits not measured in standard economic accounts: because renewable energy is expected to be competitive with conventional energy, such benefits could be achieved at no additional cost. These benefits are tabulated below.

Table 1.3 - The benefits of renewable energy not captured in standard economic accounts

Social and economic development	Production of renewable energy, can provide economic development and employment opportunities especially in areas that otherwise have limited opportunities for economic growth. Renewable energy can thus help reduce poverty in rural areas and reduce pressures for urban migration.
Reduced air pollution	Renewable-energy technologies produce virtually no emissions associated with urban air pollution and acid deposition.
Abatement of global warming	Renewable energy use does not produce carbon dioxide and other greenhouse emissions that contribute to global warming. Even the use of biomass fuels will not con tribute to global warming: the carbon dioxide released when biomass is burned equals the amount absorbed from the atmosphere by plants as they arc grown for biomass fuel.
Reducing the risks of nuclear weapons proliferation	Competitive renewable resources could reduce incentives to build a large world infrastructure in support of nuclear energy, thus avoiding major increases in the production, transportation, and storage of plutonium and other nuclear materials that could be diverted to nuclear weapons production.

Renewable energy sources are perpetual and guarantee a secure supply, minimizing dependency on outside energy suppliers. At the same time, the use of renewable energy cuts emissions of carbon dioxide, addressing environmental concerns. In this context, photovoltaic technology offers a key solution for energy issue due to its unique features: it is safe, clean, robust and proven to be efficient and highly scalable. Photovoltaic is easy to introduce and implement (in “stand-alone” or “grid connected” systems) all over the world, in both developed and developing countries.

1.4 - PHOTOVOLTAIC ENERGY

The majority of renewable energy technologies are powered by the sun. Solar energy (radiant light and heat from the sun) has more distribution across the Earth than other forms of renewables such as wind or hydro that are available only in select places: solar energy is spread out across the entire Earth surface.

The available solar energy resources are 3.8YJ/yr (120,000TW). Less than 0.02% of available resources are sufficient to entirely replace fossil fuels and nuclear power as energy source [2].
Photovoltaics (or "PV") is the field of technology and research related to the devices which directly convert sunlight into electricity. The elementary building block of the photovoltaic technology is the solar cell which works generating direct current electrical power (measured in Watts) from semiconductors when it is illuminated. The direct conversion of sunlight into electricity is a very elegant process to generate environmentally friendly, renewable energy. This technology presents several advantages compared to conventional fossil fuel energy production: source is vast and essentially infinite, there are no emissions, combustion or radioactive fuel for disposal (does not contribute perceptibly to global climate change or pollution). Photovoltaic systems operate at ambient temperature (no safety issues) and have a very low operating cost because there is no need of any fuel. Moreover PV modules can be installed quickly at nearly any point-of-use, integrated into new or existing building structures and have high reliability (>20 years).
On the other hand, photovoltaics presents some issues and drawbacks: energy source is diffuse (sunlight is a relatively low-density energy), installation costs are very high, and there is a poor reliability of auxiliary (Balance of System) elements. To be noted that several of these disadvantages are non-technical but related to economics and infrastructure (lack of widespread commercially available system integration and installation so far and lack of economical efficient energy storage).

1.4.1 - History of photovoltaics

Although discovered in 1839, the process of producing electric current in a solid material with the support of sunlight was not really understood for more than a hundred years. Only during the second half of the 20th century, the science has been refined and the process has been more fully explained.
The photovoltaic effect was first recognised in 1839 by French physicist Alexandre-Edmond Becquerel. At only 19, Becquerel found that certain materials would produce small amounts of electric current when exposed to light. But this effect remained a curiosity of science for the next three quarters of a century.
It was first studied in solids, such as selenium, by Heinrich Hertz in the 1870s. As a result, Selenium was quickly adopted in the emerging field of photography for use in light-measuring devices. However, it was not until 1883 that the first solar cell was built by Charles Fritts, who coated the semiconductor Selenium with an extremely thin layer of Gold to form the junctions. The device was only about 1% efficient. Major steps toward commercializing PV were taken in the 1940s and early 1950s, when the Czochralski process was developed for producing highly pure crystalline silicon. Russell Ohl patented the modern solar cell in 1946 [10]. Sven Ason Berglund had a prior patent concerning methods of

increasing the capacity of photosensitive cells. The modern age of solar power technology arrived in 1954 when Bell Laboratories, experimenting with semiconductors, accidentally found that silicon doped with certain impurities was very sensitive to light. In 1954, in fact, scientists at Bell Laboratories developed the first crystalline silicon PV cell, having an efficiency of 4%. Table 1.4 reports the early steps of the PV development [11].

Table 1.4 - Early PV development

Year	Development
1839	Antoine-César Becquerel discovered the photovoltaic effect. In his experiments he found that voltage was produced when a solid electrode in an electrolyte solution was exposed to light.
1877	W.G. Adams and R.E. Day observed the photovoltaic effect in solid selenium. They built the first selenium cell and published "The action of light on selenium," in *Proceedings of the Royal Society*.
1883	Charles Fritz built what many consider to be the first true photovoltaic cell. He coated the semiconductor selenium with an extremely thin layer of gold. His photovoltaic cell had an efficiency of less than 1%.
1904	Albert Einstein published a paper on the photoelectric effect.
1927	A new type of photovoltaic cell was developed using copper and the semiconductor copper oxide. This device also had an efficiency of less than 1%. Both the selenium and copper oxide devices were used in applications such as light meters for Photography.
1941	Russell Ohl developed the silicon photovoltaic cell. Further refinement of the silicon photovoltaic cell enabled researchers to obtain 6% efficiency in direct sunlight in 1954.
1954	Bell Laboratories obtained 4% efficiency in a silicon photovoltaic cell. They soon achieved 6% and then 11%.
1958	PV cells were first used in space on board the NASA Vanguard satellite.

During PV technology development, various materials have been investigated in order to obtain high-quality photovoltaic cells, evaluated by two fundamental criteria: efficiency (ratio of the electric power output to the light power input) and production cost. According to this criteria, cells have been developed following three main ways, called 'generations' in the industry, defined by the types of semi-conductors and manufacturing techniques used.

First generation refers to single junction, high quality and low defect single crystal photovoltaic devices. These cells have high efficiencies and are approaching to the efficiency limit for single band gap devices. As shown in figure 1.11, such devices are not expected to get lower than 1$/W [12].

Second generation technology involves low cost and low energy intensity growth techniques such as vapour deposition and electroplating. Such processes can bring costs down to a little under 0.50$/W but because of the defects

inherent in the lower quality processing methods, second generation cells have much reduced efficiencies compared to first generation.
Third generation derives from the progression of photovoltaic know-how and it is somewhat ambiguous in the technologies that it includes. Third generation PV cells are potentially able to overcome the efficiency limit of 31-41% for single band-gap PV cells.
Presently, there is concurrent research into all three generations but first generation devices (single junction, wafer-based cells) still represent the majority of available photovoltaic equipment on the market and crystalline silicon is the most common material used to produce PV cells.

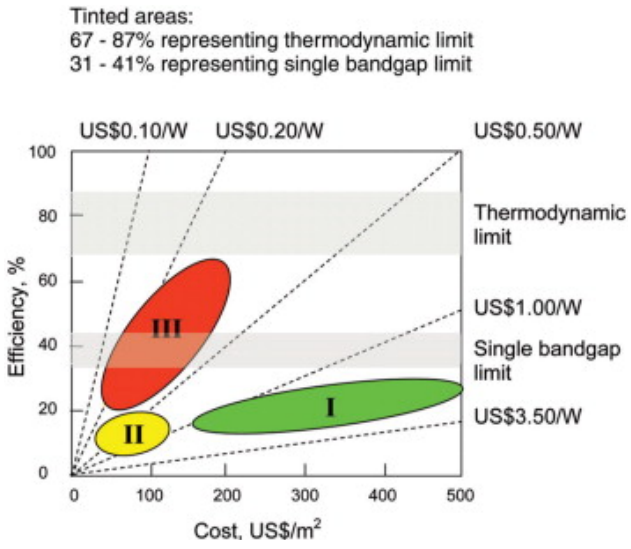

Figure 1.11 Efficiency and cost projections for the three generations of photovoltaic technology. [12]

1.4.2 - PV technology generations

The first photovoltaic generation consists of a large-area, single layer *n-p* junction diode, which is capable of generating usable electrical energy from light sources with the wavelengths of sunlight. Self supporting semiconductor wafers (polycrystalline or mono-crystalline) of ~300µm thick are fabricated and then soldered together to form a module.
These cells are typically made using a silicon wafer: silicon wafer-based technology was first developed more than 50 years ago at Bell Laboratories in New Jersey. Mono-crystalline silicon wafers are normally made using the Czochralski process and most commercial mono-crystalline cells have efficiencies on the order of 16%.
Single crystal cells tend to be expensive, and because they are cut from cylindrical ingots, they cannot completely cover a module without a substantial waste of refined silicon. Poly or multi crystalline are made from cast large

blocks of molten silicon carefully cooled and solidified. These cells are cheaper than single crystal cells, but also rather less efficient. However, they can easily be formed into square shapes that cover a greater fraction of a panel than mono-crystalline cells, and this compensates their lower efficiencies.
The first generation technology is technically proven and reliable and represents the dominant technology in the commercial production of photovoltaic cells, accounting for more than 86% of the solar cell market.
Nevertheless, there are several inherent limitations and drawbacks to this generation. Silicon wafers are fragile, making processing difficult and limiting potential applications. The process is very laborious and energy intensive and manufacturing plant capital costs are high. Finally, because materials represent more than 60% of manufacturing costs and silicon supply is finite, the long term potential for cost reduction is insufficient to deliver broadly affordable energy.
Figure 1.12 shows breakdown of costs in the fabrication of silicon wafer-based PV modules [13].

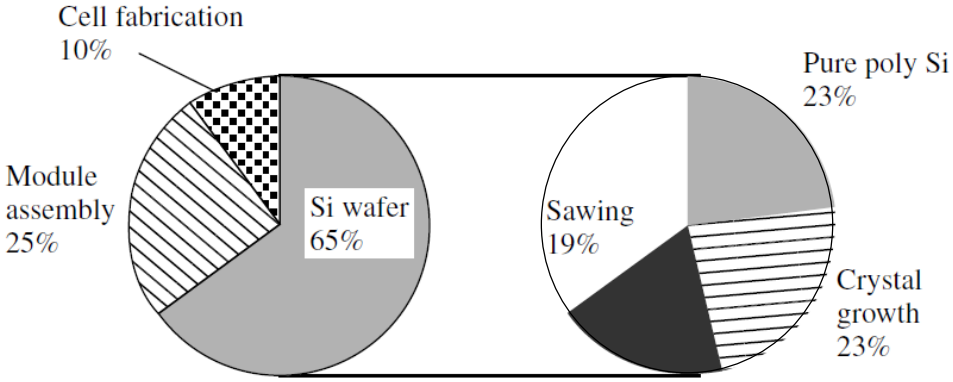

Figure 1.12 Breakdown of costs in the fabrication of a Si-wafer-based PV module. The right side presents the wafer costs. Materials represent more than 60% of manufacturing costs. [13]

The second generation of photovoltaic cells is based on the use of semiconductors thin-film deposits produced generally using chemical vapour deposition techniques, typically plasma enhanced (PE-CVD). These devices were initially designed to be high-efficiency, as multiple junction photovoltaic cells. Later, the main advantage of using a thin-film of semiconductor was noticed to be the reduction of the mass of the material required and, consequently, the reduction of manufacturing cost. Currently there are different technologies and materials under investigation such as amorphous silicon, poly-crystalline silicon, micro-crystalline silicon, cadmium telluride, copper indium selenide/sulfide (CIS). Amorphous silicon and CIS are the two most important thin-film approaches at present in production, with efficiencies around 8% and 11% respectively.

Typically, the efficiencies of thin-film solar cells are lower compared with silicon (wafer-based) solar cells, but manufacturing costs are also lower, so that a lower price in terms of $/Watt of electrical output can be achieved. The semiconductor mass reduction allows also to fit panels on light materials or flexible materials but the loss of efficiency causes the necessity to enlarge the module area to obtain a suitable output current.
Third generation contains a series of new devices based on innovative technologies. These new devices include quantum dot cells, tandem/multi-junction cells, intermediate band solar cells, hot-carrier cells and non-semiconductor cells (polymer solar cells, dye-sensitized titania solar cells, organic photovoltaics). It has been estimated that third generation PV technologies will achieve higher efficiencies and lower costs than first or second generation.
Figure 1.13 illustrates the various commercial large-area module energy conversion efficiencies and the best laboratory efficiencies obtained for various materials and technologies [14] [15].

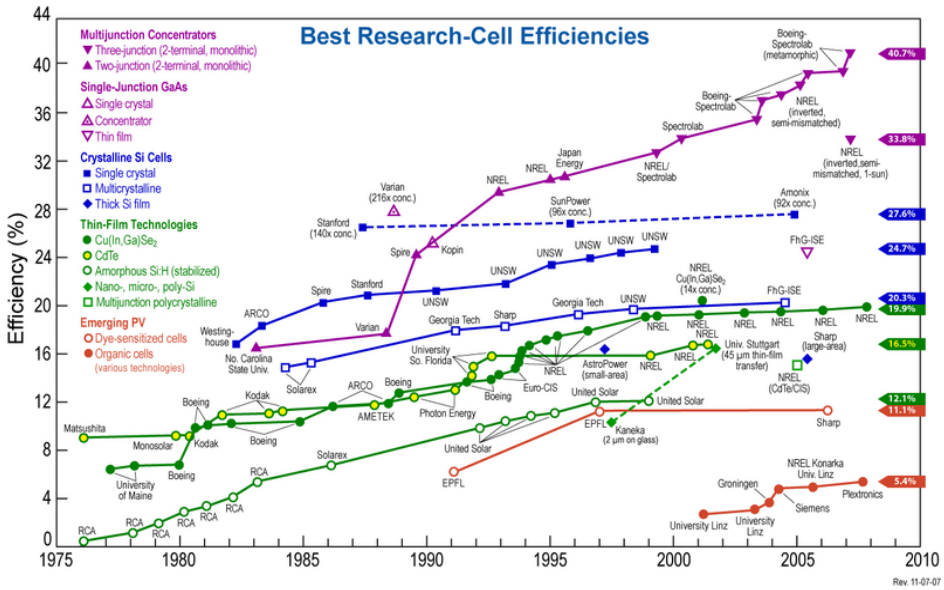

Figure 1.13 Best-research-cell efficiency. The most efficient solar cells devices developed to date are the one based on multijunctions. [15]

The most efficient solar cells devices developed to date are the one based on multijunctions. As organic cells technology (built from thin films of organic semiconductors such as polymers and small-molecule compounds) is quite new, it is difficult to predict their development.
Despite the numerous attempts to produce better solar cells by using new materials and technologies, today the photovoltaics market is still dominated by

silicon wafer-based solar cells (first-generation solar cells). Consequently, a large field of research is currently committed to create silicon wafer-based solar cells that can achieve higher conversion efficiency without an excessive increase in production cost. The aim of the research is to achieve the lowest $/Watt solar cell design that is suitable for commercial production.
The propose of today's PV research and manufacturing is to produce a low cost PV system, that mean not only low-cost-efficient solar cells, but also low cost efficient system including mounting hardware, power conditioning electronics, storage, tracking, and so on (Table 1.5).

Table 1.5 - Goals of current solar cell research and manufacturing

• Use less semiconductor material by making thinner cells.
• Use less expensive semiconductor materials.
• Improve solar cell performance with less expensive, less perfect semiconductors.
• Even with this poorer material keep a high production yield, that is, reduce the number of cells or modules rejected by the quality control.
• Increase material utilization by reducing waste in semiconductor and cell fabrication.
• Increase solar cell flux on the solar cells by using concentrators without increasing cost or optical losses too much. In this way, less semiconductor material is used.
• Increase solar radiation utilization by absorbing more of the spectrum efficiently.
• Increase speed and throughput of manufacturing processes.
• Simplify processing steps (this reduces fabrication costs and increases the yield) and reduce equipment costs.
• Reduce costs and improve reliability of BOS (auxiliary elements).

1.4.3 - PV market: status and forecast

Solar power is one of the worldwide fastest-growing sources of renewable energy. Many nations, concerned about the environmental impacts of electricity generation from fossil fuels, nuclear plant or hydroelectric plants, have been turning to solar power as an environmentally alternative. The potential for large-scale applications of solar power has improved considerably in recent years.
At present, the cost of electricity produced from photovolatics generally is too high to compete with extensive electricity. On the basis of installed price per megawatt, photovoltaic installations are relatively costly, because the panel components are expensive and the conversion of solar energy to electricity in the cells still is inefficient. From conversion efficiencies of 4% to 6% for the first solar cells built in the 1950s, there has been an improvement to efficiencies of about 16% for modern commercial wafer-silicon cells. This efficiency gain, coupled with other technological progresses, has reduced the cost of photovoltaic capacity from approximately 300$ per Watt in 1956 to less than 5$ per Watt in 2009. EIA's Annual Energy Outlook 2009 projects that, by 2030, capacity costs for new generating plants using solar photovoltaics will be 37% lower than the 2009 costs. In addition, the efficiency of solar PV applications is expected to improve as the technology continues to be developed.

Nevertheless, prices for electricity from photovoltaics may not become widely competitive with prices for electricity from conventional generating technologies within the next 25 years. They may be competitive with high retail electricity prices just in sunny regions where the cost can be as low as 0.23$/KWh and may compete with the delivered price of electricity to retail customers in areas where electricity prices are high, as they are in California, Southern Spain, and Italy [2] [16] [17].
However, the current levels of dependence on fossil fuels, the need of reducing the Carbon dioxide emissions associated with energy production and the prospects of developing a new and extremely innovative technology sector, make photovoltaics increasingly attractive. As shown in figure 1.14, in the last years the photovoltaic market expanded extensively. The annual world growth in sales of photovoltaics was over 33% per year from 1995 to 2000. In 2007 grid-connected photovoltaic electricity was the fastest growing energy source, with installations of all photovoltaics increasing by 83% in 2009 to bring the total installed capacity to 15 GW. Assuming that our rate of usage in 2005 remains constant, we could run out of conventional oil in 40 years (2045), coal in 154 years (2159) [17].

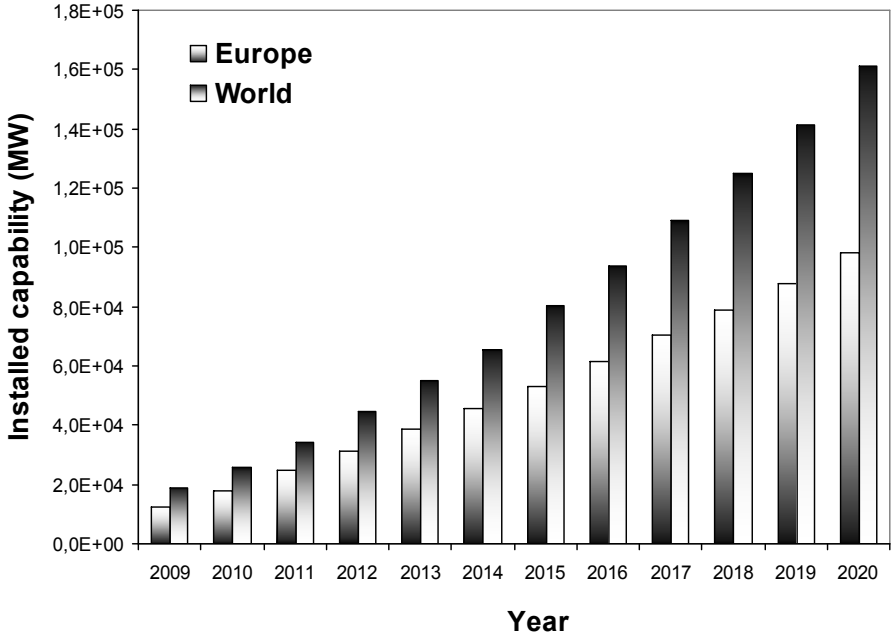

Figure 1.14 Evolution and forecast of World and European PV market. The annual world growth in sales of photovoltaics was over 33% per year from 1995 to 2000. In 2007 grid-connected photovoltaic electricity was the fastest growing energy source, with installations of all photovoltaics increasing by 83% in 2009 to bring the total installed capacity to 15 GW. [17]

The growth trend of the principal solar PV countries guides the investors to their investment decisions. Photovoltaic technology is gaining market share in countries where diminishing prices and government-backed financial incentives have led to increase usage. Solar technologies have benefited from much research and development over the past two decades, bringing down the delivered price of solar electricity.

Photovoltaic systems today are more than 60% cheaper than they were in the 1990. The focus lies now on cost reduction in order to reach competitiveness with all sources of electricity in the medium term. In the 1997 White Paper, the European Commission set a target of 3GW of photovoltaic capacity to be installed in Europe by 2010. The White Paper target, already exceeded in 2006, has been more than tripled in 2008, with a total cumulative capacity of more than 9.5GW achieved. This illustrates an increase of 200% compared to 2006. In 2010 the total cumulative capacity installed in the European Union could be as much as 16GW.

The European photovoltaic industry currently has an important role in photovoltaic technology development, capturing about 30% of the world market of photovoltaic modules. More than 56% of the EU photovoltaic installations are located in Germany that is the leader in photovoltaic installation: after the renewable energy law came into effect in 2004 with a feed-in tariff of 27cents per KWh, profits from photovoltaics have risen more than 10 times since 2003. The market stagnated somewhat in 2006 with installed capacity of 830 MW compared with 866 MW in 2005. There are more than 80 companies involved in production of thin-layer technology in Germany [18].

In order to increase the adoption of photovoltaics and its competitiveness in all EU Member States, it is necessary to create an attractive financial support that could encourage the growth of the PV industry. The possibilities are wide, ranging from investment support (capital grants, tax exemptions or reductions on the purchase of goods) to operating support (price subsidies, green certificates, tender schemes and tax exemptions or reduction on the production of electricity). Another crucial aspect is the reduction of administrative difficulties and grid barriers.

In summary, it is very probable that photovoltaics will become in the next half century one of the most important source of world electricity. Public support and global environmental concerns will keep photovoltaics viable, visible, and vigorous both in new technical developments and user applications. Nations which encourage photovoltaics will be leaders in this shining new technology, leading the way to a cleaner, more equitable twenty-first century, while those that ignore or suppress photovoltaics will be left behind in the green, economic energy revolution. The technical potential of PV electricity is high enough to contribute considerably to the abatement of the human-made global CO_2 problem. With the help of medium-term financial supports and long-term energy taxes (motivated by external costs), the technical potential may be exploited economically. Under grid-coupled operation, photovoltaics will most probably

become cost-effective for distributed peak power production and for applications in the building sector (as cladding element). Solar electricity generation has to grow by three orders of magnitude before it encounters a (extrapolated) 10% level of the global electricity demand. Assuming ambitious growth rates, this process of transformation will take some decades.

References

[1] Benka S., *Phys. Today* (2002).

[2] U.S. EIA – U.S. Energy Information Administration, *International Energy Outlook 2009*.

[3] BP, *Statistical Review of World Energy 2009*.

[4] Tozzi M., *L'Italia a secco* (2006).

[5] The Uranium Institute - Twenty Fourth Annual International Symposiums - *Supply of Fuel for Nuclear Power, Present Situation and Perspectives* (1999).

[6] Fourth Assessment Report of the Intergovernmental Panel on Climate Change (IPCC) (2007).

[7] IAEA - International Atomic Energy Agency (2010).

[8] U.S. Department of Energy (DOE) - Carbon Dioxide Information Analysis Center (CDIAC).

[9] Johansson, T. B., H. Kelly, A. K. N. Reddy, and R. H. Williams (eds.). 1993. *Renewable Energy: Sources for Fuels and Electricity*. Washington, D.C.: Island Press.

[10] "Light sensitive device" U.S. Patent 2,402,662.

[11] D. M. Chapin, C. S. Fuller, and G. L. Pearson; J. Appl. Phys. 25, 676 (1954).

[12] M.A. Green, Third Generation Photovoltaics: *Ultra-High Efficiency at Low Cost*, Springer-Verlag, Berlin (2003).

[13] Luque A., Hegedus S., *Handbook of photovoltaic science and engineering*, John Wiley & Sons, New York, NY (2003).

[14] M. A. Green, *Third Generation Photovoltaics: Advanced Solar Energy Conversion* (2003).

[15] Lawrence Kazmerski, NREL - National Renewable Energy Laboratory (2010).

[16] John G., *Global Solar Photovoltaic Market Analysis and Forecasts to 2020* (2009).

[17] EER – Emerging Energy Research, Global Renewable Power Generation Forecasts: 2010-2025 (2010).

[18] JRC – Joint Research Centre, *PV Status Report 2009*.

2. The Photovoltaic Cell: Fundamentals, Working Principles and Electrical Characteristic

2.1 – INTRODUCTION

Basically, semiconductor photovoltaic cells are very simple devices. Semiconductors have the capacity to absorb light and to utilize a portion of the energy absorbed from incident photons to generate charge carriers (electron-hole pairs); a semiconductor diode separates and collects the photo-generated carriers and conducts the electrical current preferentially in a specific direction.
Thus, a solar cell is simply a semiconductor diode designed and constructed to efficiently absorb and convert light energy from the sun into electrical energy.
Inside this chapter the fundamental notions indispensable to understand the working of a PV cell (theoretical model, equivalent circuit, electrical characteristic) are explained. Finally, a brief description of the silicon wafer-based PV cell manufacturing process flow is given.

2.2 – SOLAR IRRADIATION

Development, optimization and characterization of photovoltaic cells involve a certain knowledge of the used energy source: the sun.
Sun surface behaves like a black body at about 5800K with an emission peak situated on a wavelength of 500nm and a power of about 60MW/m^2. Just above Earth's atmosphere the radiation intensity is about 1.35kW/m^2; on Earth surface, instead, this irradiance is weighted over different factors: absorption by molecules composing atmosphere, climatic conditions, season and latitude of observation site [1]. Gas like Ozone (for wavelength lower than 0.3μm) carbon dioxide and water vapour (for infrared below 2μm) absorb energies close their bonding energy causing "holes" inside visible solar spectrum on soil. Moreover, dust and aerosol induce an absorption distributed almost on entire spectral range, leading a global reduction of incident power.
To compare and unify performances of photovoltaic cells it has been instituted the notion of Air Mass. The Air Mass is a measure of how absorption in the atmosphere affects spectral content and intensity of the solar radiation reaching Earth's surface. The Air Mass number is given by

$$AM = \frac{1}{\cos\theta} \tag{2.1}$$

where θ is the angle of incidence (θ=0° when the sun is directly overhead). As defined, the Air Mass number is always greater than or equal to one at Earth's surface. A widely used standard for comparing PV cell performance is the AM1.5 spectrum normalized to a total power density of 1kW/m^2.
The spectral content of sunlight at the Earth's surface has also a diffuse, indirect component (due to scattering and reflection in the atmosphere and surrounding landscape) which can account up to 20% of the light incident on a PV cell. The Air Mass number is consequently further defined in accordance with the measured spectrum, if it includes or not the diffuse component. An AM1.5g (global) spectrum includes the diffuse component, while an AM1.5d (direct) does not.
Black body (T = 5762 K), AM0, and AM1.5g radiations spectra are shown in figure 2.1 [1] [2].

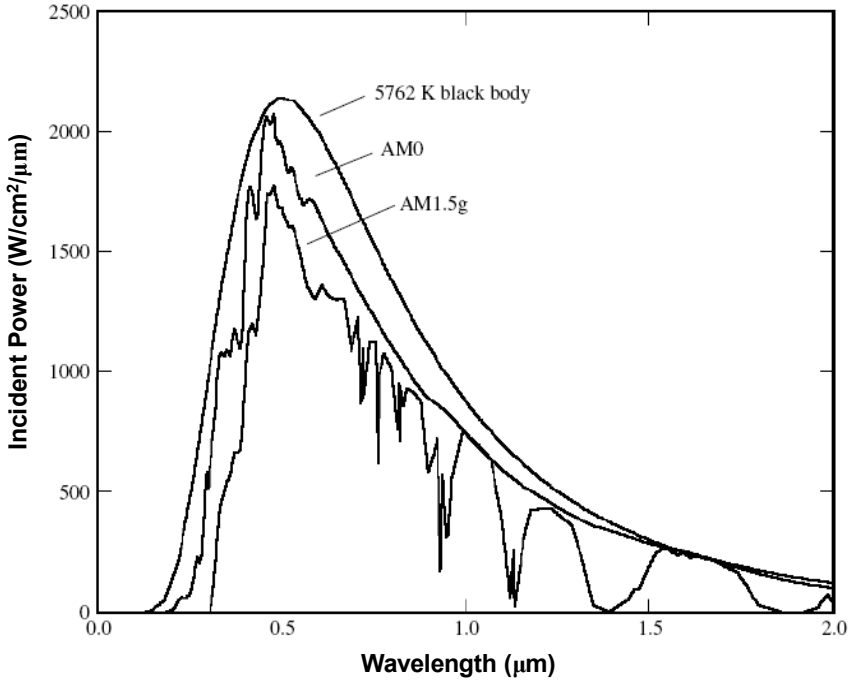

Figure 2.1 The radiation spectrum of a black body at 5762K compared with solar AM0 and AM1.5 global spectra. [2]

2.3 – WORKING PRINCIPLES OF A SILICON PV CELL

The generation of electric current in a solid material with the aid of sunlight is made by devices using photon/semiconductor interaction. The photovoltaic effect is the physical process through which a solar cell converts sunlight into electricity.

2.3.1 – Photon/Semiconductor interaction

The presence of a gap in the energy band structure is the fundamental characteristic of semiconductors material that allows making use of photovoltaic effect. Figure 2.2 shows the different possible transitions according to gap nature. When the minimum of the conduction band (BC) and the maximum of the valence band (BV) have the same crystal momentum value, the gap is called direct. When they do not align, the gap is said to be indirect. Transitions inter bands in the case of direct band-gap occur "vertically" and are radiative: this kind of transition is illustrated in figure 2.2a.

This process is impossible in an indirect band gap, because conservation of crystal momentum would be violated. Consequntely radiative transition process in an indirect band gap material must also involve absorption or emission of a phonon (figure 2.2b). In the case of indirect band-gap (as in silicon) electronics transitions between bands limits are "oblique" and involve a change of electron *k*-vectors.

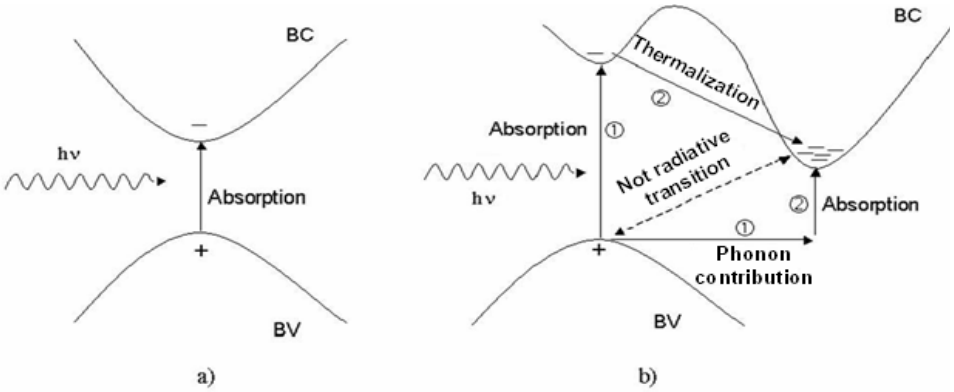

Figure 2.2 Inter bands electronics transitions inside a semiconductor. a) Direct band gap semiconductor. b) Indirect band gap semiconductor. Transitions inter bands in the case of direct band-gap occur "vertically" and are radiative. Transition process in an indirect band gap material must involve the absorption or emission of a phonon to guarantee the conservation of the crystal momentum

The interaction between photons and semiconductor is explained by an essential characteristic of the material: the absorption coefficient. It indicates the number of photons absorbed per unit of thickness as a function of incident wavelength (or energy). Figure 2.3 shows the silicon absorption coefficient and photons penetration depth inside silicon versus incident wavelength [3].

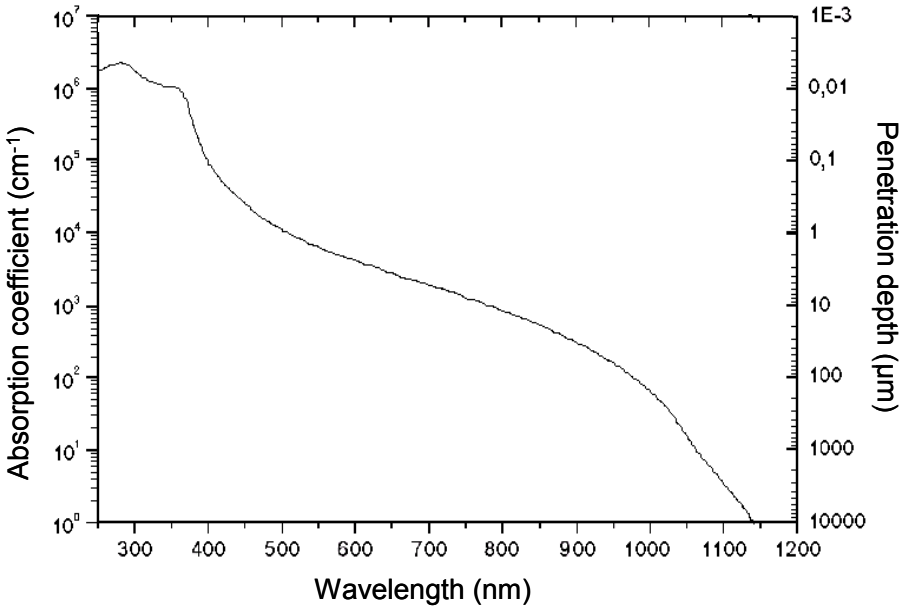

Figure 2.3 Silicon absorption coefficient and photons penetration depth. For wavelength lower than 365nm, majority of incident photons is absorbed inside first 100Å of material. [3]

For wavelength lower than 365nm, majority of incident photons is absorbed inside first 100Å of material. For longer wavelength direct transitions are no more possible: it's necessary that at least a phonon would be emitted or absorbed so that electron could drop to conduction band. This process reduces transition probability so the silicon absorption coefficient decreases on increasing of wavelength. When photons energy becomes smaller than band gap energy, transition can not occur and photons are not absorbed.

2.3.2 – Photovoltaic cell fundamentals

The absorption mechanism at the origin of the photovoltaic cell working is the creation of electron-hole pairs by means of incident photons energy transfer to semiconductor crystal lattice. Solar energy conversion in electric energy via photovoltaic cell is based on to two steps:

- photons (with energy higher than band-gap energy E_{gap}) absorption inside semiconductor by creation of electrons-holes pairs
- collection of photogenerated charges.

The most common PV cell is configured as a silicon *n-p* junction that, for simplicity, could be imagined as constituted by the direct contact between a layer of *n*-type silicon with a layer of *p*-type silicon. When an *n-p* junction is formed, since there is a concentration difference of holes and electrons between the two types of semiconductors, holes diffuse from the *p*-type region into the *n*-

type and, similarly, electrons from the *n*-type material diffuse into the *p*-type. As the carriers diffuse, the charged impurities (ionized acceptors in the *p*-type material and ionized donors in the *n*-type material) remain uncovered because no longer screened by the majority carriers. These uncovered impurity charges produce an electric field which limits the diffusion of the holes and electrons. In thermal equilibrium, the diffusion current for each carrier type exactly balance the drift current, so there is no net current flow. The transition region between the *n*-type and the *p*-type semiconductors is called the "space-charge region"or "depletion region", since it is depleted of both holes and electrons.
According to this configuration, when photons from light of an appropriate wavelength ($hc/\lambda > E_{gap}$) hits the silicon cell they can transfer their energy to generate electron-hole pairs. As photogenerated charges are free to move independently within the silicon lattice, electric field in the junction drives electrons in the *n*-side and the holes in the *p*-side. Entire process is described in figure 2.4 where the functioning of a n^+-*p* PV cell is reported. The n^+-type layer is the light exposed side (emitter); the *p*-type layer is the bulk (base) of the cell [4].

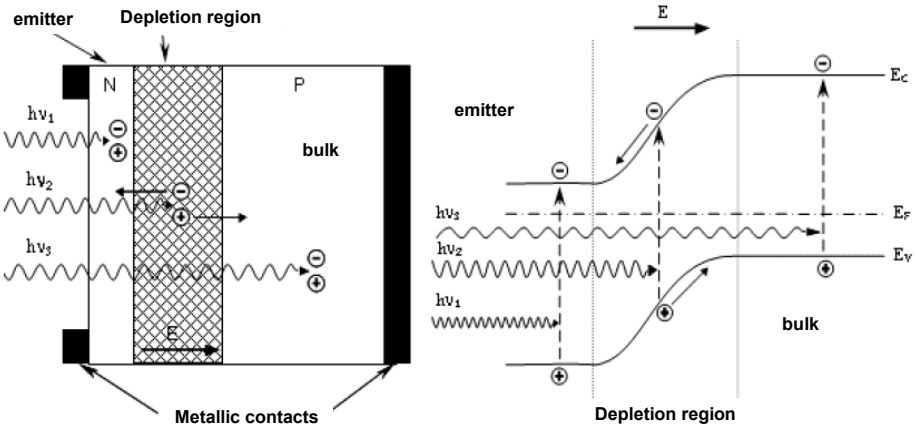

Figure 2.4 Structure and band diagram of a Silicon PV cell n^+-*p*. [4]

Ohmic contacts are applied to both *n* and *p* sides of the cell and connected to a load: the electrons created in the *n*-type or collected by the junction and pushed in the *n*-type, can thus reach the load and feed it, then continue until getting the contact to the *p*-side cell.

2.4 – PV CELL EQUIVALENT CIRCUIT AND I-V CHARACTERISTIC

The simplified equivalent circuit of an ideal solar cell consists of a photocurrent source in parallel with a diode, as shown in figure 2.5.

In dark condition, when there is no light to generate any current, the device behaves like a diode; as the intensity of incident light increases, current is produced by the PV cell.

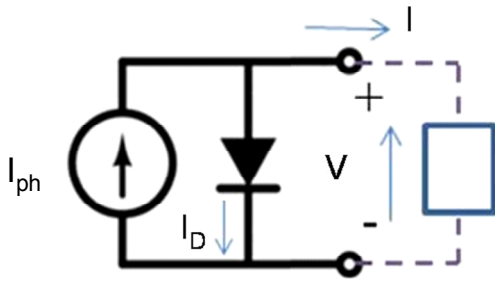

Figure 2.5 Equivalent circuit of an ideal PV cell. Parasitic resistances are neglected.

The current–voltage equation of the simplified equivalent circuit could be derived from Kirchhoff's law. In an ideal cell, the total current output I is equal to the difference between current I_{ph} generated by the photoelectric effect and the diode current I_D, according to the equation:

$$I(V) = I_{ph} - I_D(V) = I_{ph} - I_0\left(e^{\frac{qV}{nKT}} - 1\right) \tag{2.2}$$

with I_0 diode reverse saturation current, q elementary charge, K constant of Boltzmann , T absolute temperature and n ideality factor. The ideality factor n varies from 1 to 2 depending on the fabrication process and semiconductor material [3].
Nevertheless, the simplified circuit model shown above doesn't give an optimal representation of a real PV cell electrical behaviour because neglects the contribution of parasitic resistances. These resistances can be represented as a parallel shunt resistance (R_{sh}) and a series resistance (R_s), as illustrated in figure.2.6.

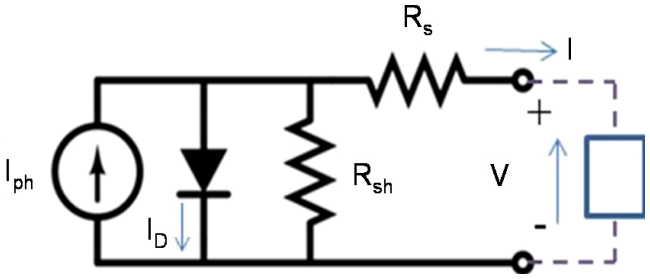

Figure 2.6 Equivalent circuit of a real PV cell.

R_s is the resistance between the different layers of the cell: emitter, bulk and metallic contacts (in particular their interface with semiconductor). R_{sh}

represents instead the power dissipation caused by leakage currents due to alternative paths of the current flow (i.e. edge short circuit). Thus, for a real solar cell, equation 2.2 must be expanded adding R_s and R_{sh} contribution.

$$I(V) = I_{ph} - I_0\left(e^{\frac{q(V+IR_s)}{nKT}} - 1\right) - \frac{V+IR_s}{R_{sh}} \tag{2.3}$$

The *I-V* characteristic of a typical silicon solar cell is plotted in figure 2.7.

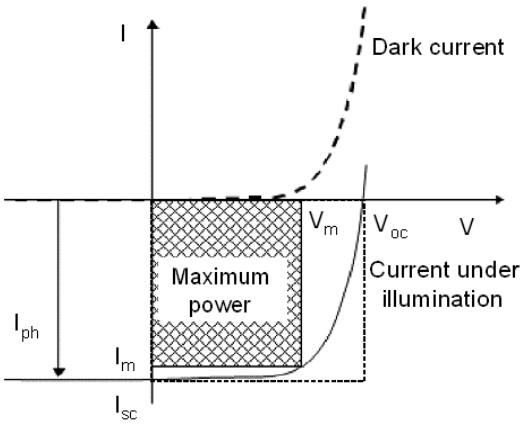

Figure 2.7 Typical *I-V* characteristic of a PV cell under illumination and in dark condition. [4]

I_{sc} is the short circuit current, corresponding to the short circuit condition when the voltage is null.

$$I_{sc} = I(V=0) \tag{2.4}$$

For an ideal cell ($R_s=0$, $R_{sh}\rightarrow\infty$), this maximum current value is equal to the total current produced by photon excitation ($I_{sc}=I_{ph}$).
V_{oc} is the open circuit voltage and occurs when no current pass through the cell.

$$V_{oc} = V(I=0) = \frac{nKT}{q} ln\left(\frac{I_{ph}}{I_0} + 1\right) \tag{2.5}$$

It is the maximum voltage difference across the cell.
V_m and I_m are the voltage and the current referred to the point of the characteristic where the power output is maximum. The power produced by the cell can be calculated along the *I-V* curve by the equation $P=VI$: the point (V_m,I_m) defines a rectangle whose area $P_m= V_mI_m$ is the largest than for any point on the *I-V* curve.

A parameter utilized to characterize the maximum power point is the fill factor, *FF*. It is defined as the ratio of the areas of the two rectangles shown in figure 2.7 and it is a measure of the squareness of the *I-V* characteristic:

$$FF = \frac{P_m}{V_{oc} I_{sc}} = \frac{V_m I_m}{V_{oc} I_{sc}} \tag{2.6}$$

Fill factor is obviously always less than one.
The most important parameter to evaluate the electric performance of a solar cell is the power conversion efficiency, η, which is defined as the ratio of the maximum electrical power output, P_m, to the solar power input, P_{in}:

$$\eta = \frac{P_m}{P_{in}} = \frac{FF V_{oc} I_{sc}}{P_{in}} \tag{2.7}$$

P_{in} is the product of the irradiance of the incident light, measured in W/m^2, with the surface area of the solar cell [3] [4] [5] [6].
Since efficiency measurement can be affected also by ambient conditions, PV electric tests must be done under standard conditions (STC) that specifies a temperature of 25 °C and an irradiance of 1000W/m^2 with an air mass 1.5 global spectrum (AM1.5g).
Efficiency is the key feature in the photovoltaic conversion of solar energy because it gives some expectations on the possibility of its generalised cost-effective use in electric power production.

2.5 – THEORETICAL EFFICIENCY

The two key factors determining solar cell theoretical efficiency are electron–hole pair generation and their recombination before being delivered to the external circuit. Therefore, photovoltaic cell theoretical efficiency depends on the physical characteristics of semiconductor material used to obtain light conversion into electricity. These characteristics include the ability of semiconductor to absorb photons by conferring energy to charge carriers and the ability of semiconductor material to conduct electricity.
In order to calculate PV cell theoretical efficiency, all generation mechanisms and recombination sources must be considered and the matching of PV cell material band gap to the solar spectrum must be evaluated.

2.5.1 – Efficiency and band gap

Since only photons with energy $hv > E_{gap}$ can create electron–hole pairs and contribute to the PV cell output, the band gap determines how well the solar cell is coupled to the solar spectrum. If incident spectrum is fixed, then η depends

only on band-gap energy. Intuitively, very small and very large band gaps lead to poor photo-conversion: in the first case, the working voltage value is too small (qV_m, like qV_{oc} always less than E_{gap}) and in the second case, the photocurrent value is too small.
A simple prediction of maximum solar cell efficiency can be performed assuming E_{gap} as the maximum energy that can be extracted from an absorbed photon:

$$\eta_{max}(E_{gap}) = \frac{E_{gap} I_{inc}}{qP_{in}} = \frac{E_{gap}}{P_{in}/A} \int_{\lambda<\lambda_{gap}} f(\lambda)d\lambda \tag{2.8}$$

where I_{inc} is the incident intensity and $f(\lambda)$ is the incident photon flux (number of photons incident per unit area per second per wavelength).
Figure 2.8 illustrates the η_{max} plot (calculated for an AM1.5g spectrum) as a function of material energy gap. Plot shows a maximum efficiency of 48% at about E_{gap}=1.1eV, close to the silicon band gap [5] [6].

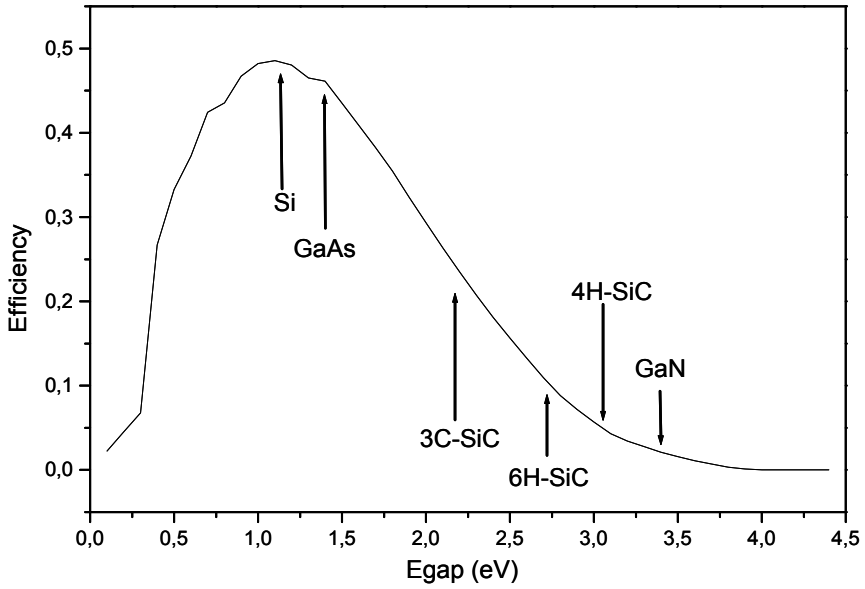

Figure 2.8 Calculated theoretical efficiency versus semiconductor E_{gap} (AM1.5g spectrum). Semiconductors with band gaps between 0.7 and 1.6eV have efficiencies in close proximity to the theoretical maximum.

This rough approximation, obtained neglecting any recombination effect, demonstrates the important role of semiconductor band gap in determining solar cell performance and shows that band gaps between 0.7 and 1.6eV have efficiencies in close proximity to the theoretical maximum.

2.5.2 – Quantum efficiency

The photocurrent generated by a PV cell under illumination is dependent on incident light. This dependence is expressed by the so-called quantum efficiency (QE).

QE is defined as the ratio of the number of charge carriers collected by the PV cell to the number of incident photons with a given energy. It represents the probability that an incident photon of energy $E(\lambda)$ could deliver one electron to the external circuit and relates the PV cell response to the various wavelengths (or energies) belonging to incident light spectrum. If all the photons of a certain λ are absorbed and the resulting carriers are entirely collected, then the QE at that particular λ has a value of unity. The QE for photons with energy below the band-gap is obviously zero.

The ideal quantum efficiency plot versus incident wavelengths has a square shape, with a constant value across the entire spectrum of wavelengths measured. Nevertheless, the real QE is reduced by recombination which makes carriers not able to move into external circuit. So, the QE spectrum is related to the recombination mechanisms and reflects both device design and material quality.

In a PV cell, the short wavelengths response is provided mainly by the emitter region since high energy photons are absorbed at the front, closely to the cell surface. Consequently, the "blue" portion of the QE is strongly affected by surface recombination. Similarly, lower energy light is absorbed in the bulk of the cell. Thus, long wavelength QE (in the “red” portion of the spectrum) is affected by back surface quality, carrier diffusion length and cell thickness.

Two types of PV cell quantum efficiency are commonly distinguished: external quantum efficiency (EQE) and internal quantum efficiency (IQE). EQE is the fraction of incident photons that are converted to electrical current and refers to the efficiency with which photons adsorbed inside the cell can generate collectable carriers. IQE is instead the fraction of absorbed photons that are converted to electrical current and includes effects of optical losses such as transmission and reflection [5].

Mathematically, IQE and EQE are defined as follows:

$$EQE = \frac{I_{sc}(\lambda)}{qAf(\lambda)} \tag{2.9}$$

$$IQE = \frac{I_{sc}(\lambda)}{qA(1-s)(1-r(\lambda))f(\lambda)(e^{-\alpha(\lambda)x_{opt}} - 1)} \tag{2.10}$$

where s is the grid-shadowing factor, $r(\lambda)$ is the reflectance, $\alpha(\lambda)$ is the absorption coefficient, x_{opt} is the optical thickness of the solar cell and A is the PV cell area.

For example, figure 2.9 illustrates IQE and EQE of a typical crystalline silicon PV cell for incident wavelengths from 300 to 1200nm.

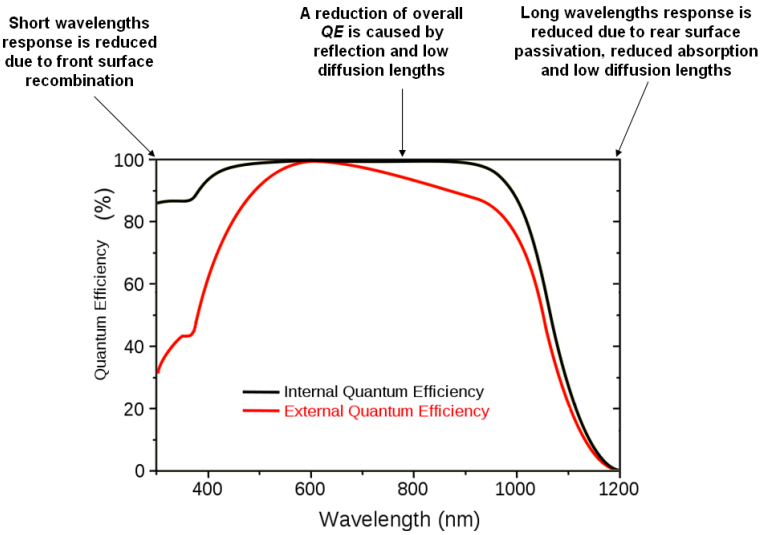

Figure 2.9 Crystalline Silicon PV cell IQE and EQE as function of incident wavelength.

Quantum efficiency does not give information about the fraction of power that is converted by the PV cell. Moreover, quantum efficiency is usefully expressed as a spectral function of photon wavelength or energy. Since some wavelengths are absorbed more effectively than others in most semiconductors, spectral measurements of quantum efficiency could give important information about the quality of the semiconductor bulk and surfaces.
Quantum efficiency is also called Incident-Photon-to-electron Conversion Efficiency (IPCE).

2.5.3 – Detailed balance limit

In 1960, Shockley and Queisser published an important paper in which the evaluation of the theoretical efficiency upper limit of *p-n* junction solar energy converters was presented [7]. A limiting efficiency, called the detailed balance limit, has been calculated for an ideal case in which the only recombination mechanism of hole-electron pairs was radiative. The efficiency was also calculated for the case in which radiative recombination was only a fixed fraction f_c of the total recombination, the rest being non-radiative. The general approach was to determine the current from the PV cell calculating the difference between the flux of photons absorbed from the sun and the flux of photons emitted by the solar cell. Efficiencies at the matched loads have been analyzed in function of band gap and f_c, assuming the sun and the cell as blackbodies with temperatures of 6000K and 300K, respectively.

The theoretical efficiency limit occurs in ideal PV cells made of a semiconductor material with a valence band and a more energetic conduction band separated by a band energy gap E_{gap}. Each band is able to develop separate quasi-Fermi levels, ε_{Fc} for the conduction band and ε_{Fv} for the valence band, to describe the carrier concentration in the respective bands. The two metallic contact Fermi levels ε_{F+} (contact to the conduction band on n^+-doped semiconductor) and ε_{F-} (contact to the valence band on p-doped semiconductor) are levelled, respectively, to the hole and the electron quasi-Fermi levels ε_{Fv} and ε_{Fc} at each interface. In equilibrium, the two quasi-Fermi levels become one.
The voltage V appearing between the two electrodes is given by the difference in the quasi-Fermi levels of majority carriers at the ohmic contact interfaces. With constant quasi-Fermi levels and ideal contacts, is

$$qV = \varepsilon_{Fc} - \varepsilon_{Fv} \tag{2.11}$$

Figure 2.10 shows the band diagram of the PV cell with its contacts [8].

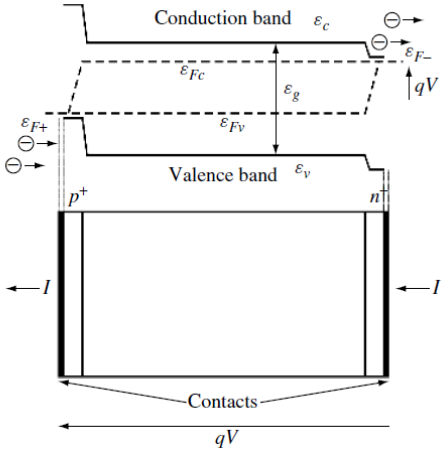

Figure 2.10 PV cell band diagram. [8]

In the ideal Shockley and Queisser cell, the mobility of the carriers is infinite, and the absorption of all photons above the band gap is complete. Photons are absorbed by electron–hole pair generation, pumping electrons from the valence to the conduction band. The opposite mechanism is also produced so that a conduction band electron can decay to the valence band and emit a photon, leading to a radiative recombination process, responsible for luminescent light emission. Many of luminescent photons having energy above the band gap are reabsorbed, leading to new electron–hole pair generations and balancing out the recombination. Only the recombination processes leading to the effective emission of a photon out of the semiconductor produce a net recombination.
Taking into account that the luminescent photons are emitted isotropically, only photons emitted near the cell surfaces (at distances in the range of the inverse of

the absorption coefficient) and directed towards the cell surface with small angles have probability to leave the semiconductor, and thus to contribute to the net radiative recombination.
In the ideal Shockley and Queisser calculation, any non-radiative recombination mechanism is assumed to be absent.
Total current extracted from the cell is equal to the difference between the electrons pumped to the conduction band by external photon absorption and the electrons falling again into the valence band emitting a luminescent photon. According to Plank's equation, this can be presented in an equation form as:

$$I/q = \phi_s - \phi_r = \int_{E_{gap}}^{\infty} (\varphi_s - \varphi_r) d\varepsilon \tag{2.12}$$

where ϕ_s and ϕ_r are the photon fluxes entering and leaving the solar cell, respectively. When the cell is properly contacted, this current is constituted by electrons that leave the conduction band through the highly doped n-contact. In a similar balance, in the valence band, *I/q* are also the electrons that enter the valence band through the highly doped p-contact.
The term in previous equation for unit-area cells are

$$\phi_s = a \frac{2\pi \sin^2 \theta_s}{h^3 c^2} \int_{E_{gap}}^{\infty} \frac{\varepsilon^2 d\varepsilon}{e^{\varepsilon / KT_s}} - 1 \tag{2.13}$$

for the cell facing the sun directly or

$$\phi_s = a \frac{2\pi}{h^3 c^2} \int_{E_{gap}}^{\infty} \frac{\varepsilon^2 d\varepsilon}{e^{\varepsilon / KT_s}} - 1 \tag{2.14}$$

for the cell under full concentration (using a concentrator without losses that is able to provide isotropic illumination) and

$$\phi_r = \xi \frac{2\pi}{h^3 c^2} \int_{E_{gap}}^{\infty} \frac{\varepsilon^2 d\varepsilon}{e^{(\varepsilon - qV) / KT_a}} - 1 . \tag{2.15}$$

where θ_s is the sun's semi-angle of vision (taking into account the sun's radius and its distance to Earth), a and ξ are the absorptivity and emissivity of the cell respectively, T_s is the sun temperature and T_a is the room temperature.
It can be proven that when the quasi-Fermi level split is uniform in the semiconductor bulk, then $a=\xi$. Assuming that the solar cell is thick enough and perfectly coated with antireflection layers so as to fully absorb any photon with energy above the band gap energy, then $a=\xi=1$ for these photons.

Equation 2.15 affirms that the temperature associated with the emitted photons is the room temperature T_a and that the chemical potential of the radiation emitted, μ_{ph}, is:

$$\mu_{ph} = \varepsilon_{Fc} - \varepsilon_{Fv} = qV \tag{2.16}$$

This occurs because the radiation is due to the recombination of electron–hole pairs, each one with a different electrochemical potential. Admitting that photons and electron–hole pairs are produced through the reversible equation electron + hole ↔ photon, equation (2.15) results as a consequence of equalling the chemical potentials before and after the reaction.
When the exponential of the Bose–Einstein function is much higher than one, the recombination term in equation (2.12) for full concentration can be written as:

$$\phi_r = \frac{2\pi}{h^3 c^2} \int_{E_{gap}}^{\infty} \varepsilon^2 e^{(\varepsilon - qV)/KT_a} d\varepsilon \ . \tag{2.17}$$

This equation is therefore valid for $E_{gap} - qV >> KT_a$. Within this approximation, the current–voltage characteristic of the solar cell takes its conventional single exponential appearance. In fact, this equation, with the appropriate factor $sin^2\theta_s$, is accurate in all the ranges of interest of the current–voltage characteristic of ideal cells under unconcentrated sunlight.
The Shockley and Queisser solar cell can reach an efficiency limit given by

$$\eta_{\max} = \frac{I(V_{\max})V_{\max}}{P_{in}} = \frac{qV_{\max}[\phi_s - \phi_r(qV_{\max})]}{P_{in}} = \frac{qV_{\max}[\phi_s - \phi_r(qV_{\max})]}{\sigma_{SB} T_s^{\ 4}} \tag{2.18}$$

where σ_{SB}=5.67x10^{-8}Wm^{-2}K^{-4} is the Stefan Boltzmann constant and the maximum is calculated optimising V.
Figure 2.11 shows the Shockley and Queisser ideal efficiency limit for a blackbody PV cell at T_a=300K, with a sun temperature T_s=6000K, as a function of energy gap. The curve (a) corresponds to the AM0 solar intensity (as observed outside the Earth's atmosphere), the curve (b) corresponds to light focused on the cell (by a mirror or a lens) at the maximum concentration [5] [6] [7] [8]. The maximum ideal efficiency for an energy gap of 1.1eV (corresponding to c-silicon energy gap), was found to be about 30% in the case of AM0 solar intensity.

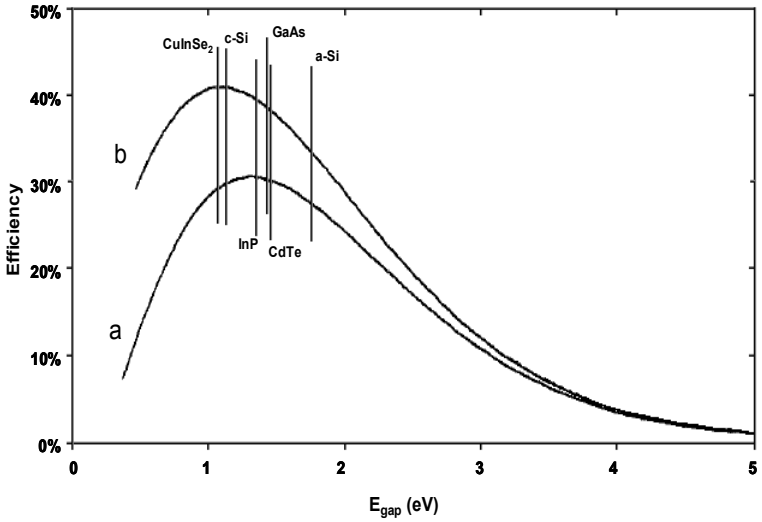

Figure 2.11 Shockley and Queisser efficiency limit for an ideal solar cell versus band gap energy for unconcentrated black body illumination and for full concentrated illumination. a) Unconcentrated 6000 K black body radiation (corresponding to AM0 solar intensity). b) Full concentrated 6000 K black body radiation ($7349 \cdot 10^4 W/m^2$). [7]

Real PV cells present a different behaviour respect to the predicted Shockley and Queisser limit, because the assumptions at the base of detailed balance calculation are not satisfied. The main reasons why real PV cells do not achieve ideal performance are the following:

- incomplete absorption of incident light. Photons are reflected from the front surface or from the contacts or could pass through the cell without being absorbed. This reduces the photocurrent
- no radiative recombination of photogenerated carriers. Excited charges could be trapped at defect sites and subsequently recombine before being collected. Recombination reduces both the photocurrent (decreasing carrier collection probability) and the voltage (increasing the dark current)
- voltage drop due to series resistance between the point of photo-generation and the external circuit.

2.6 – SILICON WAFER-BASED PV CELL MANUFACTRING PROCESS FLOW

There are a variety of processes for manufacturing silicon photovoltaic cells. In the following steps the simplest standard process flow of a silicon wafer-based cell is schematically described:

• Si substrate (either mono or poly-crystalline)

For silicon solar cell the starting wafer is generally from 200 to 500um thick with a standard size of 156x156mm^2 or 126x126mm^2. The wafer is typically *p*-type doped with small amounts of Boron (about 10^{16} atoms/cm^3).

• Saw damage etch

The starting wafer is "as cut". It is damaged and uneven due to the sawing on both surfaces. A strong alkaline etch cleans up the wafer and removes the damaged outer layer of silicon.

• Surface texturing

Silicon texturing is utilized to reduce surface reflectivity. The wafers are textured by chemical anisotropic etching. This process produces the development of micrometric relieves onto silicon surface, generally of pyramidal form. Random pyramidal texturing of substrates allows to increase the short-circuit current of the cell.

• Emitter Diffusion

The emitter is formed through doping impurities diffusion. The process takes place normally in a tube furnace. In the case of n^+-p cell (emitter n^+-doped) the more used dopant species is Phosphorus. It is usually supplied by a phosphorus-rich glass which is deposited in-situ ($POCl_3$ diffusion). In this process the temperatures are within 800÷1000°C.

• Edge Isolation

The edge isolation process removes the phosphorous diffusion around the edge of the cell so that the front emitter is electrically isolated from the rear. The edge is etched by a highly reactive plasma gas (CF_4 and O_2) to remove the junction.

• Anti-reflection coating (ARC)

Through a combination of favourable refractive index, and thickness, this layer serves to guide light into the solar cell. Without this layer, much of the light would simply bounce off the surface. An antireflection coating of silicon nitride (SiN_x) or silicon oxide (SiO_2) is typically used to passivate cell surface.

SiN_x is usually deposited using plasma-enhanced chemical vapor deposition (PECVD). Generally, the nitride deposited has a thickness of 80 nm and it is deposited in a low-pressure reactor. The nitride is an excellent front surface passivation and increases the amount of light coupled into solar cell.

SiO_2 standard production method is based on a high temperature thermal process immediately sequential at emitter diffusion. SiO_2 is an effective passivating material only for mono-crystalline wafers. In microcrystalline or polycrystalline silicon, SiO_2 coating is unsuccessful since grain edges necessitate hydrogen presence to passivate superficial layer and avoid electrical charges recombination.

• Screen-Printing rear and front contact

A mask (mesh screen) is lowered onto the cell front with a metallic past layer. A squeegee drags across the screen forcing metal paste through holes in the screen print mask. The screen is after removed leaving a thick of wet metal paste. The paste is dried to drive off solvents.

On the rear, a full coverage layer of Al or Ag paste is commonly used. On the front, a finger pattern (used to prevent shading) is screen printed using Ag paste.

• **Firing**

The wafers are subjected to rapid thermal process by passing through a conveyor belt furnace. During this process, the Ag on the front penetrates through the ARC and contacts the *n*-type emitter. The Al on the rear forms an alloy in which the phosphorous doped layer on the back is completely dissolved. After cooling, a p^+-doped Al layer is created. This forms a back surface field (BSF), which reduces the electron-hole recombination at the cell back surface and thereby increase the cell efficiency.

Process steps described above are illustrated in the following figure 2.15.

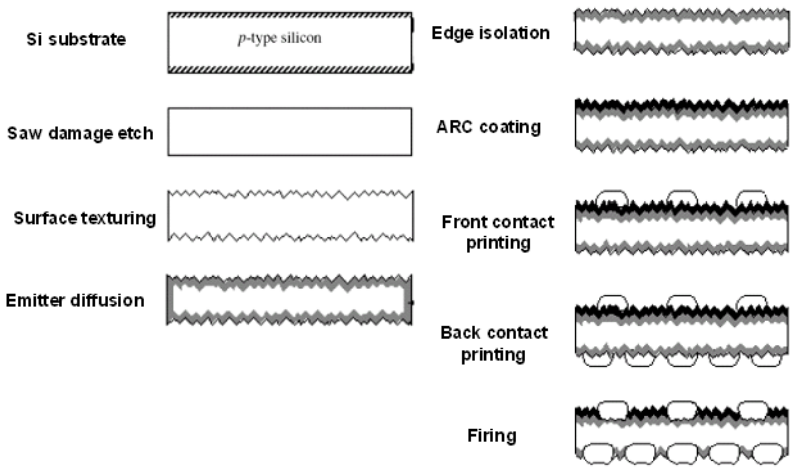

Figure 2.12 Silicon wafer-based PV cell typical process flow. [8]

The structure of a typical silicon wafer-based PV cell is reported in figure 2.13.

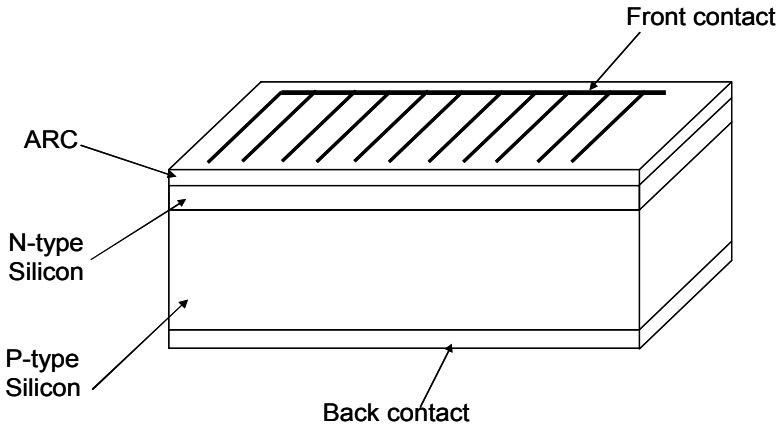

Figure 2.13 Structure of a standard Silicon wafer-based solar cell.

References

[1] Green M, Solar Cells: *Operating Principles, Technology, and System Applications* (1982).

[2] Standard ASTM E891-92*, Standard for Terrestrial Solar Direct Normal Solar Spectral Irradiance Tables for Air Mass 1.5,* American Society for Testing and Materials, West Conshocken, PA, USA.

[3] Sze S, Physics of Semiconductor Devices, 2nd Edition, John Wiley & Sons, New York, NY (1981).

[4] Jury MM. - *Simulation, fabrication et analyse de cellules photovoltaïques à contacts arrières interdigités* (2005).

[5] Castañer L., *Solar Cells: Materials, Manufacture and Operation* (2006).

[6] Nelson J., *The Physics of Solar Cells* (2007).

[7] W.Shockley and H.J.Queisser, Detailed *Balance Limit of Efficiency of p-n Junction Solar Cells* (1961).

[8] Luque A., Hegedus S., *Handbook of photovoltaic science and engineering* , John Wiley & Sons, New York, NY (2003).

3. Simulation of Photovoltaic Cells Electrical Behaviour

3.1 – INTRODUCTION

Whatever should be the structure of a PV cell, the optimization of its structural parameters is necessary to get the higher achievable efficiency. With this purpose, a simulation program of PV devices electrical behaviour has been developed for exploring the full range of silicon wafer-based cells design alternatives to find the best flow for the manufacturing process.
The cell parameters to be optimized (as thickness, doping profiles, metal contacts configuration and material quality) are several and often interdependent between themselves. Consequently, the device optimization includes the study of the influence of each parameter on electrical characteristic in order to obtain the configuration giving the maximum efficiency. The realized simulation program has been used to analyze the most important parameters determining silicon PV cell performance with the purpose of improving physical and geometrical factors to maximize photogeneration and minimize electrical losses.
The use of a simulation program provides several advantages in terms of cost saving and response time velocity: it permits to avoid the fabrication of numerous prototypes having different parameters, it is independent from used technology and it allows investigating in real time the influence of each parameter.

3.2 – ELECTRICAL MODEL USED FOR THE SIMULATION

The simulation accuracy depends strongly on the physical model used to describe the PV cell electrical functioning. As extensively reported in equation (2.3), the PV cell output current I is given by the relation:

$$I(V) = I_{ph} - I_D\,(V + IR_s) - \frac{V + IR_s}{R_{sh}} \tag{3.1}$$

where I_{ph} is the photogenerated current, R_s and R_{sh} are the series and the shunt resistances respectively and $I_D(V)$ is the characteristic of the diode appearing inside the PV cell equivalent circuit (figure 2.6) and constituted by the *n-p* junction.
The developed simulation program is based on the numerical resolution of the equation

$$I(V) - I_{ph} + I_D(V + IR_s) + \frac{V + IR_s}{R_{sh}} = 0 \tag{3.2}$$

using the cell manufacturing parameters as input data. The algorithm calculates the photogenerated current I_{ph} and the diode characteristic I_D such to find the *(I,V)* couples which solve equation (3.2) inside the entire voltage range of cell functioning.
The photogenerated and the diode currents are given by complex mathematical expressions deriving from the Poisson's equation and the hole and electron continuity equations. These three fundamental equations of charge transport inside the semiconductor describe extensively the PV cell working and contain terms depending on PV cell structure, material properties and operating conditions. Therefore, an accurate study of the cell electrical behaviour requires a detailed examination of these terms and a rigorous treatment of all current components.
Despite the complexity of the expressions describing the PV cell functioning, the basic operating principles are simple. Electron–hole pairs are created inside the solar cell as a result of absorption of the incident photons coming from the sun. The objective of the PV cell design is to optimize the photogenerated carriers' collection before they are lost on account of recombination.

3.2.1 – Photogenerated current

I_{ph} is the current due to the net absorbed flux coming from sun. In order to estimate the cell photocurrent, both events of charge carriers generation and recombination must be taken into account. The rate of creation of electron–hole pairs G (number of electron–hole pairs per cm^3 per second) through the light absorption in the semiconductor is calculated, as a function of position x inside the cell, using the formula:

$$G(x) = (1 - s)\int_{\lambda} (1 - r(\lambda)) f(\lambda) \alpha(\lambda) e^{-\alpha x} d\lambda \tag{3.3}$$

where s is the grid-shadowing factor depending on front contact design, $r(\lambda)$ is the reflectance, $\alpha(\lambda)$ is the absorption coefficient, $f(\lambda)$ is the incident photon flux (number of photons incident per unit area per second per wavelength), and the sunlight is assumed to be incident at $x=0$. The absorption coefficient has been expressed in terms of the light's wavelength through the relationship $hv=hc/\lambda$. The photon flux, $f(\lambda)$, is obtained dividing the incident power density at each wavelength by the photon energy. Obviously, only photons with $\lambda \leq hc/E_{gap}$ generate electron-hole pairs [1].
Simulation program calculates I_{ph} by the sum of the contributions to the total current coming from the light absorbed inside three separated regions: the

depletion region and the two quasi-neutral regions (*n*-type and *p*-type) in accordance with the values assumed by the position *x* in equation (3.3).
If photons absorbing occurs inside the depletion region, all the electron-hole pairs photogenerated are assumed to be separated by the junction intrinsic electric field and collected at metallic contacts.
If, instead, absorbing occurs inside quasi neutral regions, recombination processes cause the loss of mobile charges by several removal mechanisms and thus not all electron-hole pairs photogenerated contribute to I_{ph}. Only the portion of photogenerated carriers reaching the depletion layer by diffusion without recombining can be separated and then collected at contacts, taking part in photocurrent. The "size" of this portion depends on carriers' lifetime and it is calculated as a function of silicon quality, doping concentration, carriers mobility and surfaces (front and back) structures.

3.2.2 – Diode characteristic

$I_D(V)$ is computed taking into account the different currents flowing through the diode of figure 2.6, in accordance with the following relation:

$$I_D(V) = I_{D1}(V) + I_{D2}(V) = I_{01}\left(e^{\frac{q(V+IR_s)}{KT}} - 1\right) + I_{02}\left(e^{\frac{q(V+IR_s)}{2KT}} - 1\right) \quad (3.4)$$

I_{01} is the dark saturation current due to carrier diffusion in the quasi-neutral regions and I_{02} is the dark saturation current due to recombination in the space-charge region.
The direction of the current source is opposed to the current flow of the diode: it follows that diode has a forward-bias. At low voltage forward-bias, the recombination current of minority carriers in the depletion region dominates and major contribution to total current I_D is given by the term multiplying I_{02}. As voltage increases, the diffusion current increases too and I_{01} contribution to I_D progressively prevails. Moreover, at higher voltages, the surplus carriers concentration exceeds the doping in the base region and high-level injection occurs.
The diode characteristic is fundamental to define the PV cell performance because it determines the maximum voltage difference across the cell (the open circuit voltage V_{oc}) and, consequently, the squareness of the cell *I-V* characteristic (the fill factor *FF*). As shown in equation (2.5), the open-circuit voltage is logarithmically proportional to the photogenerated current and to the reciprocal of the reverse saturation currents. Therefore, a reduction of I_{01} and I_{02} increases both the open-circuit voltage and the fill factor, improving cell efficiency.
I_{01} is calculated using the following equation:

$$I_{01} = qA\frac{n_i^2 D_p}{N_D L_p}\left\{\frac{\frac{D_p}{L_p}\sinh\left[\frac{W_N - x_n}{L_p}\right] + S_F\cosh\left[\frac{W_N - x_n}{L_p}\right]}{\frac{D_p}{L_p}\cosh\left[\frac{W_N - x_n}{L_p}\right] + S_F\cosh\left[\frac{W_N - x_n}{L_p}\right]}\right\} + qA\frac{n_i^2 D_n}{N_A L_n}\left\{\frac{\frac{D_n}{L_n}\sinh\left[\frac{W_p - x_p}{L_n}\right] + S_{BS}\cosh\left[\frac{W_p - x_p}{L_n}\right]}{\frac{D_n}{L_n}\cosh\left[\frac{W_p - x_p}{L_n}\right] + S_{BS}\cosh\left[\frac{W_p - x_p}{L_n}\right]}\right\} \quad (3.5)$$

where A is the area of the cell, W_N and W_P are the n-type and p-type layers thickness respectively, D_n and D_p the hole and electron diffusion coefficients, L_p and L_n are the hole and the electron diffusion lengths, S_F and S_{BS} are the frontal and the back side surface recombination velocities, x_n and x_p are the depletion region thicknesses inside the n-type and the p-type layers, n_i is the intrinsic carrier concentration, N_D and N_A are the donors and acceptors concentrations.
I_{02} is computed using equation

$$I_{02} = qA\frac{W_D n_i^2}{\tau_D} \quad (3.6)$$

with W_D depletion region thickness and τ_D carriers lifetime inside the depletion region. I_{02} is bias dependent since W_D is a function of applied voltage.
Equations (3.5) and (3.6) explicitly show the n-p junction design factors determining I_{01} and I_{02} which may be adjusted to modify the diode characteristic [1][2].

3.3 – SIMULATIONS RESULTS

The electrical behaviour of a wafer-based silicon PV cell has been studied varying all its structural parameters, beginning from the reference n^+-p cell described in Table 3.1. Simulations have been performed in order to evaluate the influence of silicon quality, surfaces treatments, doping concentration and layers thickness on the cell I-V characteristic in terms of photogenerated current I_{ph}, open circuit voltage V_{oc} and, finally, efficiency η.

Table 3.1 - Silicon PV cell model parameters	
Parameter	**Value**
Material	Float Zone silicon
A	(15.6x15.6)cm^2
W_N	350 nm
W_P	300 µm
N_D	$1 \cdot 10^{20}$ cm^{-3}
N_A	$1 \cdot 10^{15}$ cm^{-3}
R_s	0
R_{sh}	∞
S_F	$3 \cdot 10^4$ cm/s
S_{BS}	100 cm/s

If not differently specified, values tabulated in Table 3.1 have been used as simulations input data. Other fixed inputs were the incident power and silicon absorption coefficient plotted in figure 2.1 (AM1.5g solar spectrum) and figure 2.3 respectively. Moreover, all simulations refer to room temperature (300K) and carriers mobility reported in figure 3.1 as a function of impurity concentration [3].

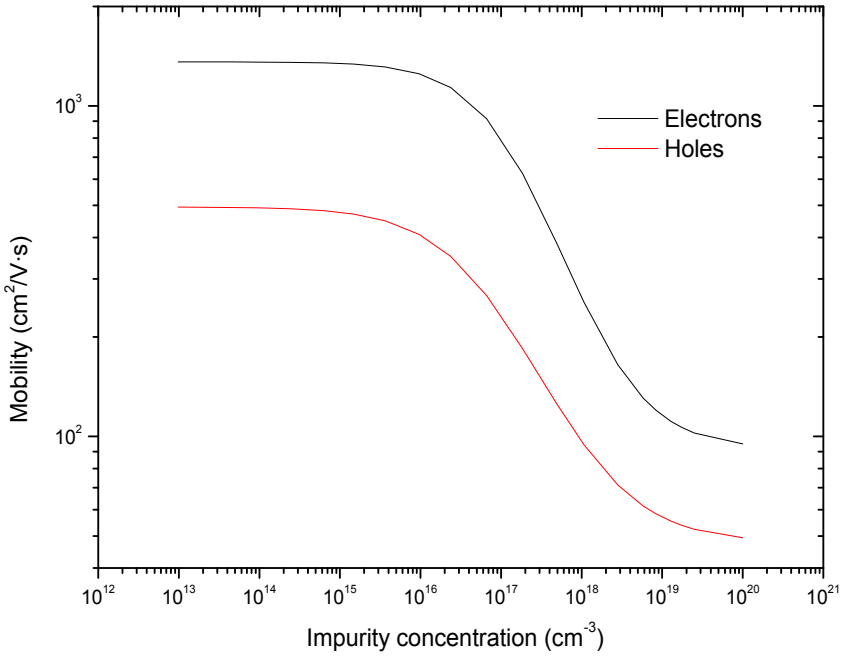

Figure 3.1 Electron (black line) and holes (red line) mobilities in Silicon for T=300K.

At low and moderate doping, electrons present mobility about three times higher than holes, both limited by phonon scattering. Impurity scattering dominates for higher doping densities. Carrier–carrier scattering affects transport properties in highly injected material.

3.3.1 – Silicon quality

Silicon quality is one of the key parameters determining PV cell efficiency because charge carriers lifetime is strongly dependent on the quantity of impurities contained inside the semiconductor.

The main recombination mechanisms are radiative, Auger and trap assisted (in the bulk or at surface). However, recombination in silicon PV cells is dominated by the existence of traps in the forbidden gap due to the presence of defects. In fact, Auger recombination (which is independent of impurity density) becomes significant only at high carrier concentration being the related lifetime inversely proportional to the carrier density; band-to-band radiative direct recombination is relatively unimportant and quantitatively negligible because the associated lifetime is extremely high. Therefore, carriers' lifetime τ in silicon is tightly connected with the impurity level and the defects concentration giving rise to recombination sites: as a consequence, it increases improving material quality. A sufficiently high lifetime is crucial to achieve high performance of crystalline silicon PV cells.

The contribution of silicon quality on cell performance has been studied simulating the PV cell characteristic at carriers' lifetime variation. In Figure 3.2 is shown the electron lifetime as a function of acceptors dopant concentration, in the specific case of three different semiconductor qualities. Higher τ curve (blue line) represents the typical of the best commercially available float zone silicon (FZ), moderate τ curve (red line) represents the typical of Czochralski-grown silicon (CZ) and the lower τ curve (black line) represents a poor-quality material[4][5][6].

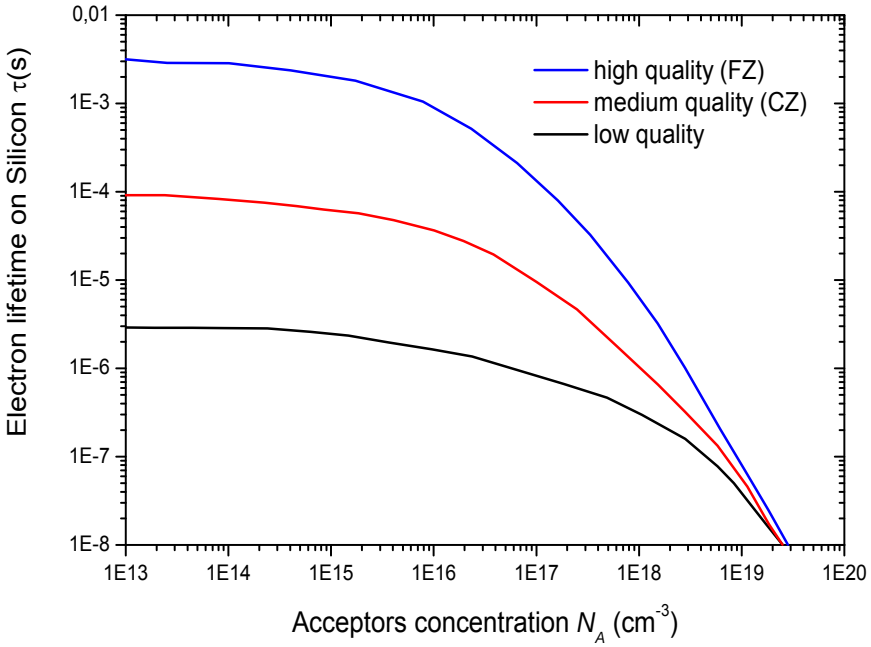

Figure 3.2 Electron lifetime on silicon as a function of dopants concentration.

FZ silicon is characterized by an extreme crystalline perfection and by the lowest contamination levels of both metallic and light (O, C, N) impurities. This translates into the longest lifetimes, belonging to the millisecond range. Czochralski material is also a perfect crystal but it contains a moderate concentration of Oxygen that affects lifetime compared to FZ. Low quality silicon is material containing high concentration of impurities. It shows lifetimes in the microsecond range.

The effect of semiconductor quality on PV cell electrical behaviour is revealed in figure 3.3, where the *I-V* characteristics related to these three silicon typologies are reported. Increasing silicon quality carriers' lifetime enhances and, as result, both I_{ph} and V_{oc} are amplified. The global effect of material quality on cell efficiency is highlighted in figure 3.4.

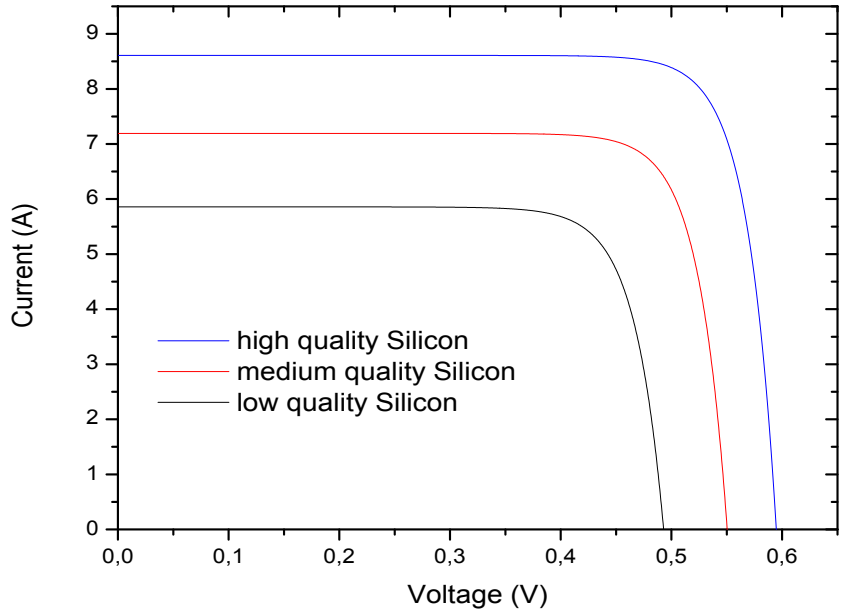

Figure 3.3 Comparison between the silicon PV cell *I-V* characteristics calculated for three different semiconductor qualities. Increasing quality, both I_{ph} and V_{oc} amplify as consequence of carriers' lifetime enhancement.

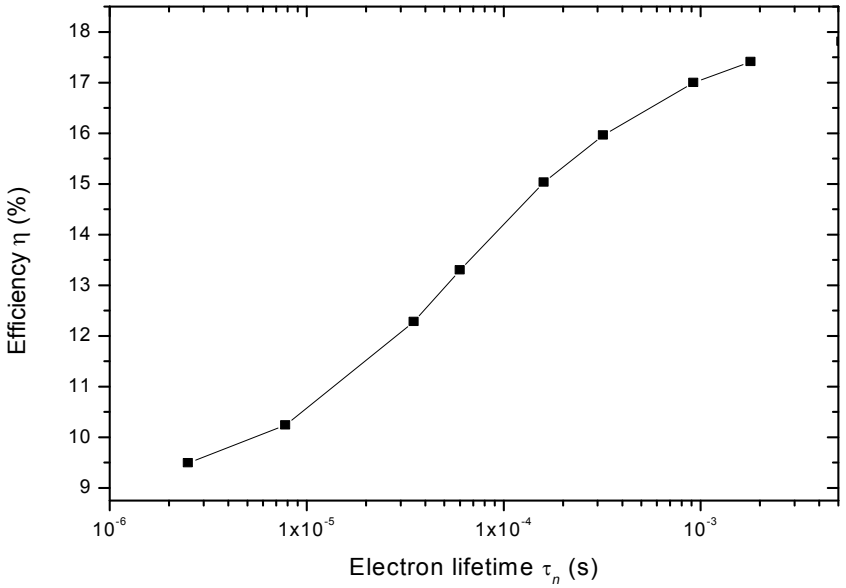

Figure 3.4 Efficiency versus electron lifetime. The highest efficiencies have been achieved with mono-crystalline FZ silicon but it is too much expensive and not easily available. CZ material allows very high efficiencies and it is much more cost-effective than FZ. Poor-quality material shows very low efficiencies and cannot generate enough PV energy to justify the costs of the total PV system.

The highest efficiencies have been achieved with mono-crystalline float zone silicon. However FZ silicon is too much expensive and not easily available. So, the FZ cost/benefit ratio is not always profitable.
Poor-quality material, on the contrary, shows very low efficiencies and cannot generate enough PV energy to justify the costs of the total PV system.
CZ material allows very high efficiencies and it is much more cost-effective than FZ. For these reasons CZ silicon represents the best material to be used for silicon PV cell, because it guarantees accessibility, suitable costs and high efficiency.

3.3.2 – Emitter thickness

In silicon PV cells the emitter is commonly made by diffusion of *n*-type (*p*-type) impurities into *p*-type (*n*-type) semiconductor wafer. Impurities diffusion creates the doped layer needed to generate the *n-p* junction indispensable to give rise to photovoltaic effect. Emitter is also necessary to make a selective contact under metal lines and to lower front contact resistance. It extends all across front surface acting as a transparent electrode by offering to minority carriers in the substrate a low resistance path to the contacts.
By means of the simulation program, the effects of emitter thickness (or junction depth) W_N and dopant (donors) concentration N_D on PV cell performance have been studied. Figure 3.5 reports the calculated photogenerated current obtained varying the W_N.

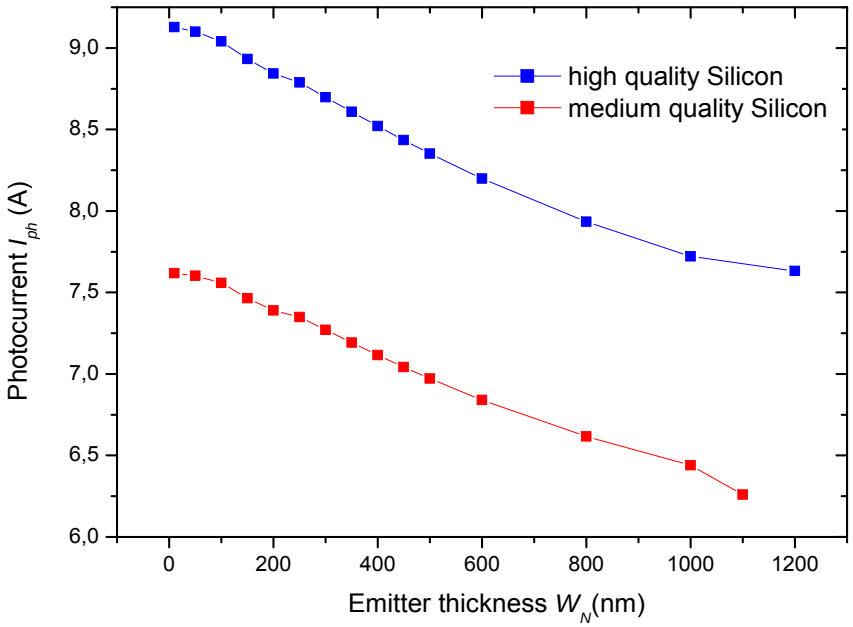

Figure 3.5 Photocurrent versus emitter thickness. Increasing the emitter thickness the photocurrent always diminishes. As thickness increases, emitter absorbs progressively more and more light but generates no photocurrent because of high front surface recombination velocity that makes the light absorbed inside emitter poorly collected.

As shown, increasing the emitter thickness the photocurrent always diminishes. This result is due to the high front surface recombination velocity that makes the light absorbed inside emitter region poorly collected. As thickness makes bigger, emitter absorbs progressively more and more light but generates no photocurrent, degrading cell performance. Consequently, the collection of carriers near the surface implies that the emitter must be thin compared to the minority carrier diffusion length ($W_N < L_p$) because it is very sensitive to surface recombination.

3.3.3 – Emitter doping level

The effects of varying emitter dopant concentration are illustrated in figures 3.6, 3.7 and 3.8 which report the calculated photocurrent, open circuit voltage and efficiency respectively as a function of doping level. Computations have been performed for the highest silicon quality (FZ).

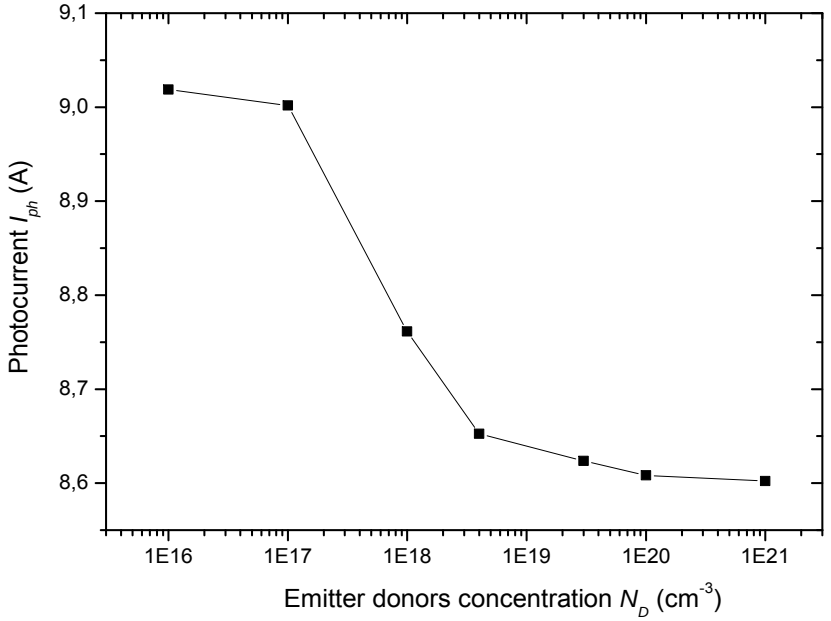

Figure 3.6 Photocurrent versus emitter doping. I_{ph} diminishes increasing impurities concentration.

The emitter concentration influences several parameters determining photocurrent, as carriers' mobility and diffusion lengths or depletion region width. The resulting effect is a photocurrent decreasing for increasing concentration.

On the other hand, figure 3.7 shows that elevating the dopant concentration an improving of the cell open circuit voltage is obtained. This is due to both the reduction of the minority carrier recombination and the growing of the *n-p* junction potential barrier. However, over concentrations of about 10^{19}cm^{-3}, V_{oc} saturates to its maximum value.

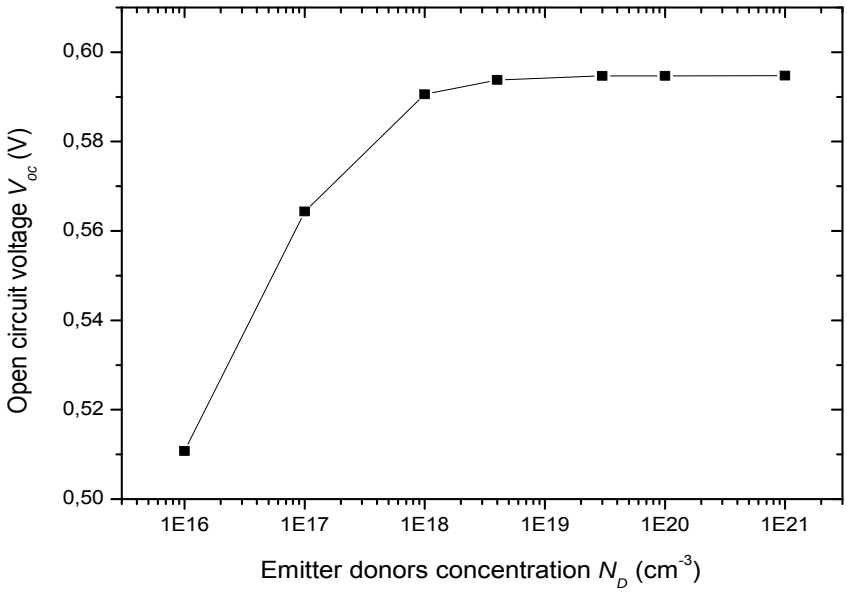

Figure 3.7 Open circuit voltage versus emitter doping. Elevating the dopant concentration an increment of V_{oc} is obtained. This is due to both the reduction of the minority carrier recombination and the growing of the *p-n* junction potential barrier.

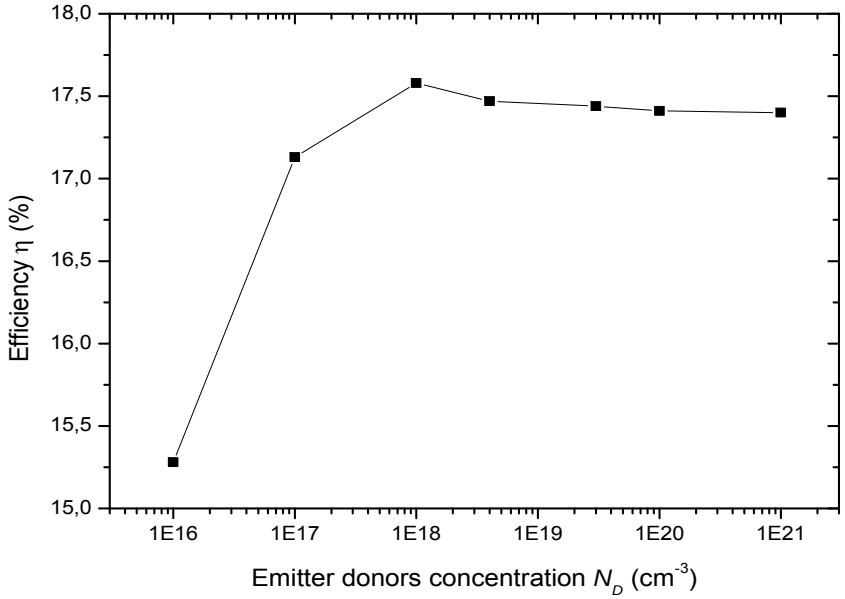

Figure 3.8 Efficiency as a function of emitter doping. Best efficiencies have been obtained for impurities concentrations N_D>10^{18}cm^{-3}.

Figure 3.8 illustrates that the global effect of I_{ph} and V_{oc} trends, as a function of donors' density, is a cell efficiency improvement increasing emitter concentration. As proved, in the optimal design the emitter must be highly doped with impurities concentration N_D>10^{18}cm^{-3}.

3.3.4 – Base thickness

The choice of the most advantageous base thickness is connected to the structure and the quality of the material and involves several considerations. Increasing base thickness light absorption always increases too, enhancing charge generation. Nevertheless, charge collection is strongly dependent on back surface recombination velocity S_{BS} and carriers diffusion length (carriers' lifetime). In cells with diffusion lengths longer than thickness, if S_{BS} is lower than D/L for the minority carriers (around 250 cm·s^{-1} for the best cells), thinning the cell decreases recombination and vice versa.

If the diffusion length is lower than thickness, the cells are moderately not sensitive to thinning because they are not affected by rear surface recombination.

Figure 3.9 shows these effects: the relationship between I_{ph} and base thickness is reported in the case of three reference cells referred to FZ silicon (blue squares), CZ silicon (red squares) and low quality silicon (black squares) respectively.

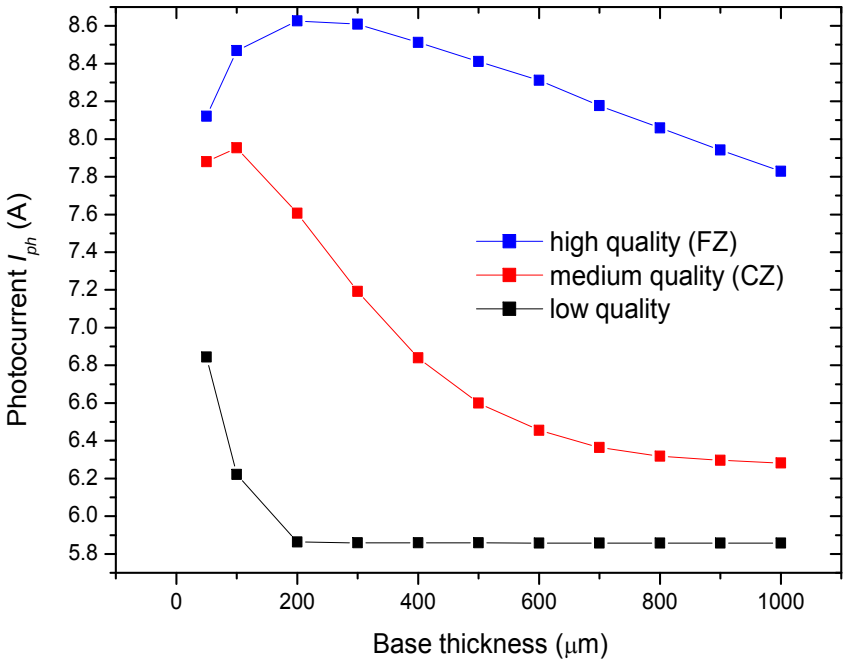

Figure 3.9 Photocurrent versus base thickness. Increasing base thickness light absorption always increases too, enhancing charge generation. Nevertheless, in cells with diffusion lengths longer than base thickness, if S_{BS} is lower than D/L for the minority carriers, thinning the cell recombination decreases and charge collection is enhanced. If the diffusion length is lower than thickness, the cells are moderately not sensitive to thinning because they are not affected by rear surface recombination.

Wafer thickness in the range of 200÷300μm ensures PV cell high performance for the more suitable silicon typologies. However, an additional important issue to be considered is the high price of the material: for this reason, the actual industrial trend is directed toward a wafers thinning to save expensive silicon and to reduce the production costs [7].

3.3.5 – Base doping level

The optimal substrate doping depends on cell structure and recombination mechanisms. Generally, increasing base concentration, carriers' lifetime and mobility are degraded and the recombination rate is amplified. This produces a significant declining of photocurrent in the case of heavily doped substrates.
On the other hand, diminishing base doping the diode direct current increases (according to equation 3.5) and the V_{oc} is reduced.
Figure 3.10 and figure 3.11 show the photocurrent and the open circuit voltage respectively, as function of base doping concentration.

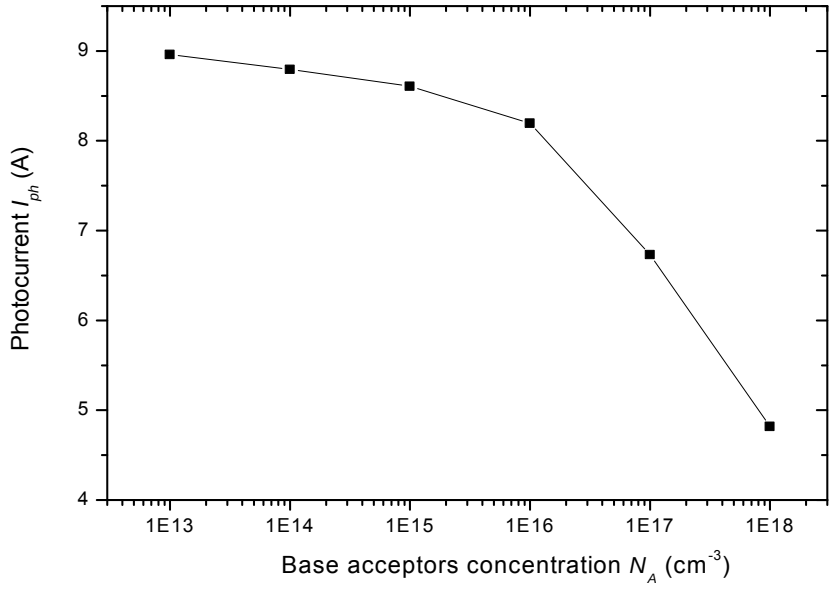

Figure 3.10 Photocurrent versus base doping. Increasing base concentration, photocurrent diminishes as a result of a carriers' lifetime and mobility degradation.

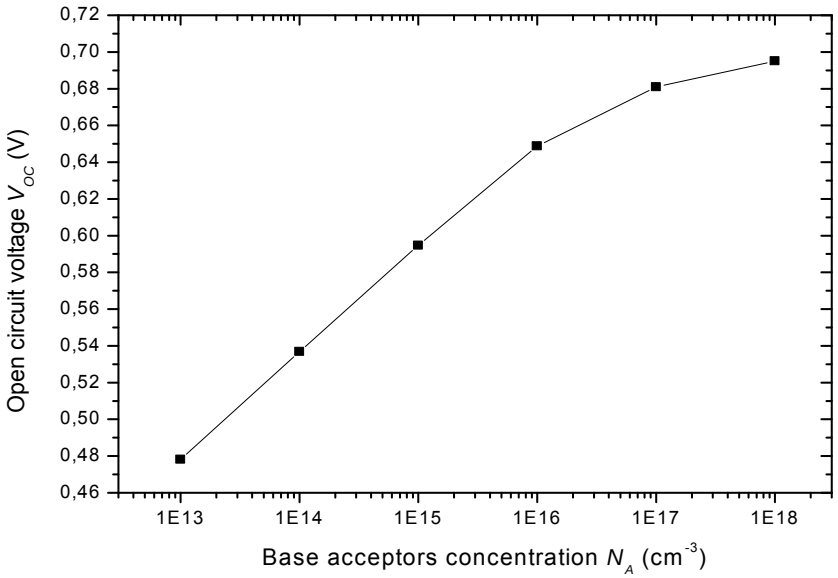

Figure 3.11 Open circuit voltage versus base doping. Decreasing acceptors concentration the diode direct current increases and the V_{oc} diminishes.

The highest values of I_{ph} and V_{oc} occur at different dopant density, consequently the doping optimization could not be made to obtain simultaneously the maximum for both parameters. Figure 3.12 demonstrates that the best efficiency values could be reached for acceptors concentration within the interval $10^{15} \div 10^{16} cm^{-3}$.

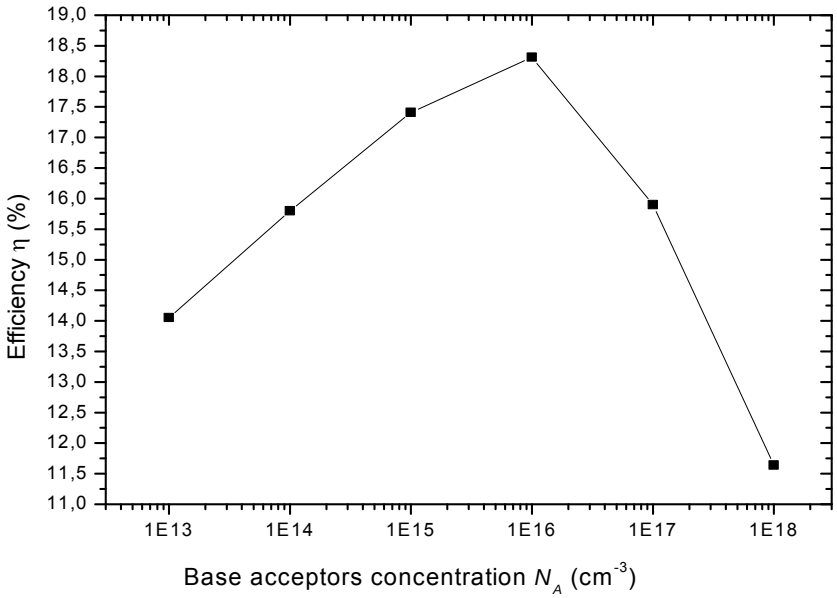

Figure 3.12 Efficiency versus base doping. Best efficiency values could be reached for acceptors concentration within the interval $10^{15} \div 10^{16} cm^{-3}$.

Figure 3.13 is a 3-D plot showing the combined effect of emitter and base doping variation. The highest efficiencies have been obtained for emitter concentrations $N_D \geq 10^{19}cm^{-3}$ and base concentrations $N_A \leq 10^{16}cm^{-3}$.

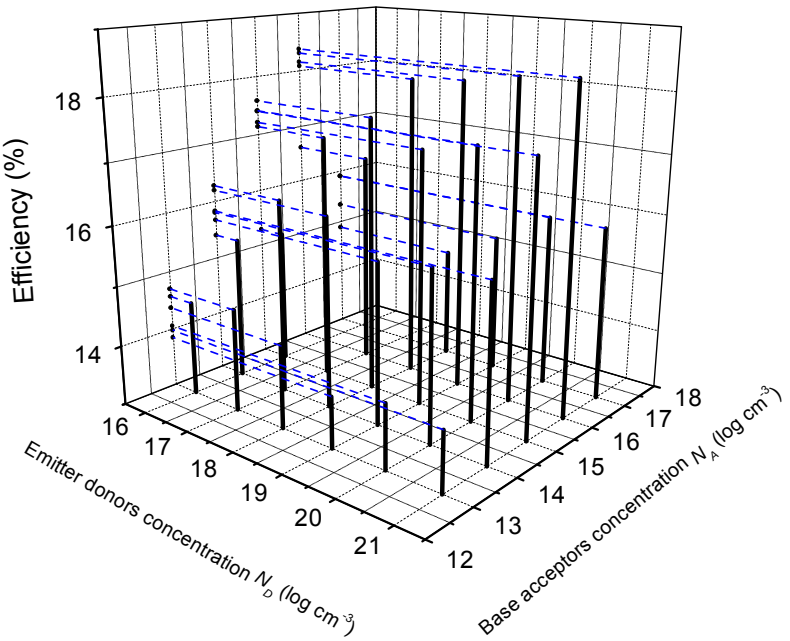

Figure 3.13 3-D plot reporting efficiency as a function of both emitter and base doping. The highest efficiencies have been obtained for emitter concentrations $N_D \geq 10^{19}cm^{-3}$ and base concentrations $N_A \leq 10^{16}cm^{-3}$.

3.3.6 – Back surface recombination velocity

Back contact of industrial silicon PV cells is usually made by printing, and subsequently firing an Aluminium conductive paste, containing Ag. Thus, a more heavily doped layer at back surface of the *p*-type base is formed. This introduces a p^+-p junction and forms a back surface field representing a potential barrier to the minority electrons. This back surface field reflects electrons and reduces considerably the effective rear surface recombination velocity S_{BS} increasing photocurrent I_{ph}. The p^+-p junction also adds to the intrinsic bias of the cell enhancing the open circuit voltage V_{oc}.

The effects of the back surface field recombination velocity on PV cell performance are illustrated inside the following figures 3.14 and 3.15.

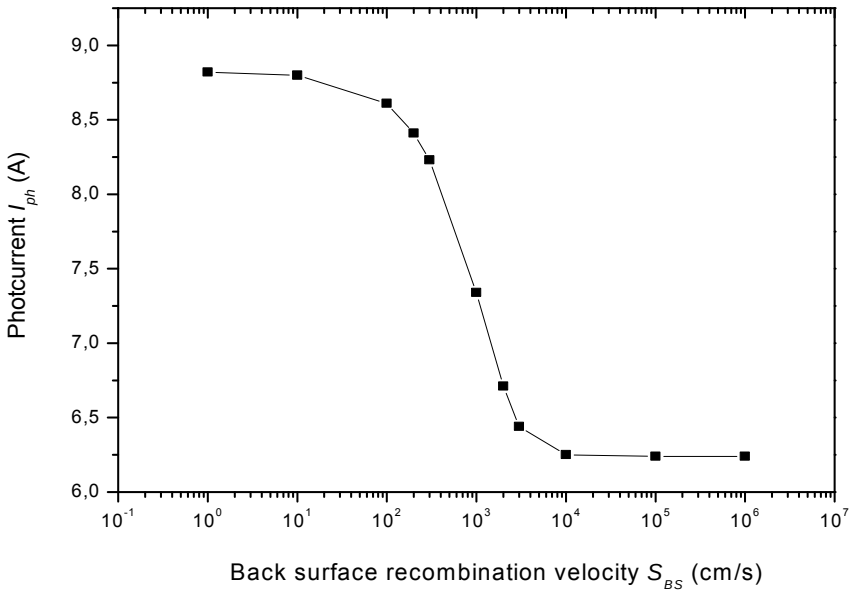

Figure 3.14 Calculated photocurrent versus back surface recombination velocity.

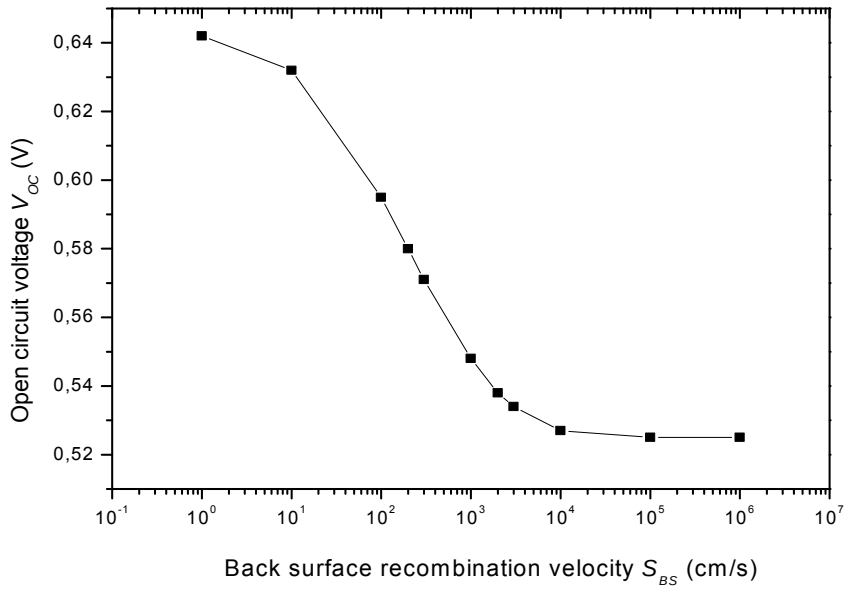

Figure 3.15 Calculated open circuit voltage versus back surface recombination velocity.

The thin more heavily doped region at the back of the base region keeps minority carriers away from the back ohmnic contact and increase their chances of being collected, improving I_{ph}, V_{oc} and, as a consequence, cell efficiency.

3.3.7 – Parasitic resistances

As described inside paragraph 2.3, in a real cell the power is dissipated through the resistance of the contacts and through leakage around the edges of the device. These effects are equivalent electrically to two parasitic resistances in series R_s and in parallel R_{sh} respectively with the cell (figure 2.6). The series resistance is due to the resistance of the cell material to current flow, particularly from resistive contacts. The parallel shunt resistance is caused by leakage of current through the cell, around the edges of the device and between contacts of different polarity.

The effects of R_s and R_{sh} on the PV cell electrical characteristic could be approximately evaluated deriving equation (3.2) and assuming the I_D derivatives $dI_D/d(V+IR_s)=0$ for $V+IR_s=0$ and $[dI_D/d(V+IR_s)]^{-1}=0$ for $V+IR_s=V_{oc}$. In these conditions, the following relationships are valid:

$$\left.\frac{dI}{dV}\right|_{V=0} = -\frac{1}{R_s + R_{sh}} \tag{3.7}$$

$$\left.\frac{dI}{dV}\right|_{V=V_{oc}} = -\frac{1}{R_s} \tag{3.8}$$

Equations (3.7) and (3.8) highlight the influence of the parasitic resistances on the slope of the *I-V* cell characteristic, both for $V=0$ and $V=V_{oc}$. This influence is graphically showed in figure 3.16 and 3.17 where the reference cell *I-V* characteristics calculated varying R_s and R_{sh} respectively are plotted.

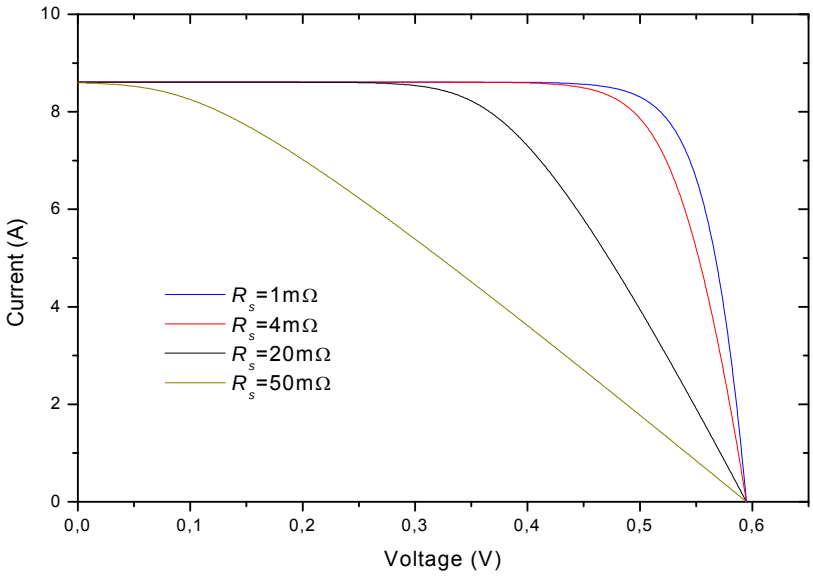

Figure 3.16 Comparison between the *I-V* characteristics of Silicon PV cells having different values of R_s. Series resistance modifies the slope of the *I-V* curve for $V=V_{oc}$. The result of increasing R_s is to reduce the area of the maximum power rectangle compared to $V_{oc}I_{sc}$.

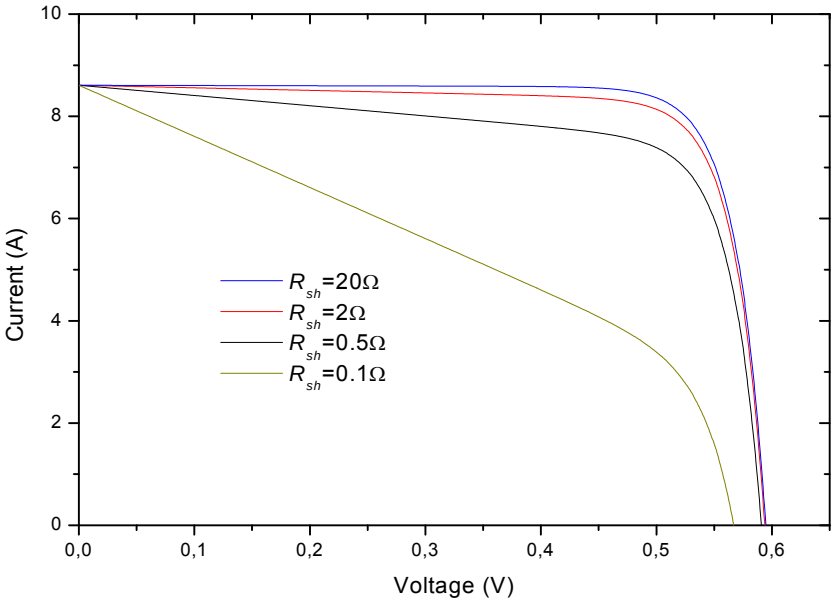

Figure 3.17 Comparison between the *I-V* characteristics of Silicon PV cells having different values of R_{sh}. Shunt resistance modifies the slope of the *I-V* curve for *V=0*. The result of diminishing R_{sh} is to reduce the area of the maximum power rectangle compared to $V_{oc}I_{sc}$.

The result of increasing R_s and reducing R_{sh} is to reduce the area of the maximum power rectangle compared to $V_{oc}I_{sc}$, and, thus, to reduce the fill factor *FF*. The shunt resistance reduces V_{oc} and has no effect on the short-circuit current I_{sc}; on the contrary, the series resistance has no effect on the V_{oc} but reduces I_{sc}.
The consequences in terms of efficiency are illustrated in following figures 3.18 and 3.19. Both parasitic resistances represent two important factors influencing significantly cell performance. Series resistance, in particular, is a critical parameter because a variation of only some mΩ in a typical industrial cell (surface area 15.6x15.6cm^2) is sufficient to diminish drastically the efficiency.
Graphs explain that shunt resistance (connected especially to edge isolation process) must be of the order of 10÷100Ω and series resistance (depending strongly on front contact process) must be as low as few mΩ.

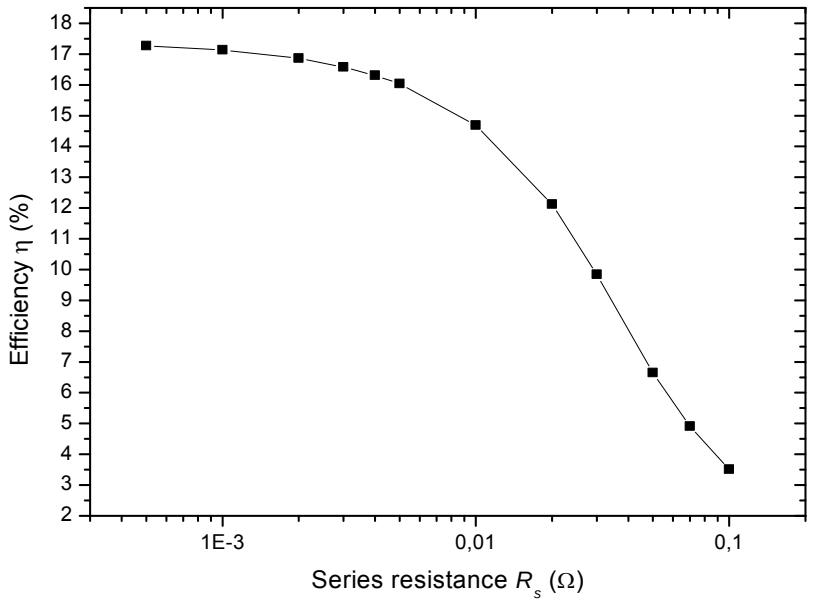

Figure 3.18 Calculated efficiency versus R_s. Series resistance must be as low as few mΩ. A variation of only some mΩ is sufficient to diminish drastically the cell efficiency.

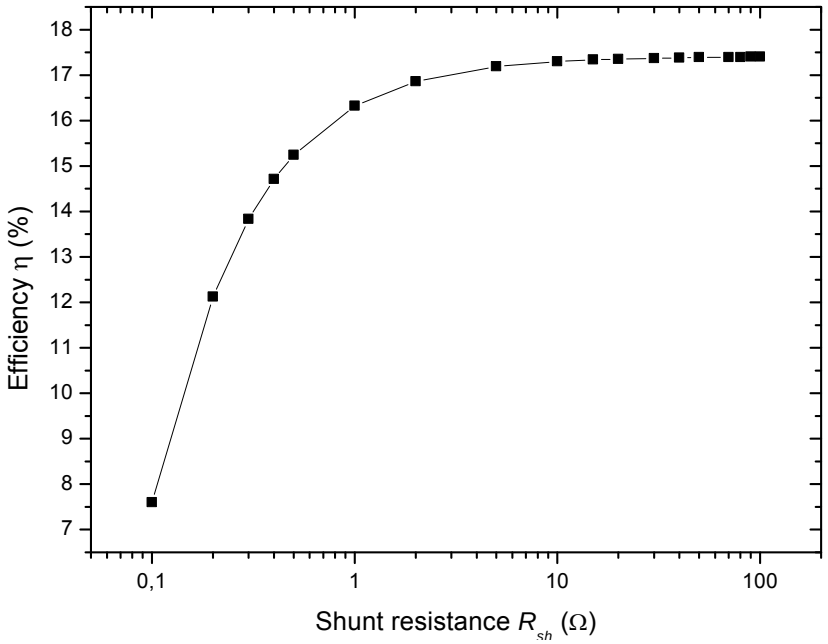

Figure 3.19 Calculated efficiency versus R_{sh}. Shunt resistance must be of the order of 10÷100Ω.

References

[1] Luque A., Hegedus S., *Handbook of photovoltaic science and engineering* , John Wiley & Sons, New York, NY (2003).

[2] Sze S, Physics of Semiconductor Devices, 2nd Edition, John Wiley & Sons, New York, NY (1981).

[3] Pierret R, in Pierret R, Neudeck G (Eds), *Modular Series on Solid State Devices, Volume VI: Advanced Semiconductor Fundamentals*, Addison-Wesley, Reading, MA (1987).

[4] Ciszek, T.F., Wang, T.H., Burrows, R.W., Wu, X., Alleman, J., Tsuo, Y.S., and Bekkedahl, T. *23th IEEE Photovoltaic Specialists Conf. Record*, Louisville (IEEE, New York) (1993).

[5] Ciszek, T.F., Wang, Tihu, Schuyler, T., and Rohatgi, A., *J. Electrochem. Soc.* (1989).

[6] Davis J.R. Jr., Rohatgi A., Hopkins R.H., Blais P.D., Rai-Choudhury P., McCormick J.R., and Mollenkopf H.C., *IEEE Trans. Electron. Devices* (1980).

[7] Green M, *Prog. Photovolt.* (2000).

4. A Real Industrial Process for Low-Cost, High Efficiency Silicon PV Cells

4.1 - INTRODUCTION

This thesis work belongs to an industrial R&D project arisen from a collaboration between Meridionale Impianti (M.I.) S.p.A., UniCt (Catania's University), Advanced Technology Solutions (A.T.S.) S.r.l. and Meridionale Impianti Welding Technology (M.I.W.T) S.r.l.. The project, financed by the Technologic Innovation Fund (F.I.T.) is entitled "*R&D program directed toward the realization of novel high efficiency photovoltaic cells and modules*"". The project purpose was the development of innovative processes and new equipments aimed at production of high efficiency and low-costs first generation silicon photovoltaic cells. It included a pre-competitive development and an industrial research to achieve the issues below listed:

- processes study
- materials study
- contaminants analysis and monitoring
- PV cells electrical parameters characterization
- prototype equipment planning and realization

The entire industrial standard process used for realize a silicon PV cell has been studied to get a picture of current technology in PV production. On the basis of the results obtained by the simulation program explained in chapter 3, a revision of every single manufacturing step has been carried out evaluating costs and benefits, in order to attain a competitive manufacturing line. Materials and equipments have been analyzed to develop repeatable and stable processes. A careful analysis of contaminants and chemical elements has been also performed. Finally, a new accurate data analysis method has been developed to determine cell electrical parameters (I_{sc}, V_{oc}, FF, R_s, R_{sh}) by *I-V* measurements, in order to estimate performance advantages achievable by process flow modification. Therefore, all critical parameters influencing cell efficiency have been studied with the purpose of specifying suitable process innovations.
Data obtained by research and simulation activities have permitted to create a prototype productive line, designed with the principle purposes of product quality, manufacturing cost reduction and energy saving.

4.2 – MANUFACTURING PROCESS FLOW STEPS ANALYSIS

4.2.1 - Grinding

The aim of this step was to recover silicon scrap wafers coming from multinational companies operating in microelectronic sector (e.g. ST Microelectronics, Micron) and to make them raw materials to PV cells production after appropriate cleaning, cutting and checking operations.
Thus, it has been carried out a sampling on thickness reduction of mono-crystalline silicon wafers to support R&D program planned inside the project. Activities have been realized in a dedicated MIWT S.r.l. plant. Mechanical treatment has been achieved utilizing a grinder machine with diamond cup wheel of different granulometry, proceeding through two consecutive steps: a first rough grinding and a successive fine grinding. Figure 4.1 shows the utilized grinder machine: G&N MPS2-RC Vacuum.

Figure 4.1 Grinding machine G&N MPS2-RC Vacuum.

Equipment is a wafer grinder, usable for wafers with diameters of both 6 and 8 inches, equipped with a vertical grinding spindle and three diamond cup wheels. Grinding machine has a rotary table speed variable between 0 and 30 rpm and its accuracy is <5µm Total Thickness Variation (TTV).
Wafers utilized for sampling were p-type <100> mono-crystalline Czochralski silicon, 520µm (6" wafers) or 720µm (8" wafers) thick, with resistivity greater than 1Ohm·cm.
Thicknesses targets of 210µm and 250µm for 6" and 8" wafers respectively have been established so as to eliminate all integrated circuits on wafers surface and to reach the right value to be used for PV technology. Under these thickness values, stress accumulated on wafers highlights a mechanical criticality that represented an elevated breakage risk caused by micro-fractures.
Figure 4.2 reports the measured wafer strength average as function of silicon removed and wafer final thickness. Wafer strength is a measure of the maximum

force necessary to break the wafer and is determined applying an increasingly stressing force until the wafer breaks. The measured mechanical strength reflects the local mechanical properties and depends strongly on the surface condition and on length and number of micro-cracks [1] [2].
Measures shown in figure 4.2 refer to a 6" wafer. Sampling has been collected for an initial thickness of 300µm.

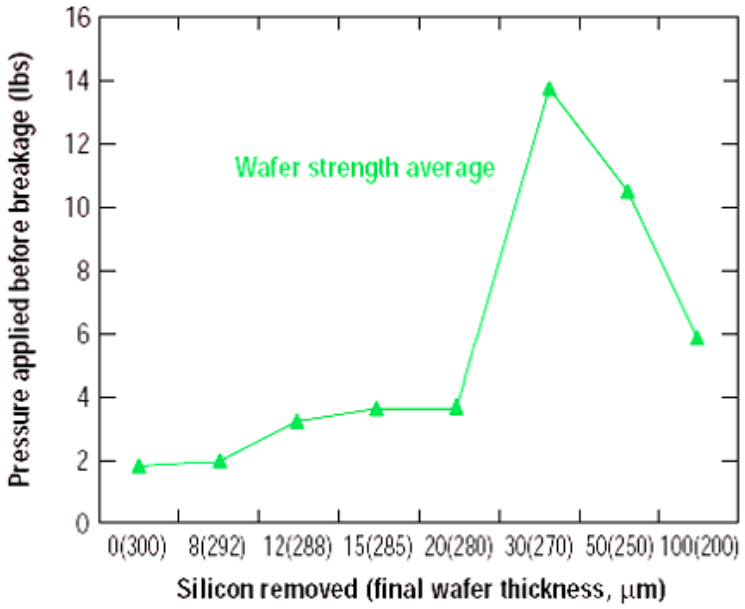

Figure 4.2 Pressure applied before breakage versus Silicon removed and final wafer thickness (6"). Under ~210µm, stress accumulated on wafer highlights a mechanical criticality that represented an elevated breakage risk.

To avoid damages due to friction with the various layers to be removed (metals, oxides, etc.) a high hardness wheel grinding have been used. Soft wheel could result in self damaging after a single grinding cycle and consequently it does not guarantee good successive workings.
To improve the yield of this process step, two additional installations have been realized:

- a filtering configuration
- a drying system.

A micro-filtering set constituted by a steel housing containing a filter has been enclosed to clean the de-ionized water (D.I.W.) necessary for lapping. This filtering procedure is used to keep high roughness particles away from silicon wafers surface during grinding process. These particles could induce micro-cracks causing wafers breaking or irreversible damaging on wafers surface.

Figure 4.3 shows the implemented water filtering system and relative constructive design.

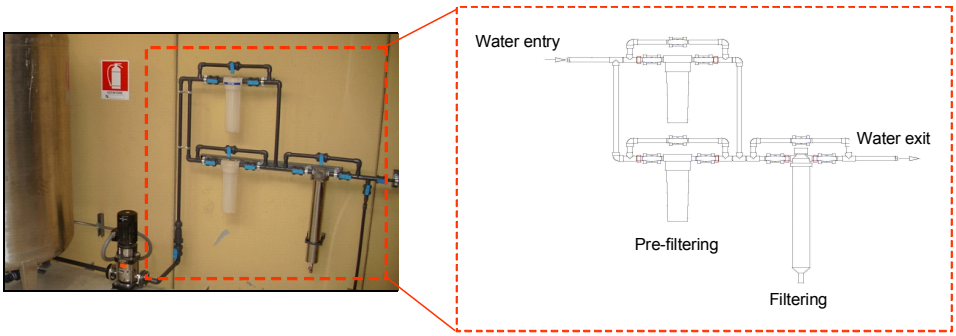

Figure 4.3 Water micro-filtering system and respective plan.

After thickness reduction, wafers have been subjected to a chemical treatment in HF (7%) (to remove silicon oxide residuals produced during mechanical proceedings), and then to a water rinse. HF etch has been performed in an appropriate polypropylene chemical bench equipped with tanks inside which wafers were manually immersed. The acid distribution occurs automatically by means of a dedicated Chemical Distribution System (CDS).
HF is involved in several steps during PV cells production, so the quality of this product (especially concerning metallic contaminants) is critical for the entire process result. Generally, metallic impurities contained in used HF solutions were in concentration lower than 0.05ppm for every metal species.
HF etch and water rinse are followed by a drying process. The drying system is composed of a container inside which wafers are submitted to a filtered airflow: in this way, all residual water particles are removed from wafers surface.

4.2.2 – Texturing

This process step is used to reduce optical losses deriving from reflection of incident solar radiation and to allow the enhancement of photovoltaic effect useful area.
Texturing consists of a surface shaping with microscopic pyramids obtained through a silicon <111> crystallographic planes wet etch. As shown in figure 4.4, this surface structure allows to catch more light inside PV cell because pyramids increase reciprocal reflections and trap reflected light inside substrate.

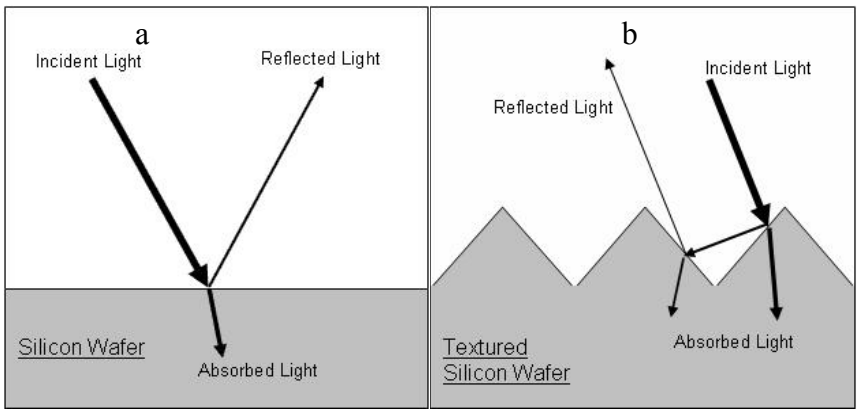

Figure 4.4 Reflection on virgin (a) and on textured (b) wafer surface. Textured structure permits to catch more light inside PV cell than virgin surface because pyramids increase reciprocal reflections and trap reflected light inside substrate.

Textured surface can be created dipping the cell in an appropriate chemical solution. By using right chemical composition, temperature and etch duration, wafers can be reliably and repeatable textured to produce optimal pyramidal formations.
Silicon anisotropic wet etch is characterized by a considerable etch rate variation according to crystallographic planes directions. Consequently this type of etches creates substrate excavations whose form and depth depend on crystallographic planes orientation. In literature discordant data about silicon crystallographic planes etch rate are reported. This is due to the elevated number of parameters that influence the chemical reaction: solution homogeneity, chemicals concentration, silicon defects, etc. One of the most important process parameter is the temperature: increasing temperature, etch rate towards all crystallographic directions increases and surface roughness decreases.
Most common texturing techniques use weak alkaline solutions and are characterized by a low etch rate that cause only few micrometers silicon surface removing. Etching process occurs by means a sequence of oxidations and etching reactions. As illustrate in following formula, water molecules and hydroxyl ions OH^- are involved in Si-H oxidation with H_2 molecules production:

$$Si\text{-}H + H_2O \rightarrow Si\text{-}OH + H_2 \qquad (4.1)$$

Reaction speed depends strongly on OH^- ions concentration.
As result, a pyramid formation created by grains with crystallographic orientation <100> or <111> is obtained. As shown in figure 4.5, hillocks appear as superficial regular pentahedron composed by four <111> lateral crystallographic planes on a <100> base plane.

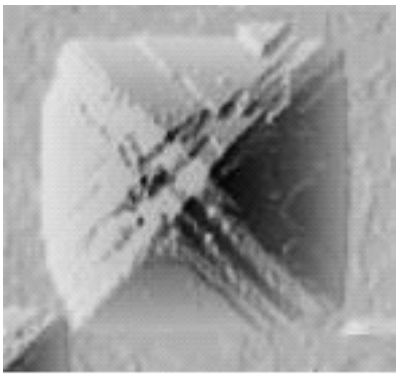

Figure 4.5 Superficial pyramidal formation after Silicon wet etch: four <111> lateral crystallographic planes on a <100> base plane.

At present, most common chemical solutions utilized to texture wafers surface are mixtures of Potassium hydroxide (KOH) or Sodium hydroxide (NaOH) with isopropyl alcohol (IPA). IPA helps to remove Hydrogen bubbles, promoting pyramids formation: Hydrogen bubbles produced in the reaction between NaOH or KOH and silicon adhere to sample and block the further reaction, resulting in a weak texturing. Nevertheless, IPA easily pollutes workbench and is very expensive. In typical texturing conditions, IPA concentration is higher than the KOH/NaOH concentration.
The texturing method based on KOH and IPA chemical solutions, is the process studied and developed inside M.W.I.T. plant for the R&D program. Process has been performed into a chemical bench inside M.I.W.T. plant. Bench frame is realized in steel Fe 360 varnished with epoxy paints; internal and external structures are constituted by polypropylene panels. Bench is provided with seven tanks in which wafers are sequentially immersed during entire process: three for chemical etch, three for rinse and one for drying.
Wafers movement occurs by means of an automatic mechanical arm, activated through a control system which operates also on intake and recycling fluids pumps. Chemical distribution occurs automatically via an appropriate system (C.D.S.).
Used chemical bench is reported in figure 4.6.

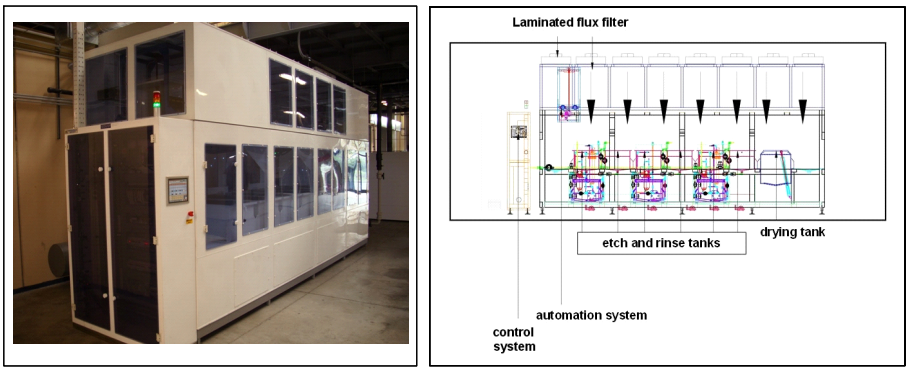

Figure 4.6 Texturing chemical bench and respective plan.

Sparber et al. [3] presented an extensive research about texturing performed by KOH/IPA aqueous solutions. Parameters such as reflection coefficients, surface homogeneity, pyramids size and speed of texturing process are compared. Best results were obtained by using KOH low concentrations (1wt%) and high IPA concentrations (6÷8vol%) at temperatures between 80°C and 85°C; the surface is completely covered with pyramids with base lengths up to 10 µm. The weighted reflection for this surface is 12.5%. SEM analysis and reflectance versus incident wavelength are reported in figure 4.7.

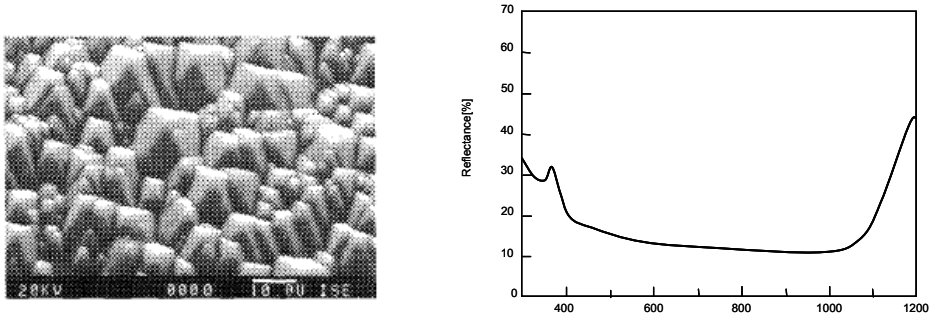

Figure 4.7 Texturing condition: KOH 1wt%, IPA 7vol%, *T*=80 °C, Time= 40min, Etch Rate=0.2 µm/min. [3]

Taking into account these literature data and with the purpose of obtaining a less expensive process, different tests have been performed varying KOH concentration from 1wt% to 5wt%, alcohol concentration from 3vol% to 9vol% and temperature within 70 and 90°C.
First attempts of silicon texturing making use of KOH and methyl alcohol failed: SEM analysis proved that pyramids have not been shaped on wafers surface. Successive tries performed using more concentrated KOH solutions at a temperature of 80°C for 180 minutes produced a poor surface texturing. Results are shown in figure 4.8.

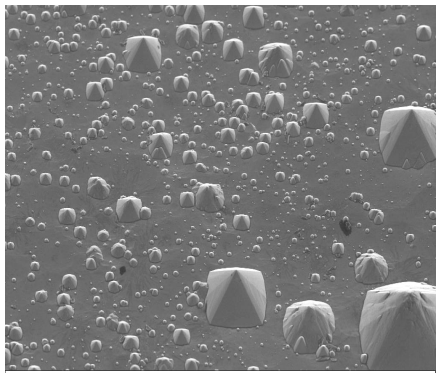

Figure 4.8 SEM analysis of a textured surface after KOH + methyl alcohol etching.

The complete surface texturing has been obtained treating wafers in solutions of KOH (1wt%), water and IPA (7÷9vol%) at 80÷90°C for 40 minutes. Process results are shown in figure 4.9, where are reported SEM analysis (a) and surface reflectance (b) referred to a silicon wafer totally textured.

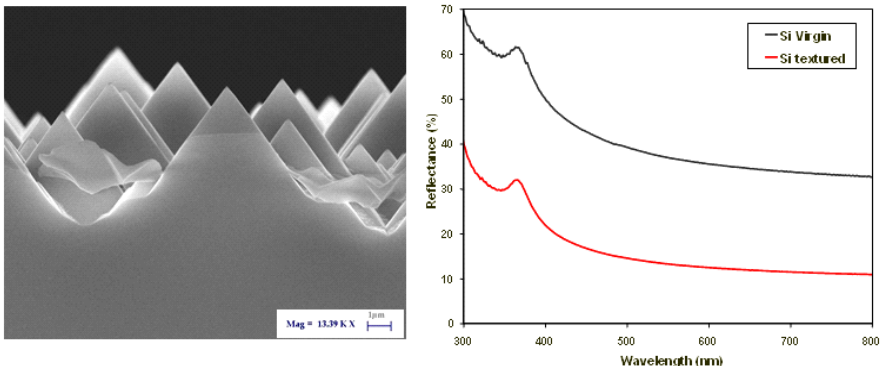

Figure 4.9 a) SEM analysis on Silicon wafer after texturing. b) Silicon surface reflectance. Textured surface reflects about 40% less than virgin Silicon.

Time process depends on wafer quality: for a wafer "as-cut", texturing is complete after about 30 minutes, while for a wafer without defects, surface is completely covered by pyramids after at least 40 minutes. This result is highlighted in the figure 4.10 which shows for both cases weighted reflectance as a function of time etch.

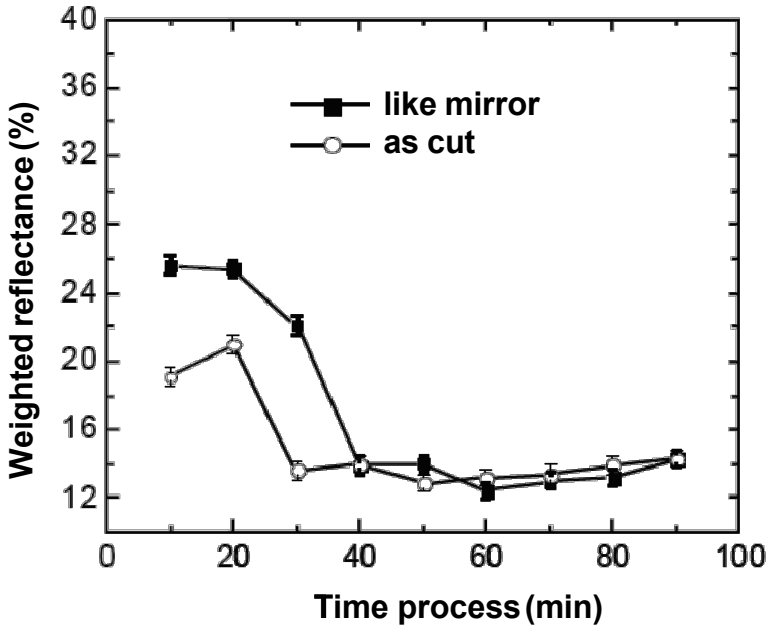

Figure 4.10 Weighted reflectance surface versus time process. Texturing is complete after about 30min. for a wafer "as-cut" and after at least 40min. for a wafer "like mirror".

After etching step, texturing process continues with a rinse in HCl (to remove residual organic substances) and with a successive etch in HF (to remove sodium metallic ions or silica).
The main drawback of industrial random pyramid texturing is results reproducibility. During process, temperature is close to IPA boiling point (82°C), consequently IPA evaporates and solution composition changes. Unfortunately evaporation control and chemical recharge are not always optimal.
In order to face this issue and get better results from texturing process step, some implementations have been developed:

- an automatic mixing system (KOH+IPA+D.I.W.)
- an automatic IPA distribution system including a distribution piping.

The Chemical Distribution Module for IPA and CDM mixer for KOH, IPA and D.I.W. are shown in Figure 4.11 and 4.12 respectively.

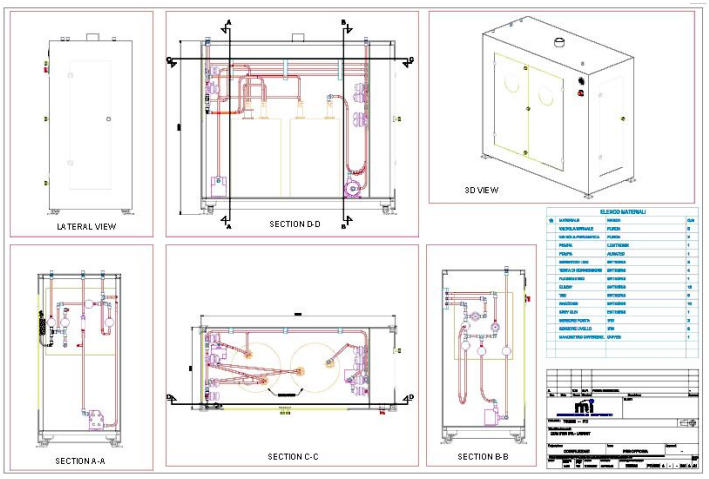

Figure 4.11 IPA CDM executive plans.

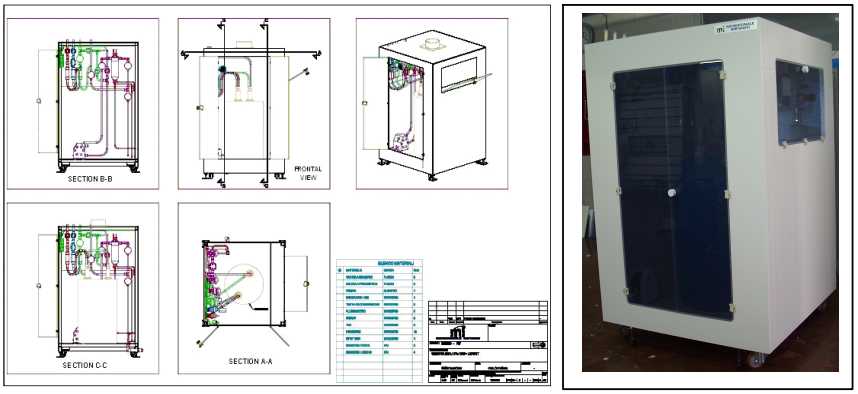

Figure 4.12 CDM mixer (KOH+IPA+D.I.W.) and respective plan.

In literature [4], studies where KOH/IPA solution is substituted by K_2CO_3 are reported, and an average reflectance of 12% is shown as result of processes characterized by a K_2CO_3 concentration of 30wt%, a temperature of 100°C and a process time of 30 minutes. Even if the result obtained by this alternative solution is comparable to the result obtained by means of KOH/IPA solution, K_2CO_3 solution based method is more expensive than KOH/IPA method because both temperature process and solution concentration are higher.

4.2.3 – Emitter diffusion

As illustrated in chapter 3, emitter formation process influences significantly PV cell electrical performance because emitter thickness and doping level are critical parameters for device efficiency. On the basis of the results obtained by simulations, it has been estimated that a junction available depth must be maintained as thin as possible both to promote light absorption and demote

charges recombination. Junction depth has evaluated by sheet resistance measurements performed using a four points probe.
Different technologies could be used to create the emitter layer. However, doping mechanism is always based on a diffusive process which occurs introducing controlled quantity of *n*-type (Phosphorous) or *p*-type (Boron) impurities. Most common methods utilize gaseous sources or doping pastes deposited by means of screen printing technique.
Using gas, doping impurities are introduced through a diffusion process constituted by two different steps: a pre-deposition and a drive-in diffusion. Pre-deposition is infinite-source diffusion and requires a constant surface concentration of diffusing atoms. Drive-in diffusion is, instead, limited-source diffusion and requires a constant amount of total doping per unit area of the diffusing surface. In our case, n^+-*p* junctions have been realized introducing *n*-type dopants inside *p*-type epitaxyal layers, utilizing Phosphorus oxychloride ($POCl_3$) diffusion by means of a high temperature furnace.
This procedure allows:

- an accurate depth junction control
- a good adaptability to industrial production (process can be performed simultaneously on a large number of wafers).

To perform dopant diffusion is required to put wafers inside an appropriate furnace. Before this operation, preliminary cleaning processes are necessary to eliminate organic and metallic impurities or dust particles from wafers. Cleaning step is followed by a rinse in D.I.W. with resistivity grater or equal than 10 MΩ·cm. Wafers are subsequently dried into a spin-dryer by means of a hot nitrogen flow.
After cleaning, rinse and drying steps, diffusion can be performed inside the furnace designed to provide a controlled gas flow to wafers into a high temperature environment. The furnace consists schematically of a heating element (a muffle containing a spiral-shaped rolled up resistance plunged into thermal insulator material), a diffusion tube, a diffusion boat, and a dopant delivery system. A typical horizontal diffusion furnace is represented in figure 4.13.

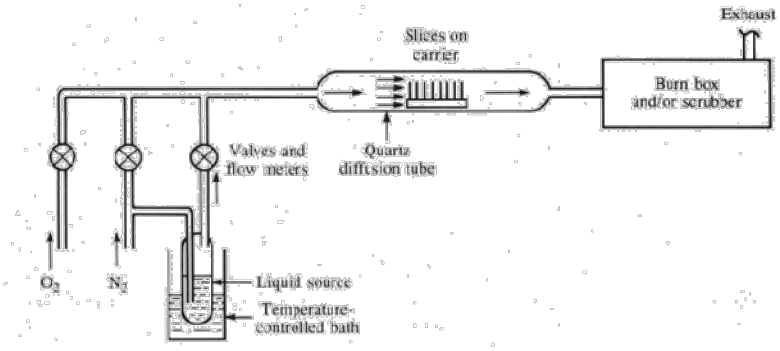

Figure 4.13 Illustration of a typical horizontal diffusion furnace.

Furnace could work at temperatures between 400°C and 1300°C. Quartz tube length is determined by necessity of introduce at the same time many wafers (up to 250) that must be loaded on quartz boats, one after other. To obtain a good doping uniformity is indispensable that temperature does not vary more than 0.5°C along the entire zone containing wafers.
Typical diffusion process can be summarized with these following actions:

- wafers introduction inside furnace
- thermal recovery and pre-oxidation
- dopant introduction
- dopant purge
- boat extraction.

Gas quantity sent to furnace is controlled using flowmeters which allow to obtain the automatic dopants flow regulation and to make doping system independent from external conditions.
$POCl_3$ is the most common chemical compound used to create *n*-type emitter via high temperature $POCl_3$ diffusion. During the entire process a continue Nitrogen flow used as gas carrier is applied. Reached the right temperature for the diffusion (800÷960°C) an additional N_2 flow with the $POCl_3$ source is introduced. Dopant introduction can continue for about thirty minutes or more. At the same time, a low quantity of O_2 is added inside quartz tube. A chemical reaction occurs and involving $POCl_3$ and O_2 produces P_2O_5 a Cl_2 on wafer surface. P_2O_5 and O_2 react with silicon forming a phosphorous-doped SiO_2, named PSG (Phosphorous Silicate Glass), on wafer surface. Reaction that occurs in gaseous phase is below expressed:

$$4\,POCl_3 + 3O_2 \rightarrow 2P_2O_5 + 6Cl_2 \tag{4.2}$$

From Phosphorous pentoxide P_2O_5 takes place silicon transfer accordingly surface reaction:

$$2\,P_2O_5 + O_2 + 6Si \rightarrow 6SiO_2{:}P \tag{4.3}$$

During doping process, uniformity is controlled by means of temperature and gas flow monitoring. Process results depend strongly on dopant quantity, gas carrier flow and gas pressure; varying one or more of these parameters, it is altered doping uniformity.
After Phosphorous diffusion, PSG is removed using a diluted HF acid solution (10%).
A purging phase follows the doping step: a Nitrogen flow is pumped for few minutes inside quartz tube to eliminate toxic gasses residuals and to extract wafers in safety conditions.

For our purpose we utilized <100> p-type mono-crystalline silicon wafers with resistivity of 1.5÷3Ω·cm, primary reduced at thickness of 210µm and subsequently textured.
Trials have been executed inside M.I.W.T plant using furnace illustrated in figure 4.14.

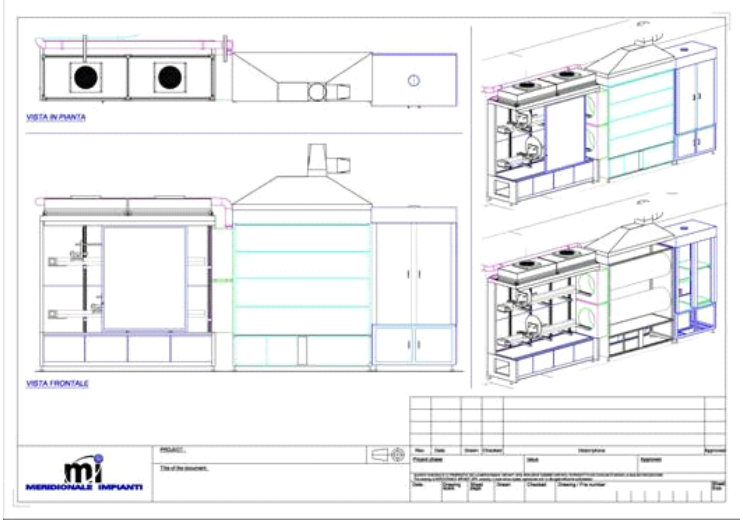

Figure 4.14 Diffusion furnace executive plan.

Performing $POCl_3$ diffusion at various temperatures for 40 minutes, following reported results have been obtained. Figure 4.15 shows the sheet resistance versus temperature diffusion.

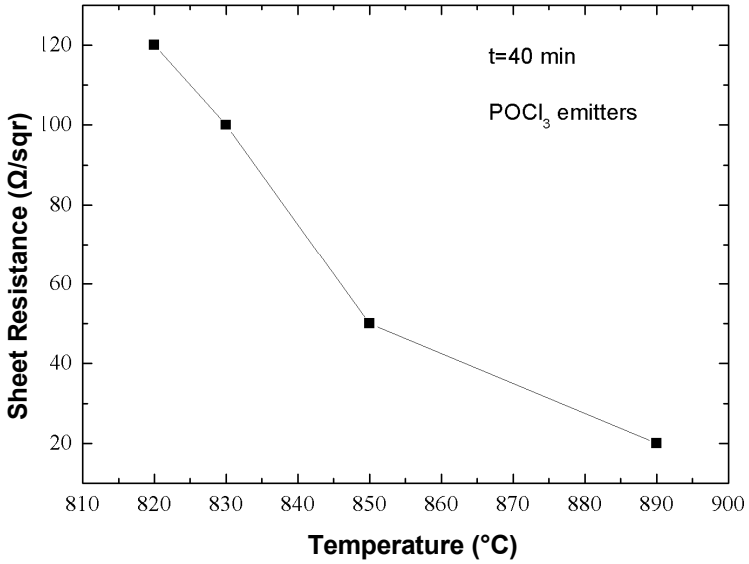

Figure 4.15 Sheet resistance as a function of diffusion temperature. Lowest resistances have been obtained increasing temperature over 850°C.

In figure 4.16 the doping concentration profile obtained with a $POCl_3$ diffusion process carried out with a temperature of 850°C for 40 minutes is reported. Emitter depth is about 0.45µm.

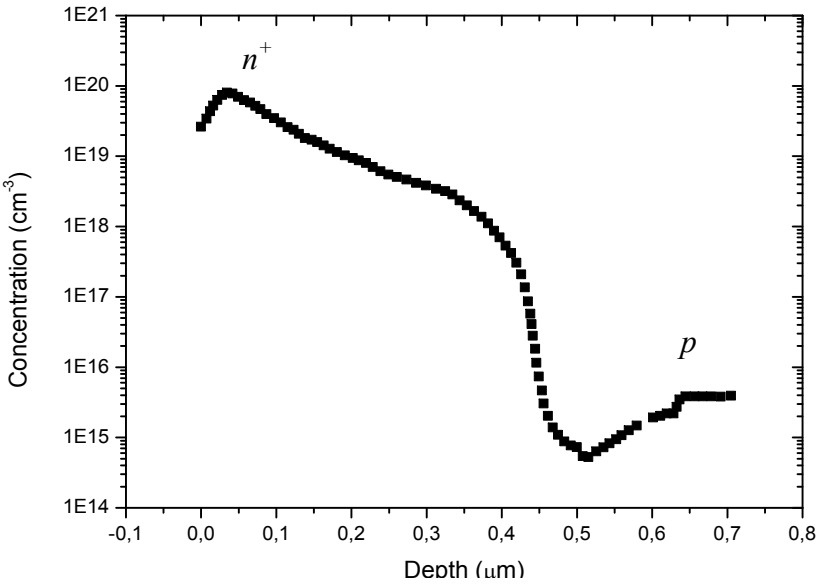

Figure 4.16 Sheet resistance profile obtained by means of $POCl_3$ diffusion at 850°C for 40 minutes. Junction depth is about 450nm.

On the used equipment some modifications have been effected to permit an accurate dopant diffusion depth control by means of thermodynamic parameter checking. Implemented installations are briefly described following:

- a new "jungle" to obtain an automatic management of diffusion process
- a cooling system to control chamber temperature
- an automatic check structure to manage thermodynamic parameters variations
- a tool to distribute and decompress gasses (N_2, O_2, $POCl_3$)
- a kit to clean, dry and stock furnace quartz tubes
- a furnace emissions scrubber (shown in figure 4.17)
- a gas detection implant.

Figure 4.17 Emission scrubber.

With the purpose of investigate a possible process improvement direct towards manufacturing cost reduction with no impact on product quality, emitter formation method based on doping pastes has been also studied. In fact, a high quality n^+ layer could be obtained utilizing diffusion of screen-printed doping pastes inside an infrared belt furnace. This method, consisting of a single step process (without a pre-deposition step) allows creating of uniform emitters restraining process costs.

A screen printable thick film paste is composed by finely divided particles of electrically functional solids dispersed in an organic medium, including a plurality of solid organic polymers dissolved in volatile organic solvent. To obtain emitter formation, Phosphorus pastes manufactured by FERRO (DP99-038) with different dopant concentration have been used [5].

The paste was applied on silicon wafers through a 180 mesh screen with an emulsion layer 25µm thick dried at 300°C for 5 minutes. Phosphorous coat was about 8µm thick. Wafers were after submitted to a high temperature firing process (T=825°÷950°C) to diffuse Phosphorous inside silicon and form an n^+ layer about 0.4µm thick. Pastes residuals were then removed using an HF etch [6].

Figure 4.18 shows emitter sheet resistance obtained by screen printing method, for a diffusion time of 4 minutes varying temperature from 825°C to 950°C. Experimental data demonstrate that inside this temperature range is possible to achieve resistivities between 30Ω/sqr and 200Ω/sqr.

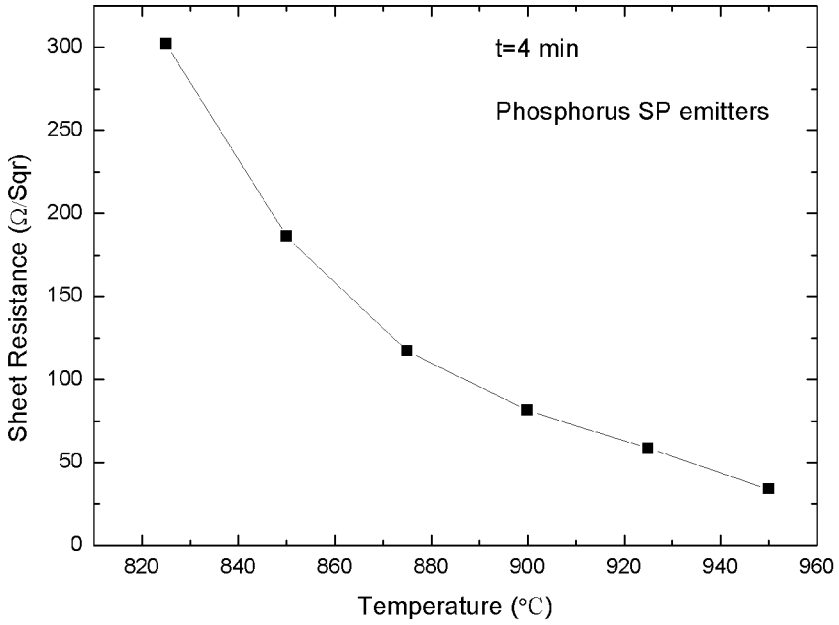

Figure 4.18 Sheet resistance versus temperature diffusion (Screen Printed emitters).

Figure 4.19 shows the measured Phosphorus surface concentration as a function of depth. The samples have been diffused at 900°C for 2 minutes and refer to various doping paste concentrations.
Regions with higher phosphorous concentration had emitter depth of 0.4µm and surface concentration greater than $10^{20}cm^{-3}$. Regions with lower phosphorous concentration show shallower emitter depth of 0.15µm and surface concentration of $10^{19}cm^{-3}$. This allows to control selective emitter diffusion by changing the phosphorous concentration and keeping the temperature constant.

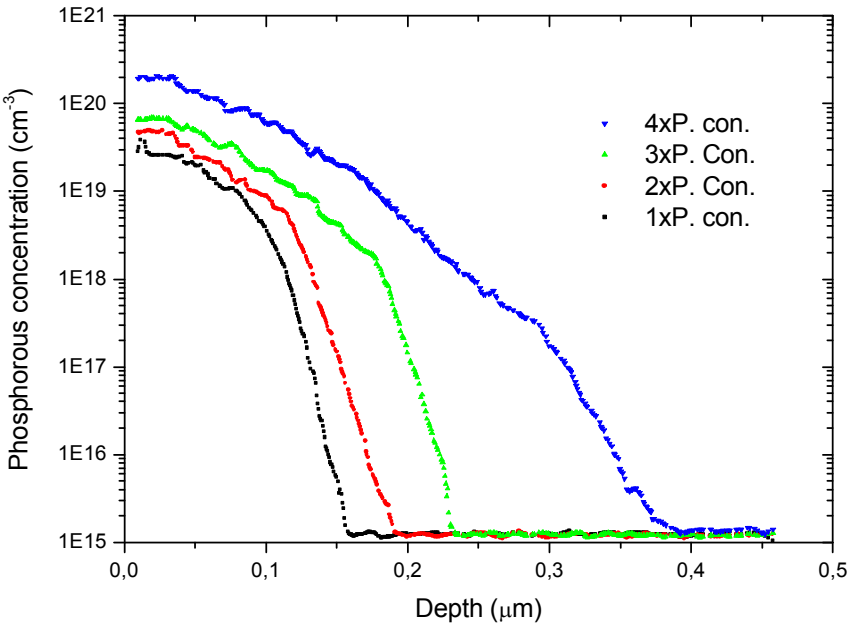

Figure 4.19 Phosphorous concentration as a function of depth. Regions with higher phosphorous concentration had emitter depth of 0.4μm and surface concentration greater than $10^{20}cm^{-3.}$ Regions with lower phosphorous concentration show shallower emitter depth of 0.15μm and surface concentration of $10^{19}cm^{-3}$.

As demonstrated, phosphorous doping pastes can be used as valid alternative to conventional $POCl_3$ diffusion method. Selective emitter can easily be formed using simple screen-printing technology and diffusion using a belt furnace.
Emitter formation by doping pastes could permit to renew standard process flow diagram, cutting involved equipments and allowing a considerable manufacturing cost reduction. In fact, high costs due to double diffusion step are reduced through a single thermal step.

4.2.4 – Anti-reflection coating

An anti-reflection coating (ARC) must be realized on frontal wafer surface to minimize losses due to light reflection and to passivate cell surface, allowing the reduction of current leakages caused by superficial recombination.
Anti-reflective layers studied to develop the PV cell manufacturing line are:

- silicon oxide (SiO_2)
- silicon nitride (SiN_x)
- zinc oxide (ZnO).

Silicon oxide is an excellent crystalline silicon surface passivating, largely studied and used in microelectronic sector. In PV wafer-based cell production, SiO_2 standard making method is very simple, based on a high temperature

thermal process immediately sequential at emitter formation. However, SiO_2 is an effective passivating material only for mono-crystalline wafers. In fact, in microcrystalline silicon, SiO_2 coating is unsuccessful because grain edges necessitate hydrogen presence to passivate superficial layer and to avoid electrical charges recombination.
In mono-crystalline cells, combining silicon surface texturing with an oxidation layer (refraction index 1.9) tens of nanometers thick, standard front antireflective and passivating proprieties are satisfied.
Like in $POCl_3$ diffusion, oxidation takes place inside a quartz tube maintained at high temperatures (within 600°÷1000°C) and occurs with a growing speed contained inside the range 5nm/hr÷1µm/hr. Thermal oxidation could be executed in dry or wet environment, according to following reactions:

$$Si + O_2 \rightarrow SiO_2 \text{ (dry oxidation)} \quad (4.4)$$

$$Si + H_2O \rightarrow SiO_2 + 2H_2 \text{ (wet oxidation)} \quad (4.5)$$

Dry oxidation is very slow and it is suitable for high quality thin film oxide production (10÷100nm). In wet oxidation, water vapor introduced inside the process furnace is employed. Since water molecules diffusion towards oxide is higher than oxygen diffusion, for the same temperature process growing speed could increase even till 150nm/hr.
SiO_2 cell passivation layer produced by Meridionale Impianti on textured wafers has been manufactured effecting dry method, with a process temperature of 650°C and a process time of 100 minutes: as result an oxide film 50nm thick (verified by XPS) has been obtained. Figure 4.20 shows a SEM image of the textured and then oxidized silicon wafer surface.

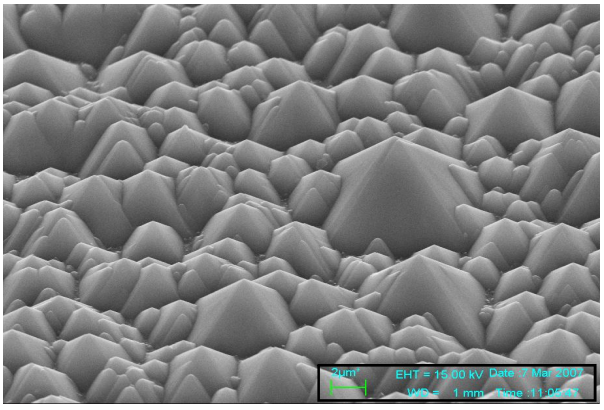

Figure 4.20 Oxidized textured Silicon wafer surface SEM image.

Compared to silicon oxide, silicon nitride presents better passivant proprieties. It is widely used in mono or poly-crystalline PV cells production because Hydrogen contained inside nitride layer saturates silicon bonds and enlarges

charges recombination time. Nitride is indispensable in the case of microcrystalline cells to get the electrical stabilization of grain edges. This kind of passivation is typically applied using plasma-enhanced chemical vapour deposition (PECVD) to attain a several hundred nanometres thick layer. Figure 4.21 schematizes a PECVD process tool.

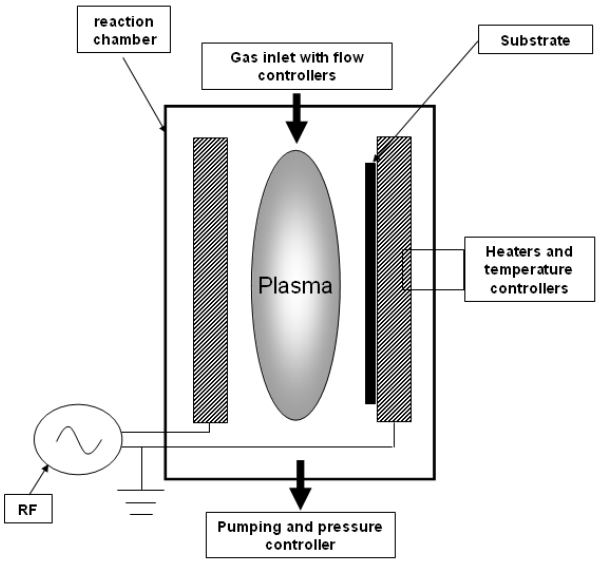

Figure 4.21 PECVD process tool schematization.

Silicon nitride PECVD process involves Silane (SiH_4) and ammonia (NH_3). These two gasses give rise to the following reaction:

$$SiH_4 + NH_3 = SiN_x : H \tag{4.6}$$

Hydrogenated amorphous nitride has optical proprieties that can be determined by the ratio between reaction gasses concentrations, in accordance with the parameter *R*:

$$R = \frac{SiH_4}{SiH_4 + NH_3} \tag{4.7}$$

R can be varied between 0.5 and 0.1.
Refraction index $n(\lambda)$ obtained for various nitride films created with different *R*, is plotted versus the wavelength λ in figure 4.22. In the same figure, the refraction index versus *R* for λ=633nm is also illustrated.

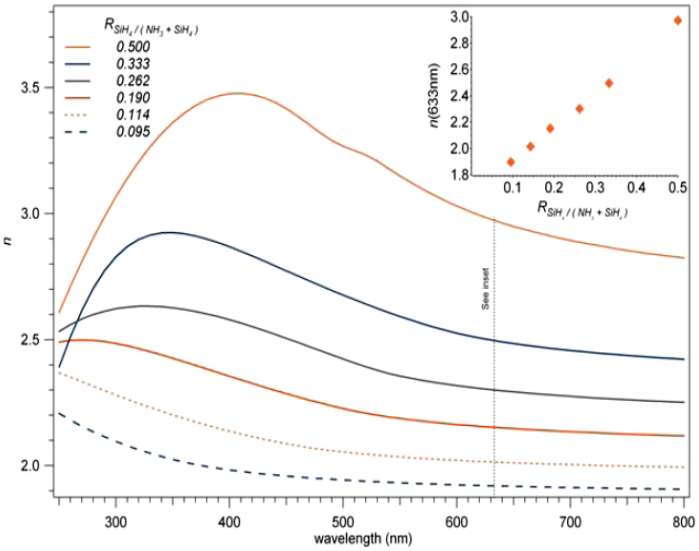

Figure 4.22 Refraction index *n* as a function of wavelength for various $R=SiH_4/(SiH_4+NH_3)$. Inside the insert, the refraction index versus *R* for a λ=633nm is illustrated.

From these data, it was possible to determine optimal nitride thickness value, maximizing transmitted light intensity in agreement with a model that includes nitride optical parameters. Results of this model are put in evidence in figure 4.23: best nitride thickness value is 85nm with a refraction index of 1.9 and characterized by an average transmittance of 91%.

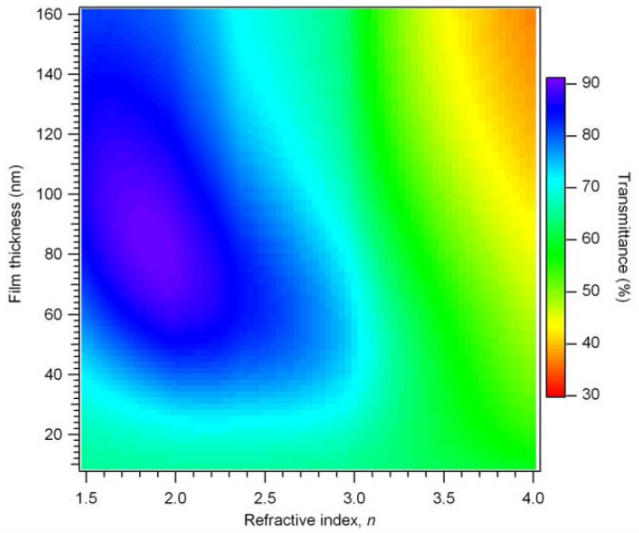

Figure 4.23 SiN film thickness and Transmittance versus refraction index *n*. Best nitride thickness value is 85nm with a refraction index of 1.9 and an average transmittance of 91%.

To obtain this thickness value, an RF of 14.36MHz and an RF power of 400W, a temperature of 350°C, a SiH_4 flow of 50 sccm and an *R* ratio between 0.1 and 0.15 have been set up.
Figure 4.24 shows the reflectance of a textured and then nitride passivated silicon wafer in comparison with bare silicon reflectance, versus incident wavelength.

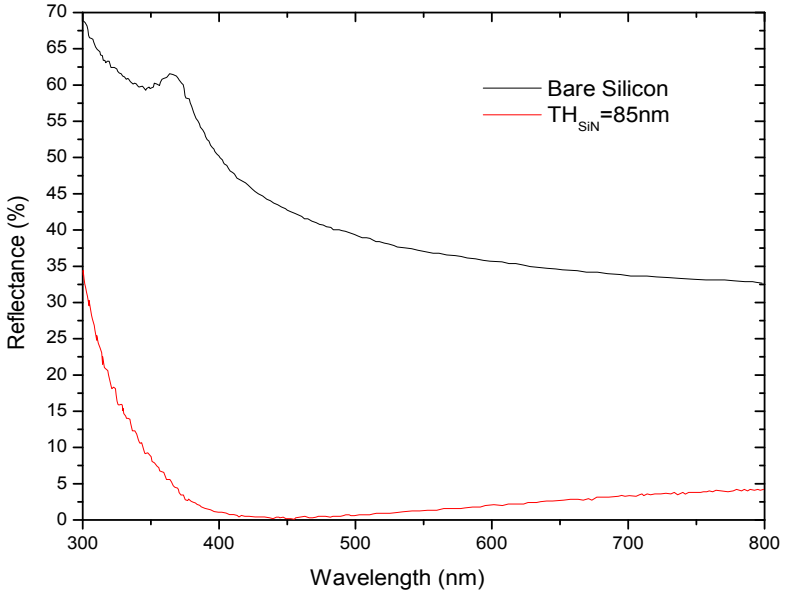

Figure 4.24 Wafer surface reflectance for bare Silicon and for SiN passivated wafer as a function of incident wavelength.

ARC and frontal contact making process are deeply connected. In the case of an insulating ARC, emitter contact requires a high temperature process to allow Ag penetration across the passivation layer. In the case of a transparent conductive oxide (TCO), instead, frontal contact is deposited on cell front by way of a low temperature screen printing process.
Since the use of ZnO as ARC is strongly related to its use as electrical frontal contact and given that the ZnO deposition method utilized represents an original alternative to standard process flow, this case will be extensively discussed inside the next paragraph 4.4.

4.2.5 – Edge isolation

$POCl_3$ diffusion that leads emitter formation obviously occurs also over cell edges, making therefore necessary a following etching process directed toward edges insulation. This step is executed through a dry etch, after the ARC process.
Dry etch is a removal process that does not utilize any liquid chemicals to eliminate materials from wafer, generating only volatile product. It may be

achieved by chemical reactions that consume the material (using chemically reactive gases or plasma) either by material physical removal (by momentum transfer) or by a combination of both physical removal and chemical reactions (Reactive Ion Etching).
To perform edge isolation, has been used the last method, which employs chemically reactive low-pressure plasma. Reactive Ion Etching tool consists of a vacuum chamber, with a wafer plate situated in the bottom and electrically isolated from the rest of the chamber. Gas enters through small inlets in the top of the chamber and exits to the vacuum pump system through the bottom. Plasma is produced applying a strong RF (radiofrequency) electromagnetic field to the wafer plate. The oscillating electric field ionizes the gas molecules by stripping electrons. Plasma is primed by free electrons released from the negative electrode and direct toward positive electrode. During their path, free electrons acquire kinetic energy by means of electric field and collide with gas molecules causing their ionization. Some electrons stripped form molecules could themselves get sufficient energy to induce others ionization collisions, giving rise to a cascade process.
In each RF cycle of the field, electrons are electrically accelerated up and down in the chamber, sometimes hitting both the upper wall of the chamber and the wafer holder. At the same time, the much more massive ions move relatively little in response to the RF electric field. When electrons are absorbed into the chamber walls, they are simply fed out to ground and do not alter the electronic state of the system. Electrons absorbed into the wafer holder cause charge accumulation due to DC isolation: this charge develops a large negative voltage on the plate (typically around a few hundred volts). The plasma itself develops a slightly positive charge due to the higher concentration of positive ions compared to free electrons [7].
Because of the large voltage difference, positive ions tend to drift toward the wafer platter, where they collide with the sample to be etched. Ions react chemically with the materials on the surface of the samples, but can also sputter some material by transferring their kinetic energy.
Figure 4.25 shows an illustration of a RIE chamber setup.

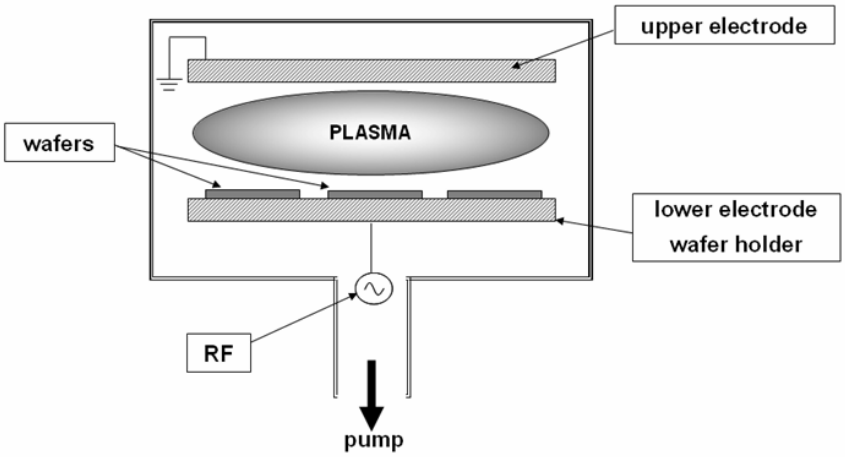

Figure 4.25 Parallel-plate reactive ion etching system.

Dry etch proceeds through consecutive phases and consists of the following basic steps:

- generation of reactive species in a plasma
- diffusion of these species to the surface of the material being etched
- adsorption of these species on the surface
- occurrence of chemical reactions between the species and the material being etched, forming volatile by-products
- desorption of the by-products from the surface
- diffusion of the desorbed by-products into the bulk of the gas.

Dry etch selectivity (that refers to the ability of the reactive species to etch only the material intended for removal leaving other materials intact) is low compared to wet etch because of physical sputter. However, selectivity could be increased choosing correct chemical components.
Process has been performed by means of equipment shown in figure 4.26, using different primer/carrier gasses.

Figure 4.26 Used reactive ion etching equipment.

Equipment was upgraded in order to get better process results: to facilitate process control and to improve process yield a gas (CF_4) distribution tool and a higher vacuum system production (based on an EDWARDS turbo-molecular pump) have been realized. Moreover, an exhaust gasses scrubber has been implemented with the aim of raising personnel and environmental safety.
Through many trials, experimental parameters have been optimized in function of silicon, SiO_2 and SiN etch rate in order to get a selectivity close to one (similar etch rates for all materials) and obtain uniform edges. Etches have been executed in plasma containing CF_4 (Freon R14) and Oxygen. CF_4 is a liquefied gas that etches selectively many metals and respective silicides and oxides. Concerning gas purity, it must used R14 electronic N45 (99.995%)
Etch rate depends strongly on Oxygen quantity, RF power and chamber pressure. Choosing following settings:

- Plasma composition: CF_4 (96%) and O_2 (4%)
- Frequency = 14.56 MHz
- Power = 400W
- Chamber pressure = 100mTorr
- CF_4 flow = 40 sccm
- O_2 flow = 1.6 sccm

an etch rate of 0.1μm/min has been reached. For a process time of 20 minutes this etch rate allows removal of a thickness of 2μm and the insulation of cell emitter from back contact.

4.2.6 – Front and back side contacts

Front contact is used as collector of the photo-generated charges and it plays a primary role in solar cell efficiency because it determines both the series resistance R_s and the frontal shaded area of the device. As previously mentioned, front metallization process depends strongly on anti-reflective type.
A second metallic contact covers entire wafer backside, since it is not exposed to light source. For wafer thickness greater than 200μm, back contact process is simple and based on double printing of Al and Ag pastes to minimize cell series resistance. For smaller thickness, back contact process requires advanced solutions to reduce electrical losses due to charges recombination and incident radiation reflection [8] [9].
Front and backside metallization have been realized by screen printing method, pushing a conductive metal paste across an appropriate mask (mesh screen) to reach the required grid shape. Screen printing principles are illustrated in figure 4.27.

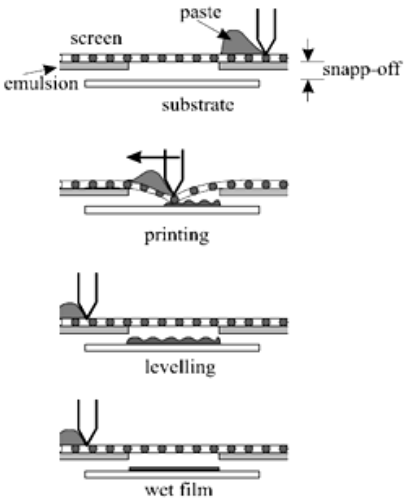

Figure 4.27 Contact screen printing procedure.

A pattern is defined on the mesh screen through a photosensitive emulsion layer exposed in function of the geometry to be realized. Paste is pressed on mesh screen using a squeegee rubber made of a high quality polyurethane elastomer. Squeegee is schematically represented on figure 4.28.

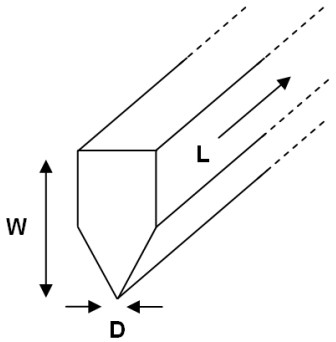

Figure 4.28 Squeegee rubber illustration.

Standard size for the three characteristic dimensions *L*, *W* and *D* of commercial squeegees are 1000mm, 25mm, 5mm or 1000mm, 40mm, 5mm respectively.
Used equipment could be simply subdivided in following elements:

- a loader
- a collecting arm
- a printing structure
- a paste proportioning device
- a furnace
- a cooling system
- a control tool

Firstly, silicon wafers are positioned into the loader. Then a mechanical arm collects wafers from the loader and put them on a trolley through which wafers are moved forward to a conveyor belt. An automatic system produces paste heating and distribution on every wafer, by means of a proportioning device. Subsequent to paste leveling, wafers are conducted inside a furnace equipped with infrared lamps to permit paste fixing onto wafers surface. Drying furnace is divided into three zones with increasing temperature: first zone temperature reaches up to 175°C, second zone temperature up to 185°C and third zone temperature up to 900°C. Wet film is initially dried at 100÷300°C. In this phase, film consists of little grains (1-2µm) conglomerate. Through a successive high temperature firing step (from 500°C to 850°C), deposited layer becomes compact and constituted of large grains (upper 10µm) optically and electronically connected. After heating inside furnace, wafers pass in the last part of equipment where an air cooling system brings them at room temperature. Equipment is entirely managed by a control tool that allows the accomplishment of diagnostic tests and the monitoring of process parameters (pressure and temperature).
Used screen printing equipment is shown in figure 4.29.

Figure 4.29 Screen printing equipment.

Meridionale Impianti S.p.A. in collaboration with ST Microelectronics has realized the design of front and back contact masks for both 6" and 8" wafers. Design has been transferred on a mesh with a grid structure of 75µm and a screen opened area of 48%. Emulsion deposited onto mesh has been treated with photolithographic technique to obtain the appropriate pattern through which metallic paste is spread on wafer surface. Used emulsion was the MS-200 photo-polymer film, version DIN-A4 297x210mm/sheet. In figure 4.30 are shown front (a) and back (b) contact masks designs.

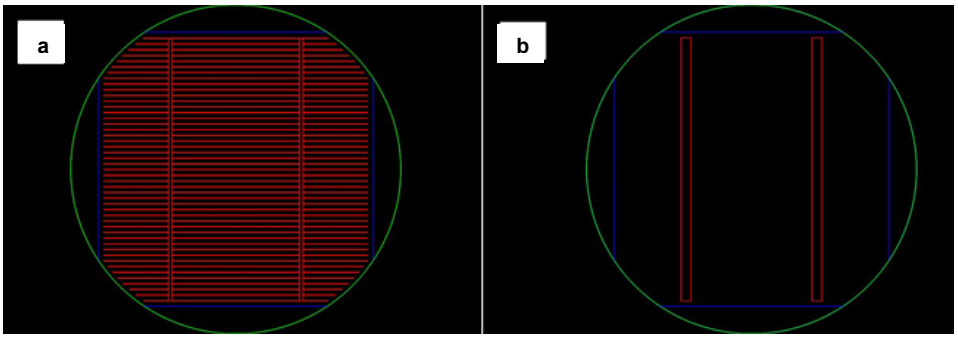

Figure 4.30 Front and back contact masks design.

Figure 4.31 illustrates the external frame that holds up a flexible polystyrene layer that fixes the stainless steel mesh structured with a wire grid.

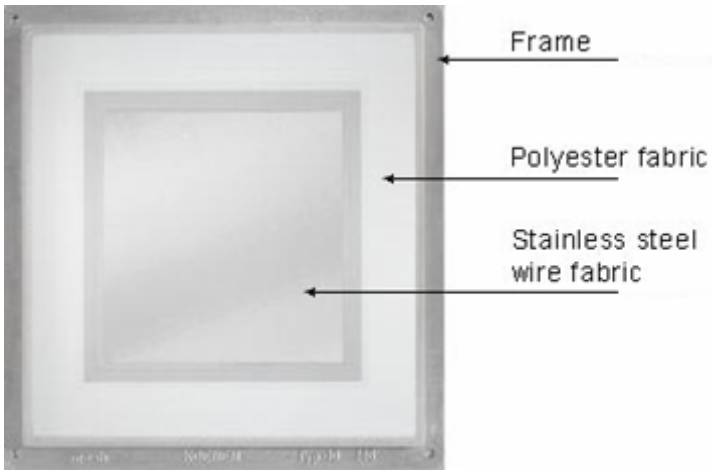

Figure 4.31 Contact mask frame.

The most important screen-printing variables to be set up to obtain a good process are paste viscosity, mesh count (holes per centimeter), mesh wire diameter, snap-off (distance between mask and substrate), squeegee speed and pressure and, above all, firing temperature.
Figure 4.32 reports firing temperature profiles used to attain ohmnic contacts formation at silicon /Ag interface, and corresponding light lamps intensity.

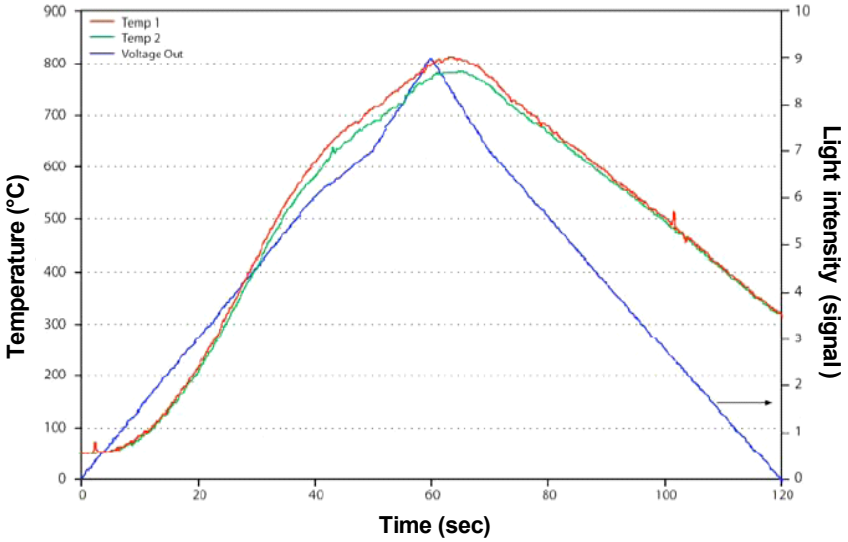

Figure 4.32 Firing process temperature and signal profile.

The entire process lasts about 160 seconds and temperature peak is 810°C.
Figure 4.33 shows the result obtained using ST scrap wafers (8") via screen printing process utilizing Ag paste 3347.

Figure 4.33 Front contact realized by screen-printing process.

As reported in figures 4.34 and 4.35, optical microscope and SEM analyses highlight a bus bar thickness of ~26µm and a width of ~1.5mm. For finger contacts a thickness of ~14µm and a width of ~118µm have been measured.

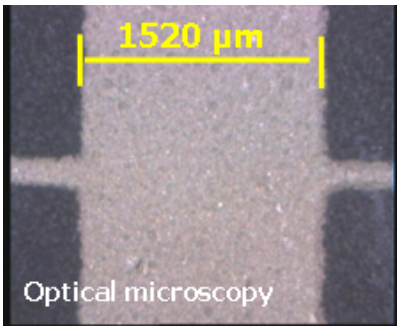

Figure 4.34 Front bus bar contact optical microscope image. Bus width is 1520 µm.

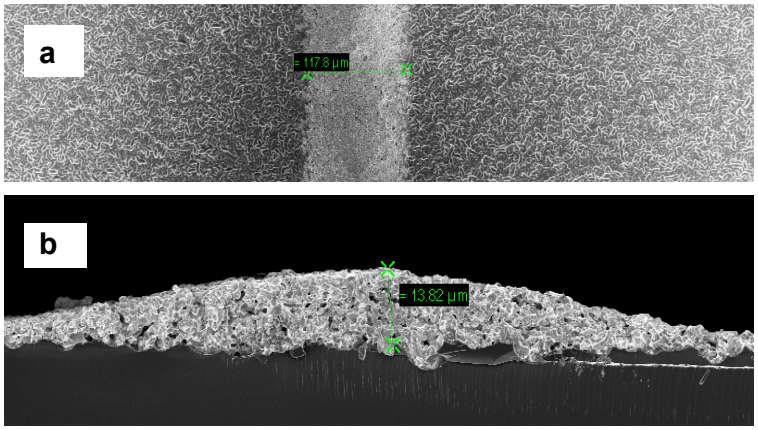

Figure 4.35 Front finger contact SEM analysis. a) Tilted SEM image. b) Cross section SEM image. Finger width is 117.8µm; finger maximum thickness is 13.82µm.

Sheet resistance measurement executed on front contact gave a result of 0.04Ω/sq.
Back contact has been realized via screen-printing process using Al/Pb paste for entire coating and an Ag paste to define bus lines. Obtained back contact are shown in figure 4.36: grey layer is Aluminium, white lines are the Argentums busses.

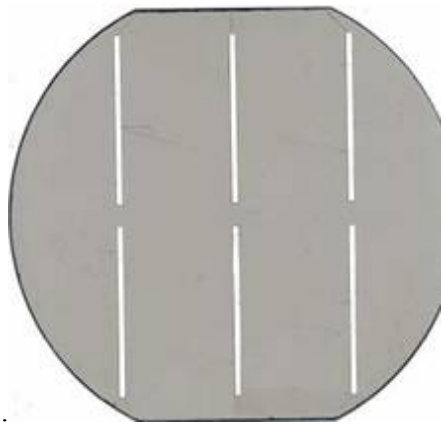

Figure 4.36 Backside contact realized by screen-printing process.

Unlike front contact, backside is geometrically characterized by Ag busses ~2.6mm wide and ~26µm thick. Aluminum layer is about 55µm thick.
Ag paste 3347 and Al paste 7229 have been used to create back side contact.
Sheet resistance measurement revealed a resistance of 0.04Ω/sq on Ag bus and of 0.09Ω/sq on Al layer, which considering layer thickness conducts to a resistivity of 4.05µΩ·cm.
The performed process step analysis till now described, allowed both to set up a manufacturing flow and to realize a productive line able to fabricate silicon wafer-based PV cells having electrical characteristics lined up to typical photovoltaic first generation technology.
Once reached this important result, successive studies centered on metallization and passivation steps were conduced in order to get higher efficiencies. Experiments have been especially directed toward the reduction of the series resistance depending on front contact: research objective was to increase contact surface without shaded area enlargement.
Front contact making process has been improved developing a double screen-printing procedure. It has been successfully tested an innovative method based on a second printing superimposed to the first one (after the standard drying) and followed by a second drying and, finally, a successive firing treatment. Structural difference between single and double screen-printing processes results could be noticed by SEM image comparison. Figure 4.37 shows SEM analyses executed on double printed front contact.

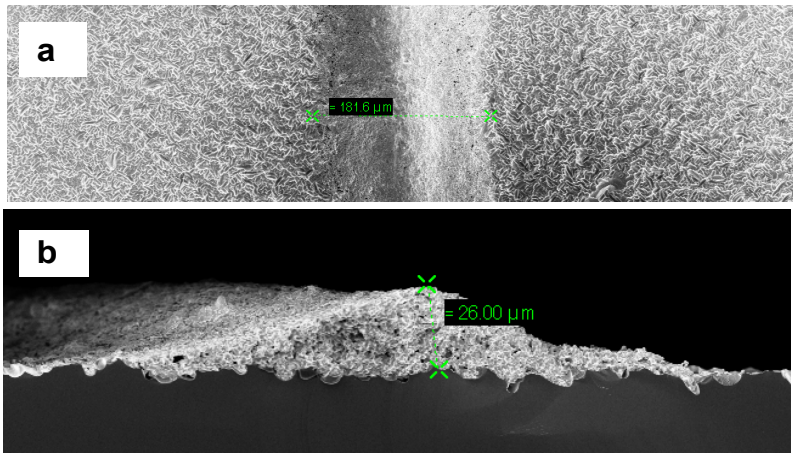

Figure 4.37 Front contact finger realized using double screen-printing process. a) Tilted SEM image. b) Cross section SEM image. Finger width is 181.6µm; finger maximum thickness is 26.00µm.

Double printed contact height is twice of standard contact while width is increased of about 60%. With this new structure a considerable series resistance reduction has been obtained with a less significant variation of shaded area. Measuring performed on both samples (single and double screen-printed cells) proved a series resistance decreasing from 0.035Ω to 0.0029Ω with an absolute efficiency improvement of ~5%.
Process upgrading required some equipment modification regarding the carrier belt control system, the lamps managing tools and the wafers automatic moving arrangement.

4.3 – TRANSPARENT CONDUCTIVE ZINC OXIDE PASSIVATION

As mentioned in paragraph 4.2.4, in addition to SiO_2 and SiN_x, an alternative material to passivate cell surface has been tested to realize a new anti-reflective coating and, thus, to re-define the connected front contact making process.
Dissimilar to previous described two materials, ZnO is a transparent conductive oxide (TCO) and its use as front contact influences positively both costs and electric performance of a PV cell. In fact, it can be used as antireflective coating and, at the same time, it represents an electrical conductive layer in order to collect the photogenerated current. Consequently, it allows both to reduce emitter contact resistance (decreasing the overall cell series resistance and improving global cell efficiency) and to simplify the successive front contact deposition, because the screen printing process can be performed at much lower temperature since the Ag penetration across an insulating passivation is not required. Moreover, the ZnO coating permits to enlarge the distance between the metal fingers, increasing the not shaded surface area.

The passivation process with ZnO developed inside this R&D project represents an innovative method based on an unconventional technology that use high-energy impulsed electrons to create a uniform TCO layer (Plasma Pulsed Deposition). To develop PPD process, a prototypal equipment specifically projected and realized by Meridionale Impianti has been employed [10] [11].

4.3.1 – Equipment functioning and simulation results

Equipment developed consists of a low-pressure chamber inside which a high-energy (15÷20KeV) Argon and Oxygen mixture is introduced into an electron gun to produce a ZnO solid target ablation. TCO deposition could be more stable if inside the reaction chamber a low quantity of Hydrogen is also introduced. Figure 4.38 represents the functioning scheme of an electronic gun.

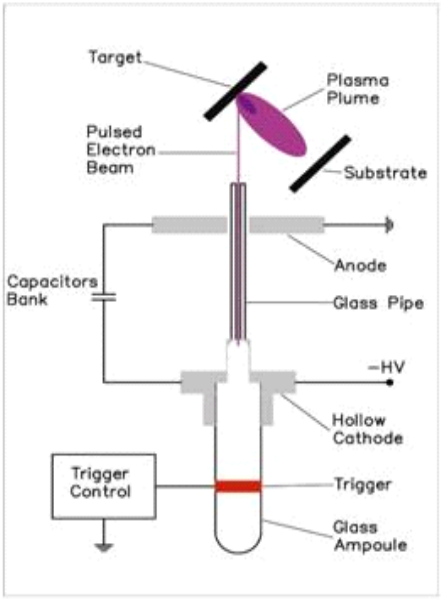

Figure 4.38 Impulsed electronic gun.

Normally, growth rate could vary between 10 and 30nm/min depending especially on gun-ZnO target distance. During entire process substrate temperature is maintained at low values facilitating passivation procedure and minimizing wafer thermal stress.

ZnO passivation process could be a crucial step in standard PV cell fabrication in terms of efficiency increasing (reducing front contact resistance) and production costs diminishing (eliminating contact firing procedure). For this reason research has been particularly pointed on this step. Research activity goals were firstly to arrange the ZnO PPD equipment in order to obtain a stable and repeatable procedure by a single source tool and, successively, to extend results on four sources depositions.

Principal purpose was to maximize deposition intensity reaching a high deposition rate and enhancing deposition extension and uniformity. This aim was indispensable to make this process applicable on industrial scale.
Final equipment building project has been based on 3D simulations afterwards verified and proved by experimental data. Simulations have been realized using appropriate software written in Microsoft Visual C++ 2005 through API graphic Microsoft DirectX 9.0c. Software utilized video board graphic processor to calculate energy spatial distribution in real time.
PPD deposition by a single source emission can be schematized as in the following figure 4.39.

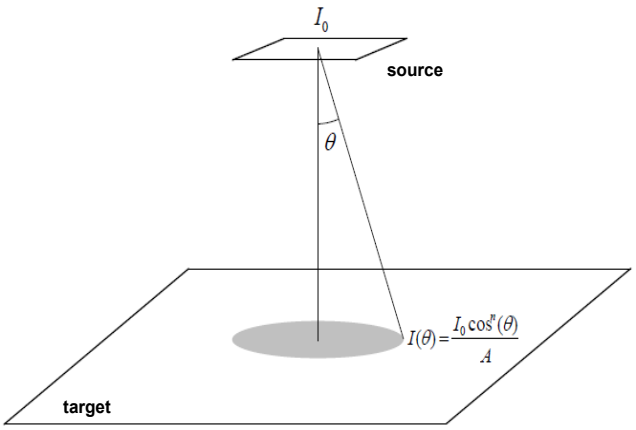

Figure 4.39 Single source PPD representation.

$I(\theta)$ is the intensity for a deposition angle θ, I_0 is the emitted particles total intensity, A is the total "illuminated" area and n is a source characteristic coefficient. Angular distribution coefficient n is a very important process parameter determined by PPD equipment working conditions and varying according to electronic gun intensity and energy.
For industrial applications, deposition uniformity is one of the most important parameter to define process quality and 3D simulations were indispensable to find best theoretical working conditions. To parameterize uniformity with synthetic data an irregularity limit of 5% on entire deposited area has been chosen as process quality criterion.

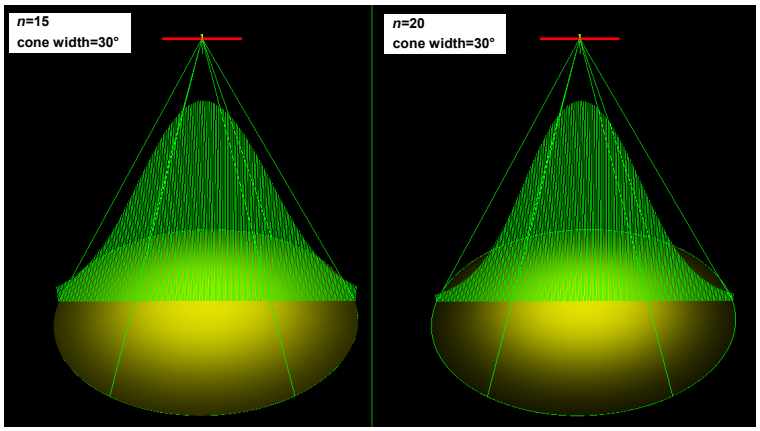

Figure 4.40 Calculated deposit spatial distribution for a single source emission.

Figure 4.40 shows the deposit spatial distribution obtained through simulation program in the case of a single source deposition for two values of *n* (*n*=15 and *n*=20). Results refer to a source-target distance of 12cm. Simulations better results have been obtained fixing *n*=15. Using same working parameters set up (*n*=15), deposit spatial distribution shown in figure 4.41 has been obtained in the case of four sources deposition.

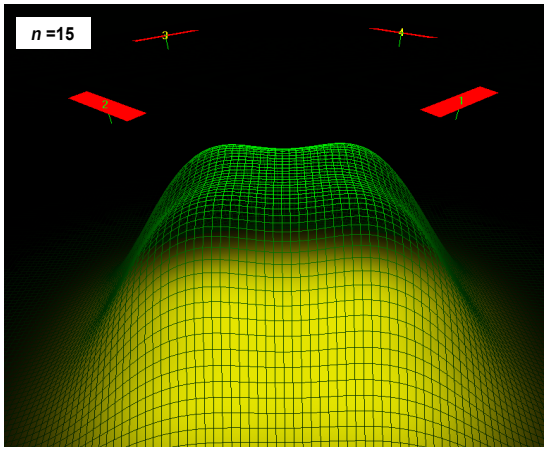

Figure 4.41 Calculated deposit spatial distribution for a four sources emission.

After system performance testing and theoretic results checking, a prototype equipment constructive designs have been built up. Realized prototype consists of a stainless steel chamber and of various control systems and detectors. Figure 4.42 shows the chamber design project and the realized deposition chamber with the relative control panel.

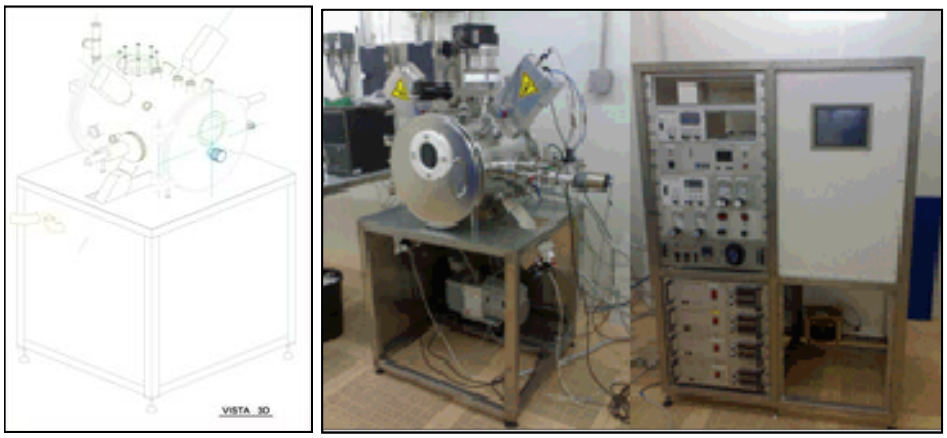

Figure 4.42 PPD chamber and respective control panel.

Entire tool is equipped with a gas feed valve to introduce inert gas (Nitrogen) into process chamber, a gas intake valve to regulate chamber gas loading, a pulsed beam generator (electronic gun), a rotating sample support and a vacuum production system constituted of a turbo-molecular pump, a rotational pump and an oil filtering structure. A panel containing tools fitted to manage PPD system working conditions controls all electronic elements.
By means of this equipment, many trials of ZnO deposits have been produced using in succession a system with one, two and finally four electron guns, obtaining a deposited areas enhancement from 20x20mm to 50x50mm and to 156x156mm respectively.
PPD process calibration required different parameters regulation to achieve desired deposit characteristics. Basic working parameters are:

- chamber pre-vacuum
- deposition vacuum
- pin valve setting
- gun pressure
- plasma accelerator voltage supplier
- target(s)-gun mutual distance
- shots number
- gun frequency

To start deposition process, after wafer positioning inside chamber, a vacuum of $6 \cdot 10^{-6}$mbar must be done closing all gas intake valves and turning on vacuum pumps. This operation is followed by the purge of the two branches forming gasses line. Subsequently, valves that intercept gas are opened and the temperature deposition set up using a potentiometer connected to a heating system.
Then, gas must be introduced into electronic guns and high voltage supplier is switched on. Acting on generator trigger and gas loading modulator, electronic

guns functioning is regulated and shots are stabilized. During all these starting phases, wafer to be processed is shielded from ZnO target by a shutter. Only when all correct operating conditions are satisfied, the shutter can be extracted giving rise to ZnO deposition on wafer. Timing process duration and knowing shots frequency, formed layer thickness could be estimated with a good approximation.
Deposition can be monitored during entire process through a porthole that consents to observe plasma plums formed at every shot going from target surface to substrate.
When process ends (before wafer unloading) power supply, heater and trigger must be turned off and all gasses intakes must be closed.
Experimental data and simulations results comparison allowed to determine best practical working conditions especially in terms of deposition rate and deposit uniformity. Top results using a single source deposition were attained under the following conditions:

- Chamber pre-vacuum $1.4 \cdot 10^{-5}$ Bar
- Deposition vacuum $4.8 \cdot 10^{-3}$
- Pin valve setting = 240
- Gun pressure = 2 Bar O_2
- Plasma accelerator voltage supplier = 13KV 2.5mA
- Target-gun distance = 11.5cm
- Shots number = 30000
- Gun frequency = 10Hz

The obtained deposit was uniform, 380nm thick and with a transmittance integrated on solar spectrum (400nm÷800nm) of 77%.
Acquired these data and verified their repeatability, has been implemented deposition by two guns trying to orient target, guns, substrate system, and setting depositions parameters up so as to increase deposition surface.
Target position compared to guns and substrate positions is the most important parameter to get suitable passivation layer uniformity. Plasma plum must be perpendicular to target surface direction, while ZnO target/gun position has been defined through computing simulations run during projecting phase.
Passing from a single source to double source deposition, oxygen intake valve must be varied diminishing gas introduction. Through the adjunctive gun, in fact, a little quantity of oxygen reached the chamber by means of this new way and so it was necessary to reduce gas flow acting on pin valve to avoid an excessive oxygen accumulation inside chamber. Different deposits have been performed on a $50x50mm^2$ substrate with the aim of acquire stable and repeatable deposition thickness and uniformity. These operations have been repeated until similar appropriate results have been obtained performing deposition by four guns, in order to cover a $156x156mm^2$ PV cell standard area.
Under the same previous operating conditions listed in the case of a single

source, after many trials, a configuration has been finally found to get the uniform layer.

4.3.2 – ZnO deposited film structural and electrical properties

The structure of a film obtained by a single source deposition is showed in figure 4.43, reporting the SEM image of a ZnO layer deposited on a not textured silicon wafer. Finest results, in terms of coating uniformity, have been obtained fixing a target-target distance of 11.5cm, a target-substrate distance of 14.5cm and a target inclination compared to substrate direction of 2°.

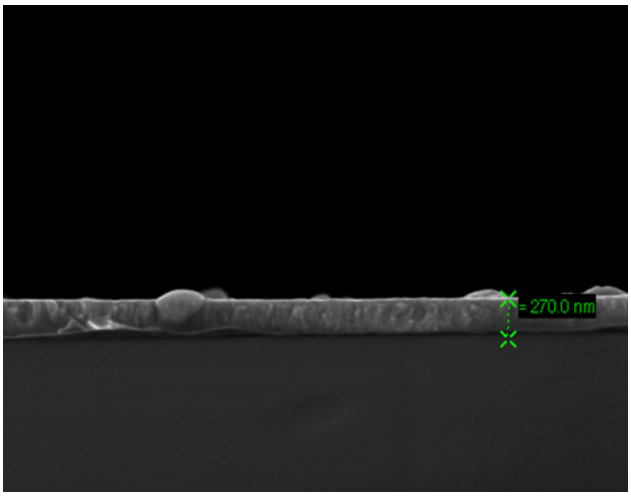

Figure 4.43 SEM analysis on ZnO layer deposited by PPD (single source). Layer is uniform and 270.0nm thick.

Layer structure has been studied by TEM and high energy electron diffraction analyses. Results are shown in figures 4.44 and 4.45 respectively.

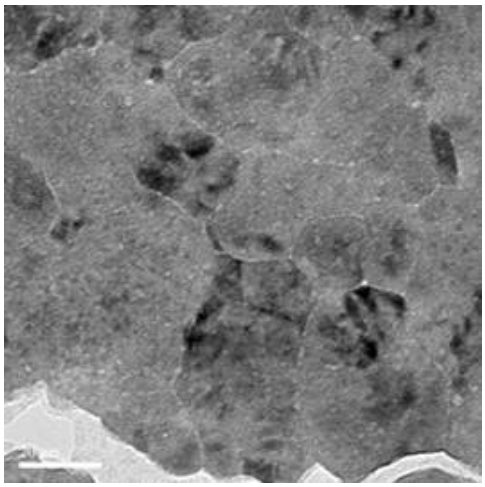

Figure 4.44 TEM analysis on ZnO layer deposited by PPD (single source).

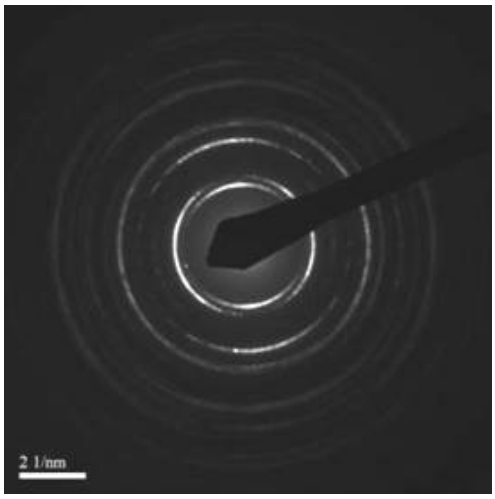

Figure 4.45 High energy electron diffraction pattern of ZnO layer deposited by PPD (single source).

TEM and electron diffraction highlight a typical polycrystalline structure.
Generally, ZnO deposited by PPD is polycrystalline or amorphous with morphology and grains dimension depending critically on process conditions. Consequently, it is necessary a systematic calibration work combining optical and physical measures.
For every deposition carried out varying electronic guns parameters (and consequently growth rate), the ZnO layers microscopic structure obtained by PPD equipment was the same. This result proves method repeatability and

process equipment stability. Figure 4.46 reports the SEM images of a textured silicon wafer before (a) and after (b) ZnO deposition.

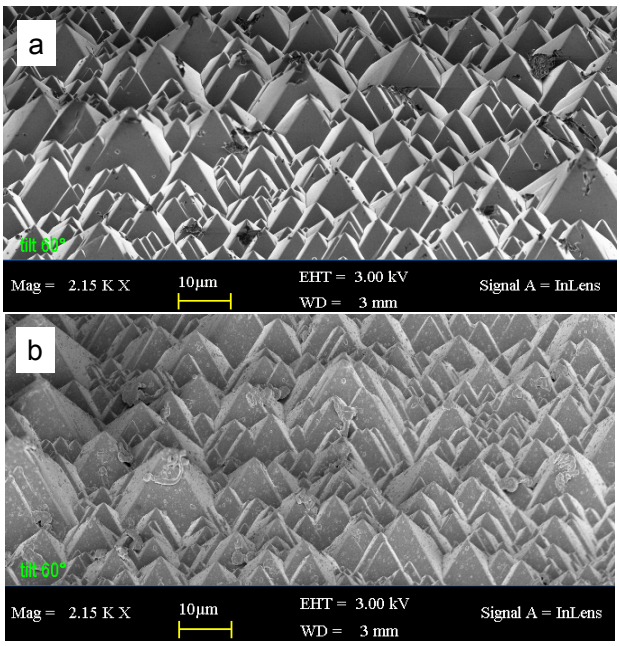

Figure 4.46 Textured mono-crystalline Silicon SEM planar view. a) after texturing process. b) after ZnO PPD process.

ZnO layer is uniform over entire surface and presents grains few microns large deposited on <111> pyramids sides. Figure 4.47 illustrates the cross section analysis and demonstrates coating uniformity.

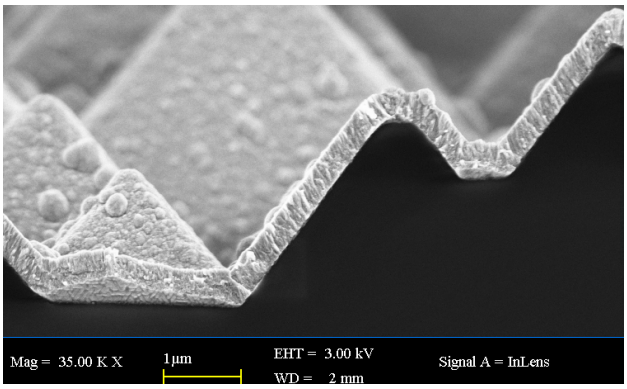

Figure 4.47 Cross section SEM analysis on ZnO passivation layer 350nm thick. Film follows regularly textured surface structure without hillocks or fractures.

Film follows regularly textured surface structure without hillocks or fractures. Roughness is contained inside the range 8÷15nm.
ZnO layer has a high mechanical stability and good electric propriety in terms of resistivity. For the sample reported in figure 4.47, measured average resistivity is 87mΩ·cm. Layer resistivity depends on deposition conditions and, according to simulations data, can vary from 100 to ~1mΩ·cm. Superficial resistance is a very important factor in photovoltaic applications and it varies from tens to thousands of Ohm, depending also on deposited thickness.
Resistivity results inversely proportional to chamber vacuum during deposition process. Figure 4.48 shows resistivity got for three different deposition pressure values.

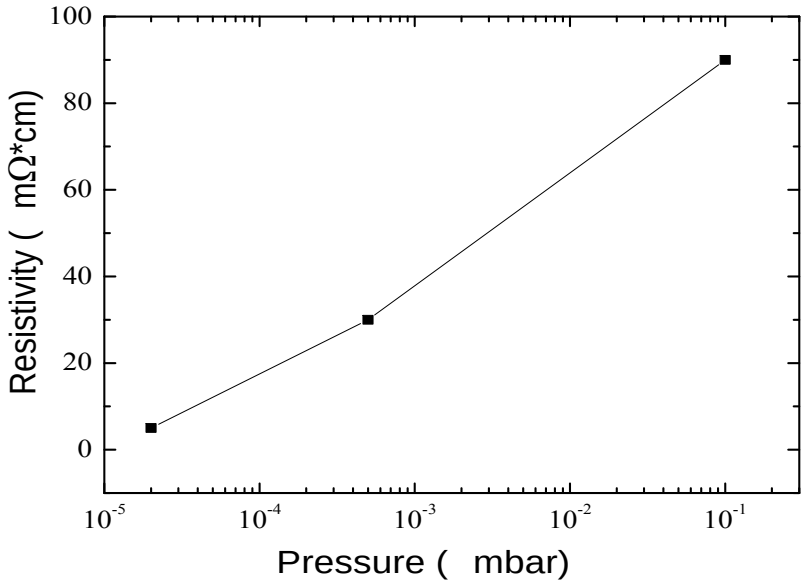

Figure 4.48 Resistivity as a function of pressure (T=200°C). A pressure range from $2 \cdot 10^{-5}$ to 10^{-4}mbar gave the most satisfactory results.

A temperature range from 100°C to 350°C and a pressure range from $2 \cdot 10^{-5}$ to 10^{-4}mbar gave most satisfactory results. Best-measured resistivity was 1.8mΩ·cm (48.5Ω/sq) that represents the lowest value reached. However, considering all performed tests, a values range up to 250Ω/sq has been obtained.

4.3.3 – ZnO deposited film optical properties

In order to characterize optical proprieties of ZnO films produced by PPD method, a series of deposition on quartz samples have been performed. Optical measurements made on films were carried out by using a spectrometer and include reflectance and transmittance measured at normal incidence over the UV-VIS range of wavelength.

The reflective and transmissive properties of films have been calculated from electromagnetic theory, in terms of the refractive index and layer thickness. For the general case (shown in figure 4.49) of light incident at an angle β_0 on a film of refractive index n_1 and thickness d_1 deposited on a substrate of index n_2, the reflectance R and the transmittance T can be determined by means of Fresnel coefficient of reflection and transmission at air/film and film/substrate interfaces.

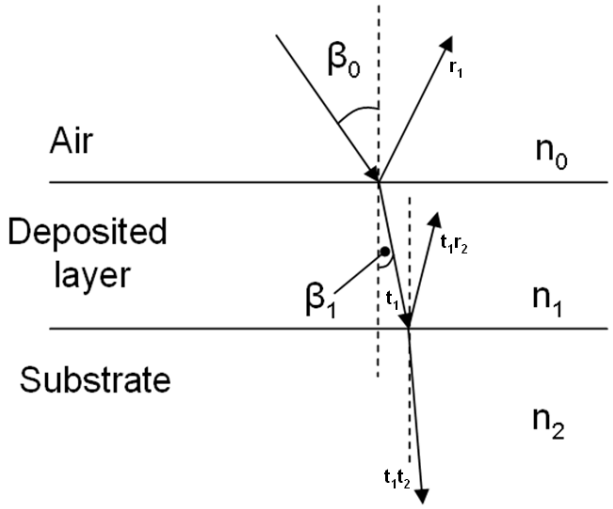

Figure 4.49 Reflection and refraction of incident light at air/deposited layer and layer/substrate interfaces.

For polarized, light with electric vector lying on the plane of incidence, the Fresnel amplitude reflectance and transmittance coefficients are respectively:

$$r_{1p} = \frac{n_1 \cos\beta_0 - n_0 \cos\beta_1}{n_1 \cos\beta_0 + n_0 \cos\beta_1} \tag{4.8}$$

$$t_{1p} = \frac{2n_1 \cos\beta_1}{n_1 \cos\beta_0 + n_0 \cos\beta_1} \tag{4.9}$$

with n_0 refractive index of the air [12].
For polarized light with electric vector perpendicular to the plane of incidence, the corresponding quantities are:

$$r_{1s} = \frac{n_1 \cos\beta_1 - n_0 \cos\beta_0}{n_1 \cos\beta_1 + n_0 \cos\beta_0} \tag{4.10}$$

$$t_{1s} = \frac{2n_1 \cos\beta_1}{n_1 \cos\beta_1 + n_0 \cos\beta_0} \tag{4.11}$$

In the particular case of normal incidence ($\beta_0=\beta_1=0$), Fresnel coefficients for reflection and transmission become:

$$r_{1p} = r_{1s} = \frac{n_1 - n_0}{n_1 + n_0} \tag{4.12}$$

$$t_{1p} = t_{1s} = \frac{2n_1}{n_1 + n_0} \tag{4.13}$$

Total reflectance and transmittance are determined by summing the multiply reflected and transmitted beams, taking into account of the phase difference $\delta_1=2\pi\upsilon n_1 d_1 \cos\beta_1$ (with υ wavenumber) between successive beams. It should be noted that generally n_0, n_1 and n_2 are functions of υ. The result of the sum is given by:

$$R = \frac{r_1^2 + 2r_1 r_2 \cos 2\delta_1 + r_1^2}{1 + 2r_1 r_2 \cos 2\delta_1 + r_1^2 r_2^2} \tag{4.14}$$

$$T = \frac{n_2}{n_0} \frac{t_1^2 t_2^2}{1 + 2r_1 r_2 \cos 2\delta_1 + r_1^2 r_2^2} \tag{4.15}$$

where the Fresnel coefficients for either components are inserted.
The variation of R with δ_1 could be considered as the variation of R with thickness for a given wavenumber. If the film is sufficiently thick, two or more peaks can be obtained in a spectrometric curve for normal incidence and then the optical thickness $n_1 t_1$ may be calculated.
Finally, if the film material is absorbent the propagating wave may be described by a complex index (n_1-ik_1). The real part of the refractive index indicates the phase speed, while k_1 indicates the amount of absorption loss when the electromagnetic wave propagates through the material. The physical significance of k_1 is that for a length of path equal to one vacuum wavelength, the attenuation is $exp(-2\pi k_1)$.
Expressions for R and T of an absorbent film may be obtained by substituting (n_1-ik_1) in place of n_1 in the expressions of Fresnel coefficients, performing the sum and evaluating the square of the modulus of the resulting amplitudes.

$$R = \frac{(n_1 - n_0)^2 + k_1^2}{(n_1 + n_0)^2 + k_1^2} \tag{4.16}$$

$$T = \frac{16 n_0 n_2 (n_1^2 + k_1^2)^2}{[(n_1 + n_2)^2 + k_1^2][(n_1 + n_0)^2 + k_1^2]} e^{-4\pi\nu d_1 k_1} \tag{4.17}$$

If the film to be examined is deposited on a transparent substrate, like a quartz substrate, then transmittance and reflectance measures enables to determine optical constants and thickness [12] [13].
In figure 4.50 the reflectance measured for a ZnO thin film deposited on a quartz substrate versus the incident wavelength is plotted. Square dots represent experimental data; red line is the best-fit.

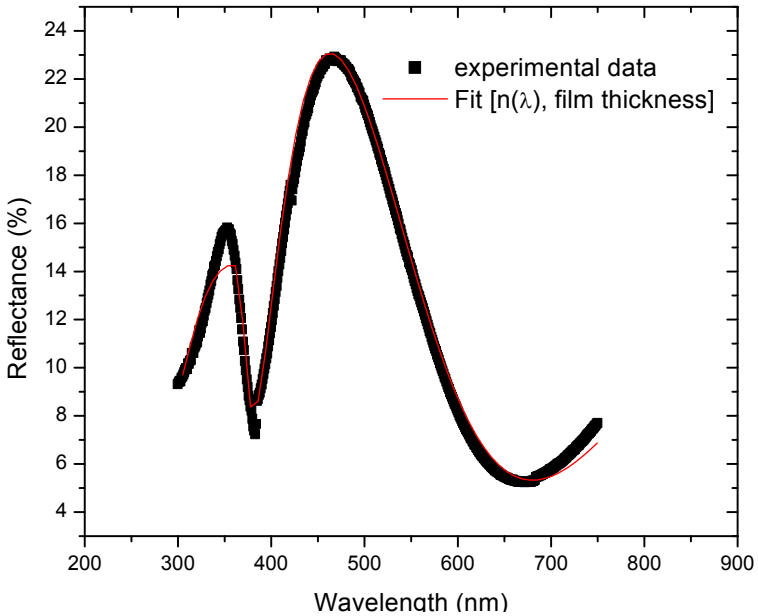

Figure 4.50 Deposited ZnO film reflectance versus incident wavelength. Best-fit provided a thickness value of (165±5)nm.

The fit of the experimental data has been performed using as fit parameters ZnO refractive index $n(\lambda)$ and film thickness d. To determine refractive index has been applied the Forouhi-Bloomer analysis [13].
Best-fit provided a thickness value of (165±5)nm and the $n(\lambda)$ reported in figure 4.51.

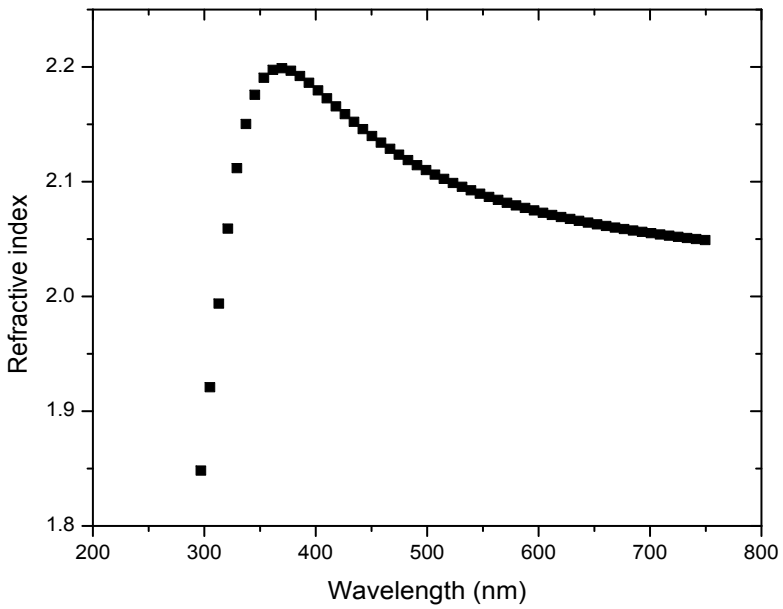

Figure 4.51 Calculated ZnO film refractive index versus incident wavelength.

Once an estimation of the film thickness *d* has been obtained, the relative absorption coefficient (as a function of wavelength) can be evaluated making use of the transmittance spectrum. In fact, absorbance *A*, reflectance *R* and transmittance *T* are connected by the relation:

$$A+R+T=1 \tag{4.18}$$

Thus, using the well known Lambert-Beer law, is possible to calculate the absorption coefficient of the deposited film $\alpha(\lambda)$, and the related imaginary part of the refractive index $k(\lambda)$, from the following equation:

$$R+T= 1-A = e^{-\alpha(\lambda)d} = e^{-\frac{4\pi}{\lambda}k(\lambda)d} \tag{4.19}$$

The transmittance measured inside the range of wavelengths from 200nm to 1100nm for the same ZnO deposit is shown figure 4.52.

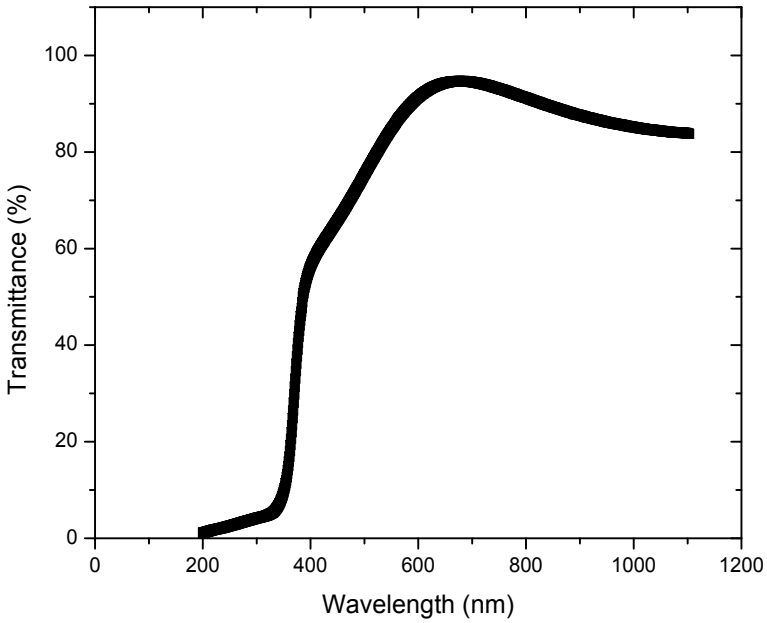

Figure 4.52 Measured ZnO film transmittance versus incident wavelength.

The computed ZnO film absorption coefficient, versus the incident wavelength, is plotted in figure 4.53.

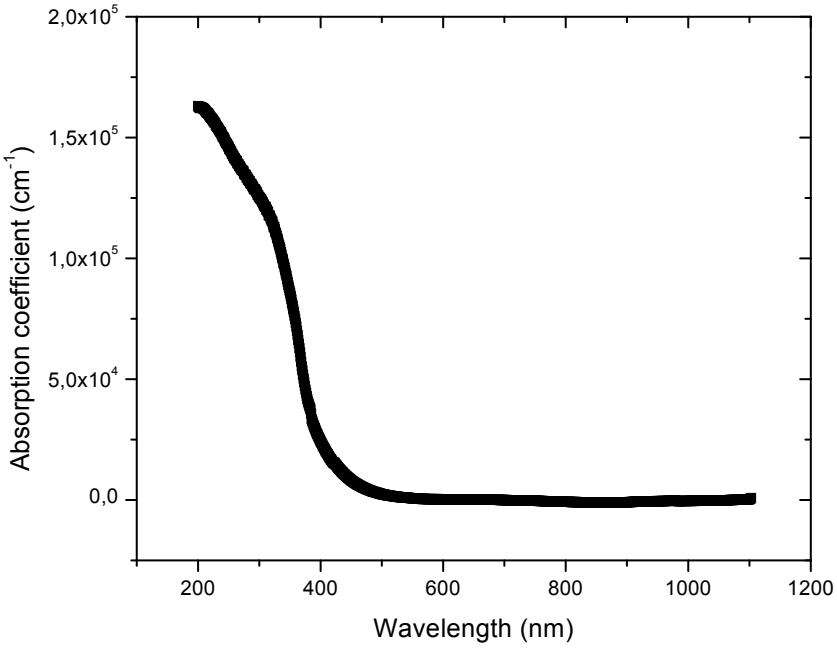

Figure 4.53 Calculated ZnO film absorption coefficient versus incident wavelength.

As illustrated, optical and electrical properties of the deposited ZnO layer encounter the PV technology requirement opening the prospective of an innovative front contact process that allows both manufacturing cost reduction and device efficiency improving.

4.3.4 – Effect of ZnO coating on PV cell

Making use of the results previously explained, in terms of electrical and optical ZnO film properties, the effect on PV cell efficiency of a ZnO deposit used as front contact and ARC has been evaluated. The ZnO layer is electrically conductive and optically absorbent, consequently it influences both cell series resistance and photo-generated current, in function of its thickness. These two contributions could be estimated independently to calculate the end result on device performance.

Figure 4.54 reports the computed photocurrent versus the ZnO film thickness. Reported results have a general validity and are applicable at every silicon wafer-based PV cell (whatever its geometrical properties may be) since calculated photocurrent has been normalized with respect to the current generated in the ideal case in which all incidents photons create charges couples completely collected by metal contacts (i.e. neglecting silicon reflectivity and assuming total absorption). The analysis has been performed for both a textured (black square) and a not treated (white circle) wafer surface.

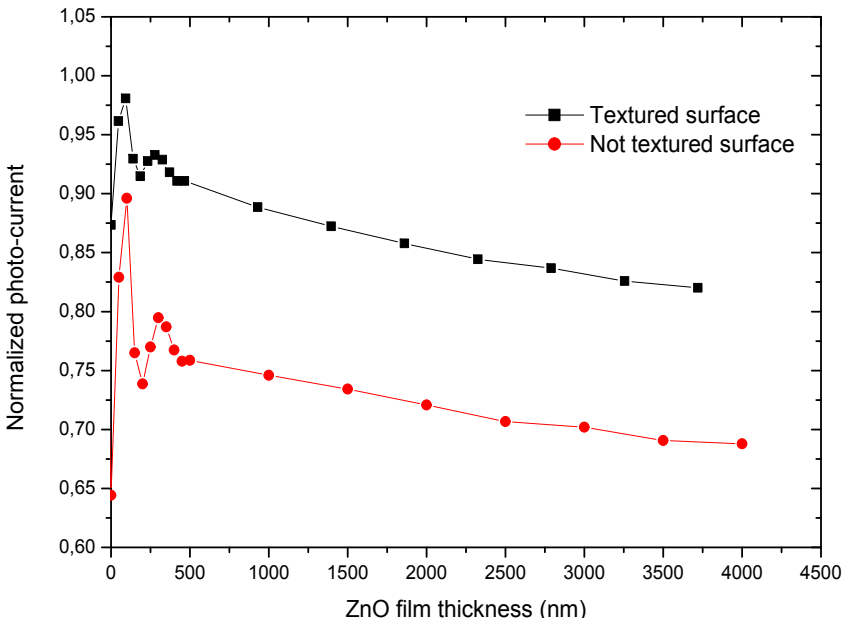

Figure 4.54 Normalized calculated photocurrent versus ZnO film thickness. Curves oscillations are consequence of the interference phenomena involving the rays of light reflected and transmitted at air/ZnO and ZnO/Silicon interfaces. The decreasing trend for thickness greater than 500nm is caused by the increasing of layer absorption.

Curves oscillations are consequence of the interference phenomena involving the rays of light reflected and transmitted at air/ZnO and ZnO/ silicon interfaces. The decreasing trend for thickness greater than 500nm is caused by the increasing of layer absorption.
To evaluate the effect of the ZnO layer on the series resistance it is necessary to define the PV cell area and the front contacts layout. These parameters determine the path covered by the photogenerated charges before their collection at metallic contacts. The R_s calculated for the particular realistic case of a 156x156mm^2 square cell (with the structural parameters values reported in table 3.1), having 64 metallic fingers is plotted in figure 4.55 as a function of the film thickness. The considered ZnO resistivity was 5mΩ·cm, a value consistent with the experimental results obtained by PPD method under standard operating conditions.

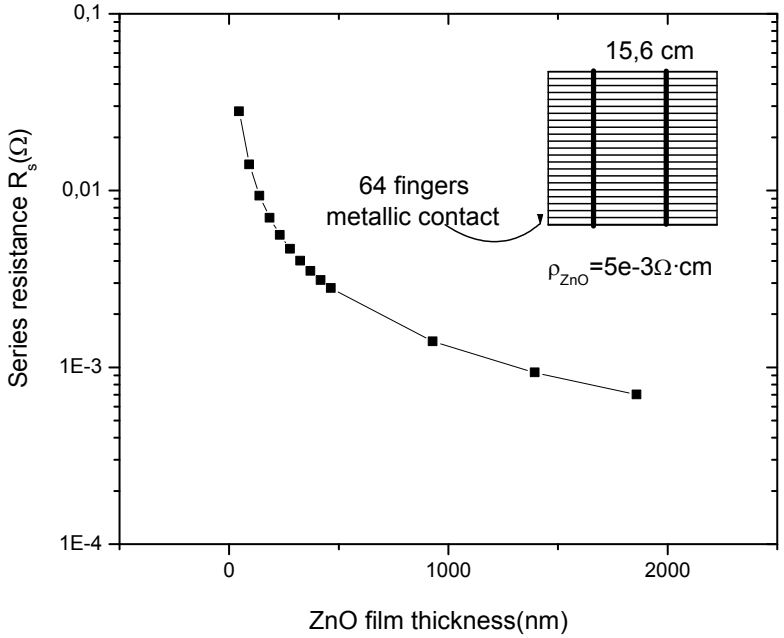

Figure 4.55 Series resistance as a function of ZnO film thickness. R_s values suitable for photovoltaic technology (~mΩ) could be obtained for ZnO deposit thickness higher than few thousand of nanometers (≥300nm).

The calculation has been carried out neglecting the contact resistance due to metal/ZnO interface.
Plot highlights that R_s values suitable for photovoltaic technology (~mΩ) could be obtained for ZnO deposit thickness higher than few thousand of nanometers (≥300nm).
Single contributions to and the global effect on PV device efficiency of the ZnO coating (for the same cell previously considered) are shown inside figure 4.56.

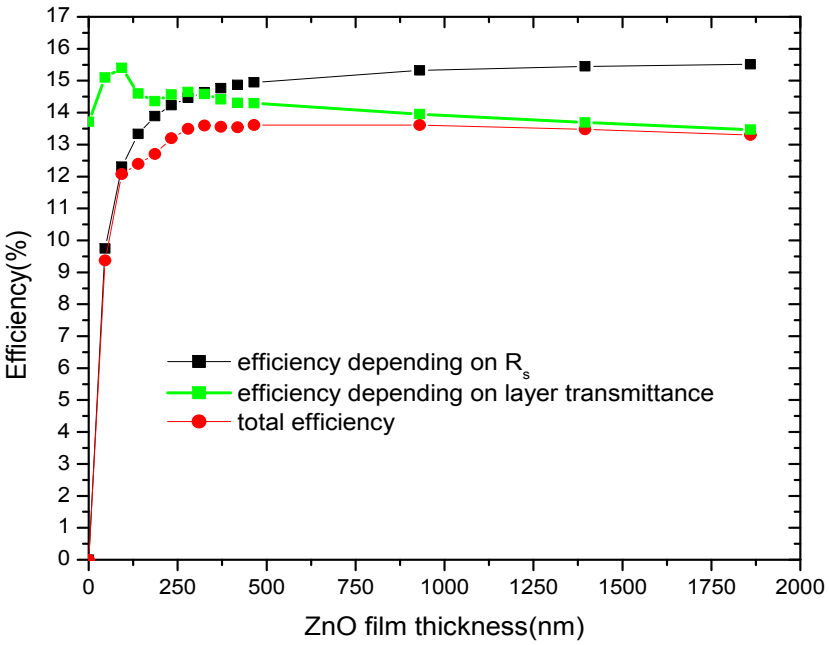

Figure 4.56 Calculated cell efficiency versus ZnO film thickness. The best cell efficiency has been obtained for a film 325nm thick. For higher thickness, the performance worsening due to the coating film absorption exceeds the improvement resulting from the decreasing of series resistance.

Starting from a thickness value of zero (i.e. no ZnO deposit), the total efficiency grows until reaching a maximum value. After this peak, efficiency decreases progressively increasing ZnO thickness.
In the particular case treated, the best cell efficiency has been obtained for a film 325nm thick. For higher thickness, the performance worsening due to the coating film absorption exceeds the improvement resulting from the decreasing of series resistance.
To prove the PV cell upgrading by means of a ZnO coating, a prototype 50x50mm^2 cell (textured CZ <100> silicon, with a phosphorous doped emitter 0.4µm deep) has been produced. An electrical characteristics comparison between the sample before (white circle) and after (black square) the ZnO film deposition (350nm thick) is reported in figure 4.57 (*I-V*) and 4.58 (*P-V*).

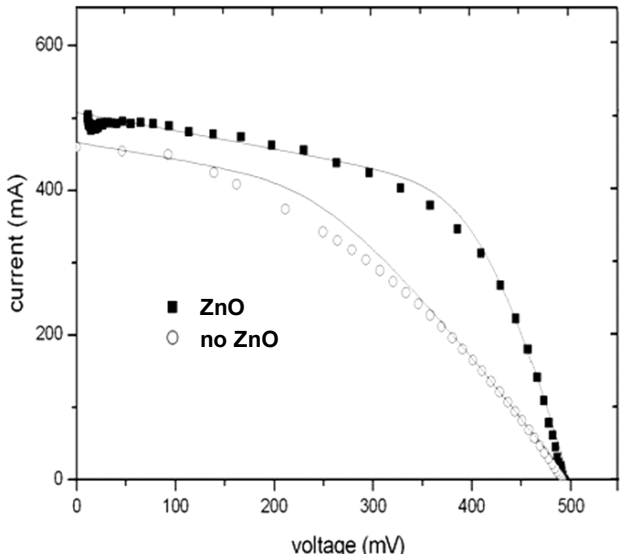

Figure 4.57 Comparison between *I-V* characteristics of two 50x50mm^2 prototypal cells with ZnO and SiO_2 passivation. Trial cell with the ZnO coating shows better fill factor and higher photocurrent than cell passivated with traditional SiO_2.

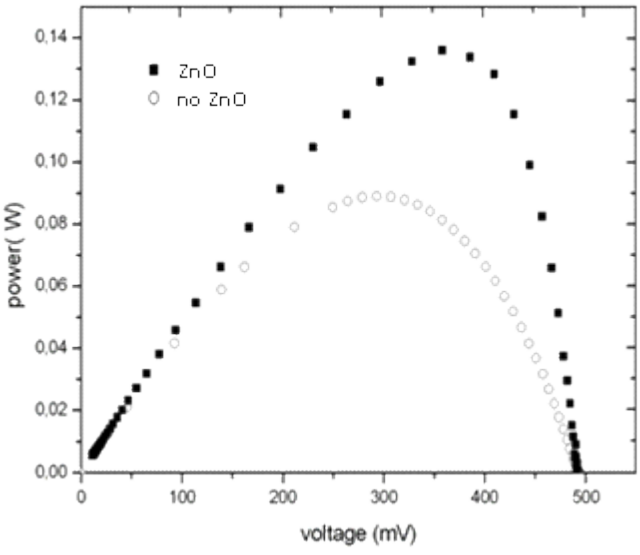

Figure 4.58 Comparison between P-V characteristics of two 50x50mm^2 prototypal cells with ZnO and SiO_2 passivation. Trial cell with the ZnO coating shows higher power peak than cell passivated with traditional SiO_2.

It has been demonstrated that innovative process flow with ZnO could improve cell efficiency. Obtained results highlight the importance of the innovative technique investigated: it is very advantageous because simplify entire PV cell process flow (decreasing production costs through energy saving) and improving final cell efficiency.
ZnO deposition performed by PPD developed inside present project opens interesting prospects in the sphere of process flow simplification and necessities of a dedicated industrialization program directed towards large scale production.

References

[1] G. Coletti, N.J.C.M. van der Borg, S. De Iuliis, C.J.J. Tool and L.J. Geerligs, *Mechanical Strength of Silicon Wafers Depending on Wafer Thickness and Surface Treatment*, ECN Energy Research Centre of the Netherlands (2006).

[2] G. Coletti, C.J.J. Tool and L. J. Geerligs, *Quantifying Surface Damage by Measuring Mechanical Strength of Silicon Wafers*, ECN Energy research Centre of the Netherlands (2005).

[3] Sparber W. et alt. *Comparison of Texturing Methods for Mono-crystalline Silicon Solar Cells Using KOH and Na_2CO_3*, 3rd World Conference on Photovoltaic Energy Conversion Osaka (2003).

[4] Melnyk I., Wefrighaus E., McCann M., Helfricht A., Hauser A., Fath P., *NA_2CO_3AS An Alternative to NAOH/IPA for Texturisation of Mono-crystalline Silicon* (2004).

[5] Hilali M.M. and Rohatgi A., *A Review and Understanding of Screen-Printed Contacts and Selective–Emitter Formation*, NREL - National Renewable Energy Laboratory (2004).

[6] Kopecek R., Buck1 T., Liba11 J., Röver I., Wambach K., Geerligs L.J., Sánchez-Friera P., Alonso J., Wefringhaus E., Fath P., *Large Area Screen Printed n-type Silicon Solar Cells With Rear Aluminium Emitter: Efficiencies Exceeding 16%* (2006).

[7] Sze S, Physics of Semiconductor Devices, 2nd Edition, John Wiley & Sons, New York, NY (1981).

[8] Luque A., Hegedus S., *Handbook of photovoltaic science and engineering* , John Wiley & Sons, New York, NY (2003).

[9] Jakubka, L. Klumpler, A. Szendiuch, I., *Application of screen printing by photovoltaic cell realization*, Dept. of Microelectron., Brno Univ. of Technol. (2005).

[10] A. A. Serdobintsev, A. G. Veselov, O. A. Kiryasova, S. A. Portnov and D. N. Bratashov*, Low-temperature plasma pulsed deposition of thin films with nanoscale periodicity of properties* (2009).

[11] Ellmer K., Klein A., Rech B., *Transperent Conductive Zinc Oxide*, Springer (2007).

[12] Stenzel O., *The Physics of Thin Film Optical Spectra* (2005).

[13] Heavens O. S., *Thin film Physics* (1970).

5. A New Method to Evaluate the Series Resistance of PV Cells from *I-V* Characteristics

5.1 – INTRODUCTION

As previously discussed, parasitic resistance values influence critically the performance of a PV cell modifying significantly the features of its *I-V* characteristic. Nowadays, parasitic resistances effects have been reduced to very low level: in a standard silicon PV cell of about 200cm^2 surface area, shunt resistance of the order of 10÷100Ω is obtained by edge passivation and series resistance as low as few mΩ is obtained using even low cost technologies (for example "screen printing" for front contacts).
So, it is of great relevance the availability of a measurement method able to determine such values of series resistance with good accuracy to monitor industrially produced devices. In fact, especially for low values of the shunt resistance, large error can occur in the estimation of the R_s if R_{sh} is not correctly evaluated.
For a more general purpose, the method must also allow measurements over a resistances range as large as possible so to include also worse quality cells (for example having low shunt resistance) in order to test innovative fabrication procedures.
In this chapter, a general method to determine the parasitic resistances of a PV cell (or a panel) from its electrical characteristics under solar irradiation is presented. The method makes use of a cell *I-V* curve measured at a fixed sun irradiation and a dataset of short circuit current I_{sc} and open circuit voltage V_{oc} values taken at various levels of sun irradiations. The method involves different fitting procedures iteratively performed on these two dataset.

5.2 – STANDARD METHODS

The internal reverse current of the cell is assumed to be the direct characteristic of a diode in parallel to the photocurrent source (figure 2.6). In the case of a silicon photovoltaic cell, this characteristic is the direct characteristic of the silicon *n-p* diode junction. As seen in chapter 2, the commonly assumed Shockley equation for the diode direct characteristic $I_D(V)$ is:

$$I_D(V) = I_0\left(e^{\frac{qV}{nKT}} - 1\right) \tag{5.1}$$

already used in equation (2.2). V the voltage across the diode terminals, q, K_B, T and I_0 are the electron charge, Boltzmann constant, temperature and saturation current respectively. The "ideality factor" n takes into account the deviation of a real diode from the ideal one and fits the experimental diode characteristic in order to take into account several mechanisms involved for the current flow inside the diode. This is the so called "single diode" approximation commonly adopted in the *I-V* characteristic description of a PV cell.
For non conventional silicon cells, equation (5.1) is surely not a good assumption for the internal reverse current. Moreover, even in the case of a conventional silicon based cell, equation (5.1) may be not an adequate approximation. Several phenomena like, for example, the interplay between the diffusion of minority carriers in the doped layers, the charge recombination in the depletion layer, the effect of high carrier injection level, the voltage drop between the back contact and the edge of the depletion layer, the shortness of the doped layers on respect of the diffusion length of the minority carriers, the surface recombination effects and so on, may strongly reduce the reliability of such a simple formula for the description of the diode current [1].
Different analytical expression can be used in order to approach a real diode characteristic. In the present work, an interpolation of same experimental data by a double term Shockley equation has been performed. This is as if two Shockley's diodes with different ideality factors are shunted to the current generator ("double diode" approximation) which has been demonstrated to be a better model for a detailed analysis of a PV cell characteristic [2]. Other expressions are, however, suitable to be used depending on the peculiar cell under analysis.
The equivalent circuit of a PV cell has been already illustrated in figure 2.6: one or two diode shunting the light generated photocurrent I_{ph} represent the use of the single diode or the double diode approximation adopted to describe the reverse current of the cell I_D (i.e. the diode direct current). According to this circuital model, the most general form for the cell characteristic is expressed by the equation

$$I(V) = I_{ph} - I_D\left(V + IR_s\right) - \frac{V + IR_s}{R_{sh}}. \qquad (5.2)$$

The methods used to determine the R_s and R_{sh} values take origin from treating equation (5.2) with different approximations.
Firstly the "slope method": very roughly, the values of R_s and R_{sh} can be easily estimated by equations (3.7) and (3.8) obtained assuming the I_D derivatives $dI_D/d(V+IR_s)=0$ for $V+IR_s=0$ and $[dI_D/d(V+IR_s)]^{-1}=0$ for $V+IR_s=V_{oc}$. The first of the two conditions is in practice enough valid for silicon conventional PV cells,

while the second is in general not satisfied, conducting to over-estimated values of R_s with very large relative error for low R_s values.
The values obtained by these rough estimations are anyway suitable to be used as starting point for some other procedures.
The standard method recommended by the International Electrochemical Commission (IEC) [3] for R_s measurements use to compare two (or more) *I-V* characteristics obtained with different sun irradiances. This method does not make any assumption for the expression of $I_D(V+IR_s)$ but it provides a correct value of R_s only in the limit of $R_{sh}\rightarrow\infty$.
Instead, from a single *I-V* characteristic with a constant illumination, a "derivative method" is often used: the series resistance R_s and the ideality factor n are obtained from a plot of the characteristic derivative versus $(I_{sc}-I)-1$. In fact, from equation (5.2), using the single diode approximation it is obtained:

$$\frac{dI}{dV} - 1 = -R_s - n\frac{KT/q}{I_{sc} - I} \tag{5.3}$$

This is a very simple method from experimental point of view but it must be pointed out that two critical assumptions are made to equation (5.2) to derive equation (5.3):

a) it is assumed that $R_{sh}\rightarrow\infty$
b) I_D must be well approximated by the simple Shockley equation with a single term.

Moreover, experimental uncertainties in the determination of the *I(V)* derivative pose important limits to the precision of the method.
More recently, Ishibashi et al. proposed a new method overcoming the first of the above mentioned limitations [4]. In the Ishibashi method, $(dI/dV)-1$ is derived from equation (5.2) without the assumption $R_{sh}\rightarrow\infty$ and it is expressed as function of a parameter χ which involves both $(I_{sc}-I)$ and R_{sh} and approaching $(I_{sc}-I)-1$ when R_{sh} becomes larger and larger. R_s, R_{sh} and n are then obtained through an iterative fitting procedure of the $(dI/dV)-1$ plot as a function of χ.
Even in this case, however, the single diode approximation for $I_D(V+IR_s)$ is assumed. In addition, the same experimental limitations occurring from the experimental uncertainties in the evaluation of the *I(V)* derivative can be significant.
Many other methods have been reported in the literature in the past years but all of them make use of at least one of the two assumptions on R_{sh} and I_D above mentioned.
Theoretically, most of the mentioned limitations of the above described methods could be overcome by directly fitting equation (5.2) to the experimental *I-V* characteristic. However, the large number of parameters that have to be determined by the fitting procedure (R_s, R_{sh}, I_{ph} and all the parameters needed in any functional form used to describe $I_D(V+IR_s)$) and their mutual interaction in determining the shape of the experimental curve conduct to large instabilities

and very strong dependence of the result of any least-square method procedures on the choice of the initial parameters values.

5.3 – A NEW METHOD: THEORY

The present method avoids the problems related to standard methods since it is based on the fitting of two independent set of data:

- one *I-V* characteristic at a fixed sun irradiance
- one dataset of values pairs (I_{sc}, V_{oc}) obtained at different sun irradiances.

The method starts from the consideration that, as demonstrable from equation (5.2), in the case of negligible parasitic resistances the dataset (I_{sc}, V_{oc}) obtained at different sun irradiances represents an experimental evaluation of $I_D(V+IR_s)$. This dataset can be easily fitted with any suitable analytical form. In the case that R_s and R_{sh} are not negligible, instead, they may represent however a first approximation of $I_D(V+IR_s)$ that can be improved if good approximations of R_s and R_{sh} are provided.
On the other hand, once I_D is determined, least square fitting of the *I-V* characteristic by equation (5.2) having only R_s, R_{sh}, and I_{ph} as fitting parameters is easily obtained. So, by iterating different separate fitting procedures, with a reduced number of parameters to be determined each, easily convergence to unique and stable values of all the investigated parameters is achieved.
The value of sun irradiance used to acquire the (I_{sc}, V_{oc}) is not necessary to be known (unless efficiency must be evaluated). The sun irradiance used for the measure of the *I-V* characteristic should be within or not too much out of the range used for the measure of the dataset (I_{sc}, V_{oc}) .
The sun irradiance level, for a given cell, determines a single value of I_{ph}. From equation (5.2), for a given illumination level, the value of V_{oc} and I_{sc} are related to I_{ph} by

$$I_{ph} = I_{sc}\left(1 + \frac{R_s}{R_{sh}}\right) + I_D\left(I_{sc} R_s\right) \tag{5.4}$$

and

$$I_D(V_{oc}) = I_{ph} - \frac{V_{oc}}{R_{sh}}. \tag{5.5}$$

For an ideal cell without parasitic resistances ($R_s=0$ and $R_{sh}\rightarrow\infty$), from equations 5.4 and 5.5 follows:

$$I_{sc} = I_D(V_{oc}) \tag{5.6}$$

So that the dataset of values pairs (I_{sc},V_{oc}) can be taken as an experimental evaluation of the diode direct characteristic I_D. This set represents only an approximation which in general overestimates the value of I_D. This approximation can be improved if realistic values of R_s and R_{sh} and an estimate of I_D ($I_{sc}R_s$) are given.
In fact, the exact expression connecting I_{sc} and V_{oc} is, from equations (5.4) and (5.5):

$$I'_{sc}=I_D(V_{oc}) \tag{5.7}$$

with

$$I'_{sc} = I_{sc}\left(1+\frac{R_s}{R_{sh}}\right)+I_D(I_{sc}R_s)-\frac{V_{oc}}{R_{sh}} \tag{5.8}$$

So, using I'_{sc} evaluated by equation (5.8), a better approximation of I_D is then represented by the dataset (I'_{sc},V_{oc}). Present method is an iterative procedure composed by the following steps:

Step 0) To set an initial dataset (I'_{sc},V_{oc}). It could simply be the initial dataset (I_{sc},V_{oc}) or, for a better approximation, the values I'_{sc} obtained by equation (5.8) assuming for R_s and R_{sh} the rough values estimated by any other evaluation method (for example evaluating the dI/dV derivatives by the "slope method"). At this step, the term I_D (I_{sc} R_s) in equation (5.8) can be neglected.
Step 1) To fit the initially set (I'_{sc},V_{oc}) pairs. Once the dataset (I'_{sc},V_{oc}) is available, a suitable function can be fitted on it (single or double diode approximation or any other analytical form depending on the peculiar cell under investigation). It must be noted that, for the purpose of determining the parasitic resistance values the chose of the particular analytical expression for $I_D(V+IR_s)$ is not very critical and does not have any particular physical meaning. It provides a good interpolation of the dataset (I'_{sc},V_{oc}).
Step 2) To fit, by a suitable least square method, equation (5.2) to the experimental I-V characteristic having R_s and R_{sh} as fitting parameters and assuming for $I_D(V+IR_s)$ the expression obtained in step 1). I_{ph} in equation (5.2) is not an independent fitting parameter since it is related to the experimental value of the I_{sc} of the characteristic by equation (5.4).
Step 3) To evaluate by equation (5.8) a new dataset (I'_{sc},V_{oc}) using the values of R_s and R_{sh} obtained in step 2). The term $I_D(I_{sc}$ $R_s)$ is evaluated using the $I_D(V+IR_s)$ expression previously obtained in step 1).
Steps 1) 2) and 3) are re-iterated obtaining consecutively new couples of values of R_s and R_{sh} each of them following from different approximations of $I_D(V+IR_s)$ and, in turn, generating a new one.

This procedure gives a very good approximation of the values of R_s and R_{sh} and of the $I_D(V+IR_s)$ curve although, in principle, it cannot really converge to the "true" values. In fact, for each iteration, equation (5.2) fits the experimental *I-V* with some R_s and R_{sh} values evaluated in step 2) but the values of R_s and R_{sh} used in order to define $I_D(V+IR_s)$ are those determined in step 3) of the previous iteration. So the method is not self-consistent. Nevertheless, it has been found that after few iterations it provides quite good values of R_s and R_{sh} that are sufficiently exact in order to make the final step 4).

Step 4) A least square fitting procedure is employed to simultaneously evaluate both the parasitic resistances values and the parameters needed to define the function $I_D(V+IR_s)$. In this procedure, R_s and R_{sh} are varied searching for the best fit of equation (5.2) to the experimental *I-V* but using an $I_D(V+IR_s)$ expression obtained from the (I'_{sc}, V_{oc}) dataset generated by the same R_s and R_{sh} values.

This procedure easily converges because the initial values of R_s, R_{sh} and of the parameters related to $I_D(V+IR_s)$ have been previously obtained with good accuracy by the preceding iteration of the first three steps.

5.4 – APPLICATION TO SILICON PV CELLS

In order to test the novel method we have done *I-V* measurements by means of a PASANT CTSLAB 906 laboratory cell tester on two cells:

- #1: a 12.5x12.5 mono-crystalline silicon cell
- #2: a similar one but with a artificially worse shunt resistance.

Cell #2 has been adopted in order to experimentally test the case of a low quality cell for which assumption a) of paragraph 5.2 is surely not satisfied. For both cells irradiations between 600 and 1200W/m^2 have been performed and the corresponding *I-V* curves have been registered. With the purpose of having a larger (I_{sc}, V_{oc}) set, some neutral filters were also interposed between the lamp and the cell so to have some data even at irradiation power densities lower than 600W/m^2. The accuracy of both current and voltage measurements were ±0.2% with a minimum sensitivity of 2mA and 1mV respectively. In order to better explain the method we show, as an example, the result in the case of 800W/m^2 irradiation on cell #2.

The measured *I-V* characteristic for this case is shown as open dots in figure 5.1. I_{sc} and V_{oc} are 4.247± 0.008A and 0.571±0.002V respectively. The dashed straight lines are the tangents to the *I(V)* curve at V=0 and I=0, from which the first approximation of R_s=5mΩ and R_{sh}=0.4Ω are obtained by means of the "slope method" (step 0).

The experimental (I_{sc}, V_{oc}) dataset is reported in figure 5.2 as open squares.

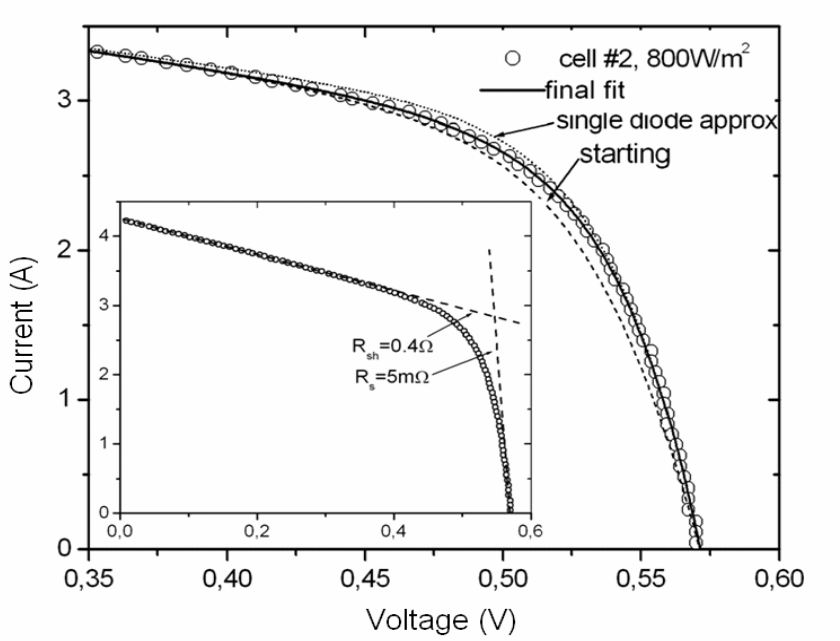

Figure 5.1 Circles: experimental characteristic of a (12.5x12.5)cm^2 crystalline Silicon PV cell (#2) with a very low shunt resistance irradiated with 800W/m^2 sun irradiance. Dashed curve (starting) is the first approximation used in the present method; full line (final fit): is the result of the last iteration of the procedure adopted in the present method assuming the double diode approximation; dotted curve: the same but assuming the single diode approximation. In the insert, the same characteristic in the full *I-V* scale. The dashed straight lines are the tangent to the end-points of the characteristic from which the first approximation for R_s and R_{sh} are derived.

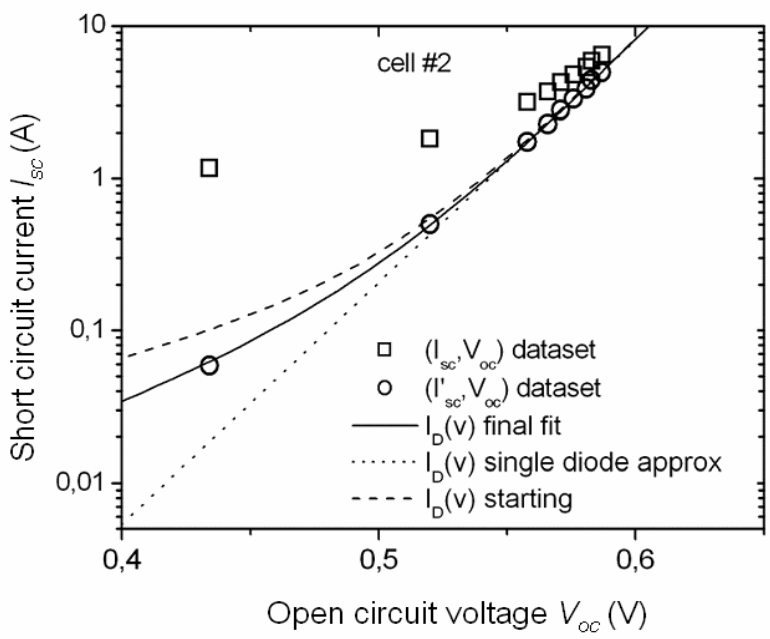

Figure 5.2 Symbols: plot of the short circuit currents (I_{sc}) versus the corresponding open circuit voltage V_{oc} obtained irradiating with several sun irradiances the same PV cell of figure 5.1. Squares: experimental data; circles: experimental data corrected following the last iteration of the procedure adopted in the present method.
Lines: reverse current of the cell (diode characteristic) calculated by the present method. Dashed curve (starting): is the first approximation used in the present method; full line (final fit): is the result of the last iteration of the procedure adopted in the present method assuming the double diode approximation; dotted curve (single diode approx.): the same but assuming the single diode approximation.

5.4.1- Double diode approximation

The first approximation of R_s=5mΩ and R_{sh}= 0.4Ω generates, using equations 5.7 and 5.8, the first $I_D(V+IR_s)$ approximation shown in figure (5.2) as a dashed line labelled "starting" (step 1). By using this approximation and the initial values of R_s and R_{sh}, equation (5.2) holds the result shown as a dashed line and labelled "starting" in figure 5.1. The sum of the squares of the difference between the computed curve and the experimental data is in this case S=1.29A^2. Proceeding to step 2, a new value of R_s(=1mΩ) and of R_{sh}(= 0.4Ω) are found which, in turn, give a new data set (I'_{sc},V_{oc}) (step 3). Iterating steps 1, 2 and 3 several times the consecutively obtained values of R_s, R_{sh} and S are reported as dark squares in figure 5.3a, 5.3b and 5.3c respectively as function of the iteration number. The values obtained by the last fit (step 4) are highlighted in

the same figures as dashed horizontal lines. They are: R_s=1.457mΩ, R_{sh}=0.389Ω and S=0.0493A^2.

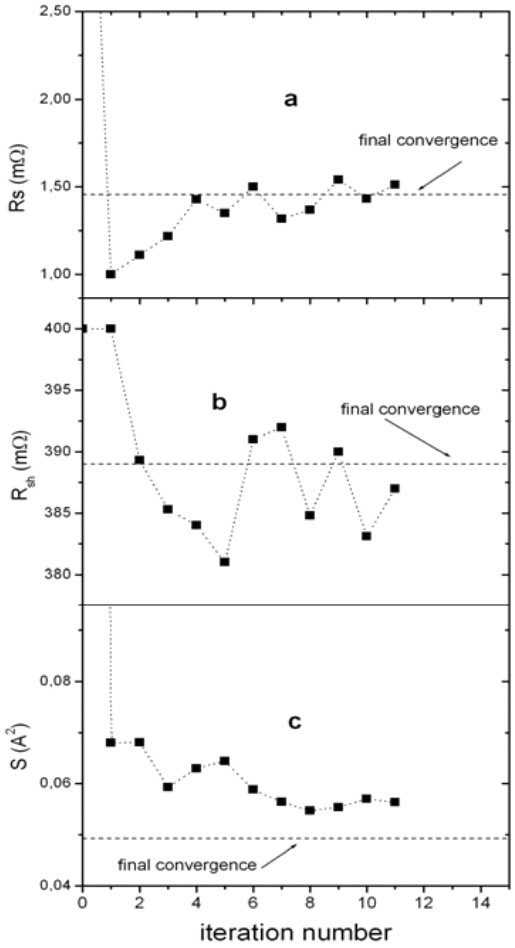

Figure 5.3 Values of series (a), shunt (b) resistances found in the various iteration of the procedure of the present method for the same cell of figures 5.1 and 5.2. The sum *S* of the squares of the differences between the experimental current values of the characteristic obtained with 800W/m^2 irradiance of figure 5.1 and the calculated ones are reported in (c). The initial values are represented by 0 as iteration number and, in the cases (a) and (c) are out of the scale. After 11 iterations the procedure is interrupted and the final step (step 4) of the procedure provides the result indicated as a horizontal dashed line in the figures.

In figure 5.2 the (I'_{sc},V_{oc}) dataset obtained by the last step 4 is reported as open dots and its fit obtained using the double diode approximation is reported as a full line labelled "final fit". In figure 5.1 the last calculation of the *I-V*

characteristic by equation (5.2) obtained in the step 4 is reported as a full line also labelled "final fit". It satisfactorily fit the experimental data. The errors in the R_s and R_{sh} values are not estimated within the fitting procedure but they are evaluated, as it will be shown, from the fluctuation of the data obtained by applying the procedure to different experimental dataset belonging to the same cell.

5.4.2 - Single diode approximation

In order to evaluate the relevance of the functional form adopted to describe $I_D(V+IR_s)$, the same procedure has been repeated on the same *I-V* characteristic, assuming the single diode approximation. The procedure yielded the final values R_s=1.75mΩ and R_{sh}=0.37Ω that is somewhat different from those obtained using the double diode approximation. The best fit of equation (5.2) to the experimental data is reported in figure 5.1 as a dotted line labelled "single diode approx" and in the same way also the final evaluation of $I_D(V+IR_s)$ is reported in figure (5.2). This last underestimates the real $I_D(V+IR_s)$ in the voltage region below 0.5V and, as a consequence, the computed *I-V* overestimates the experimental characteristic in the "knee" region between about 0.4 and 0.5V. The main reason of the discrepancy between the parasitic resistance values obtained by the single diode approximation and by the double diode approximation is just due to this difficulty to obtain a satisfactory fit of the experimental data in the "knee" region of the *I-V* curve. So it can be concluded that in the present method, a precise description of the diode characteristic is crucial in order to find correct values of the parasitic resistances.
However the single diode approximation can be also advantageously used in the case of a silicon PV cell, by using a partial set of experimental data, i.e. if the knee region of the characteristic is eliminated from the set of the *I-V* data to be fitted. In fact, the values of R_s and R_{sh} influence greatly the slope of the *I-V* characteristic in the regions near V_{oc} and near I_{sc} so that the use of the data around the knee region, although important if one want to detail $I_D(V+IR_s)$, are not so crucial for the purpose of evaluating the parasitic resistances values.

5.5 - RESULTS AND COMPARISON TO OTHER METHODS

All the *I-V* characteristics obtained at the various sun irradiations were analyzed following the method described in the previous paragraph.
In figure 5.4 the series resistance values obtained for cell #1 (triangles) and cell #2 (circles) are reported. The series resistances are equal, within the statistical fluctuations, between the two cells (as they must be being both cells coming from the some batch).

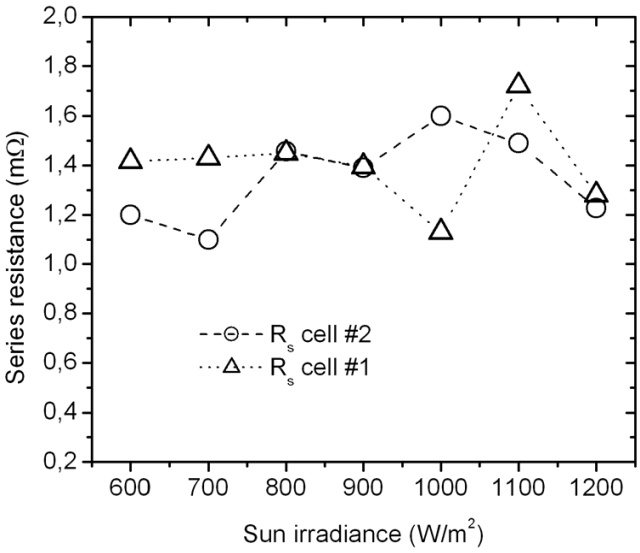

Figure 5.4 Values of series resistance obtained by the present method for the cell #2 and a similar one but with a much higher shunt resistance (#1), as function of the Sun irradiance used to get the analyzed characteristic.

The average values are R_s=1.37mΩ and R_s=1.35mΩ and the standard deviation of the measurements for the various irradiation are 0.24mΩ and 0.18mΩ for cell #1 and #2 respectively. Although the relative fluctuations of the R_s values may appear considerably large, it must be noted that the absolute error is very small: this method can even appreciate series resistance of the order of a fraction of one mΩ.
The shunt resistance values obtained by our procedure are reported in figure 5.5 upper part (triangles) for cell #1 and lower part (circles) for cell #2.

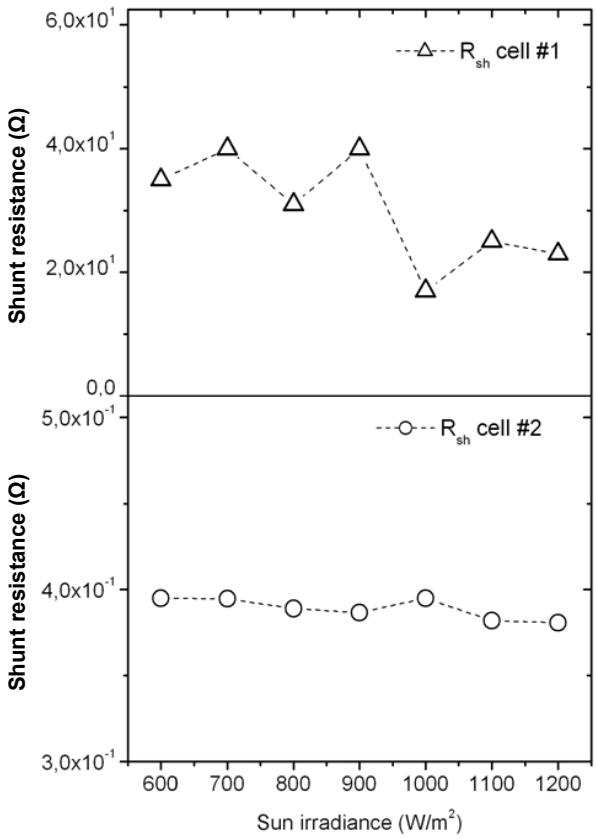

Figure 5.5 Values of shunt resistance obtained by the present method for the cell #2 and a similar one but with a much higher shunt resistance (#1), as function of the sun irradiance used to get the analyzed characteristic.

As expected, the shunt resistances are largely different between the two cells.
For cell #1 the average value is R_{sh}=30Ω and the standard deviation of all the measurements is 8.8Ω. This large error arises mainly from the fact that for so big values of shunt resistance the evaluation of the $I_D(V+IR_s)$ by means of equations (5.6) (5.7) and (5.8) is almost insensitive to the exact value of R_{sh} and the slope of the *I-V* characteristic in the region at high current values (which is the region more sensitive to the value of R_{sh}) is so small to be hardly measurable taking into account the fluctuation of the experimental points.
For cell #2, instead, the average value is R_{sh}=0.389Ω and the standard deviation of all the measurements is $6.18 \cdot 10^{-3}$Ω. In this case the relative error is much smaller because the fitting procedures are very sensitive to R_{sh} in this range of small values. The values of R_{sh} obtained by our method do not differ appreciably from those obtained with the other standard methods investigated, for this reason we will concentrate our attention only to the results obtained for R_s.

Two important features are evident, on looking the data of figure 5.4 and 5.5: first, despite the large difference for the shunt resistance values, the method provides the same series resistance value for both cells. Second, the values of the series resistances are measured with good accuracy although they are considerably small. In order to put in evidence the importance of these two features, some comparison with other standard methods will be shown.
Firstly the standard method recommended by I.E.C. has been used. In this method a point of a certain *I-V* characteristic is chosen, so that its I_1 value is below the maximum current I_{sc} of a fixed amount. A corresponding point in another characteristic, obtained at different sun irradiance, is chosen so to have an I_2 value below its corresponding I_{sc} of the same amount. Being V_2 and V_1 the related voltages, assuming $R_{sh}>>R_s$, it follows from equation (5.2) that $R_s=(V_2-V_1)/(I_2-I_1)$.
The I.E.C. method has been applied choosing several pairs of characteristic belonging to the same cell in the range between 600 and 1200W/m^2 irradiance. For each chosen pair the obtained R_s value is shown in figure 5.6 for cell #1 (triangles) and cell #2 (circles) as function of the average of the two sun irradiances in the pair.

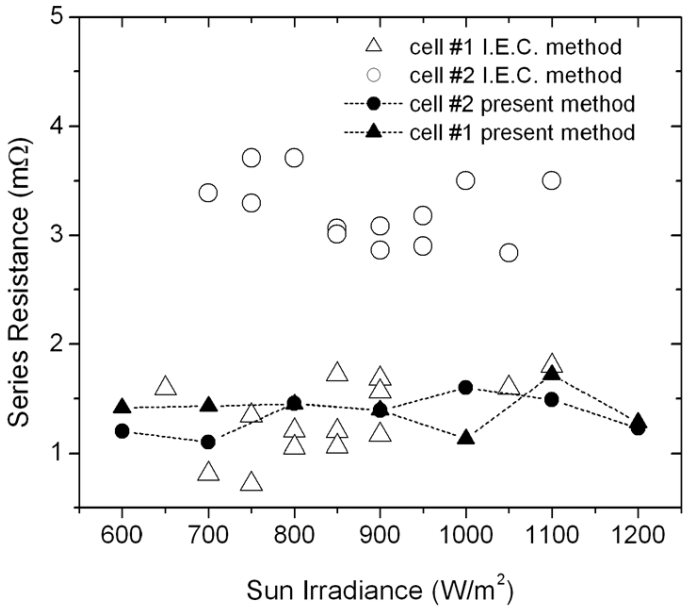

Figure 5.6 Full symbols: values of series resistance obtained by the present method for the same cell #2 and a similar one but with a much higher shunt resistance (#1), versus the Sun irradiance used to get the analyzed characteristic. Open symbols: The same but using the procedure recommended by the International Electrotechnical Commission (I.E.C.). In this last case the sun irradiance value reported is the average between the two characteristics used for the series resistance determination.

The average value obtained for all the pairs is R_s=1.29mΩ with a standard deviation of 0.36mΩ and R_s=3.6mΩ with a standard deviation of 0.7mΩ for cell #1 and for cell #2 respectively. For comparison, in the same picture the data of figure 5.6 obtained for our sample are also reported with full symbols. It is evident that the I.E.C. method gives a value reasonably close to that one obtained by the present method only for cell #1. In fact, for the cell with the low shunt resistance, it gives an incorrect value since, as said, the two cells must have the same series resistance. Moreover, also the precision of the I.E.C. method is rather worse since the standard deviation of the measurements is about a factor of two or three larger than those obtained with present method.
Obtained results could be compared to those obtained by the derivative method and its implementation due to Ishibashi et.al. [4].
The derivative *dI/dV* of the *I-V* curves has been computed by the five points method after an initial smoothing of the experimental data. As an example in figure 5.7 *(dI/dV)-1* is reported versus $(I_{sc}–I)$*-1* for the case of cell #1 irradiated at 800W/m^2.

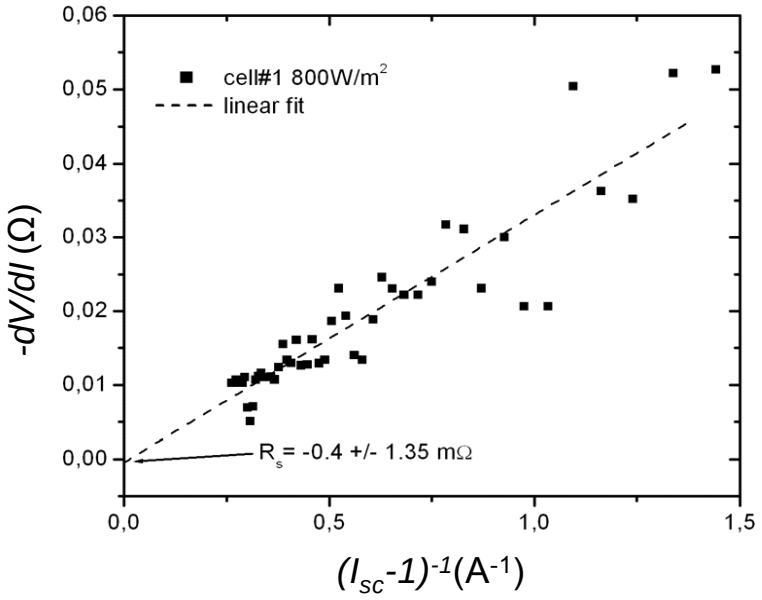

Figure 5.7 The inverse of the derivative of the *I-V* characteristic of (12.5x12.5)cm^2 Silicon polycrystalline solar cell with a high value shunt resistance (#1) irradiated with 800W/m^2 sun irradiance plotted vs. the inverse of the difference between the short circuit current and the current *I*. The full squares are obtained using the five points method on the experimental data, the dashed line is the linear fit of the plot.

The linear best fit of the data gives an intercept value R_s=-0.4±1.35mΩ. So, large error and the unrealistic negative value of the series resistance found are obviously due to the large fluctuations of the computed derivative points which are a consequence of the experimental uncertainties of the voltage and current measurements.
These analyses have been repeated to all the measured characteristics and the resulting series resistance values and the corresponding errors are reported in the following figure 5.8 as open squares. The average of all the obtained R_s values is 2mΩ and the standard deviation is 3.54mΩ. For comparison, in the same figure 5.8 the data obtained with present method (the same that have been reported in figure 5.4) are reported as full dots.

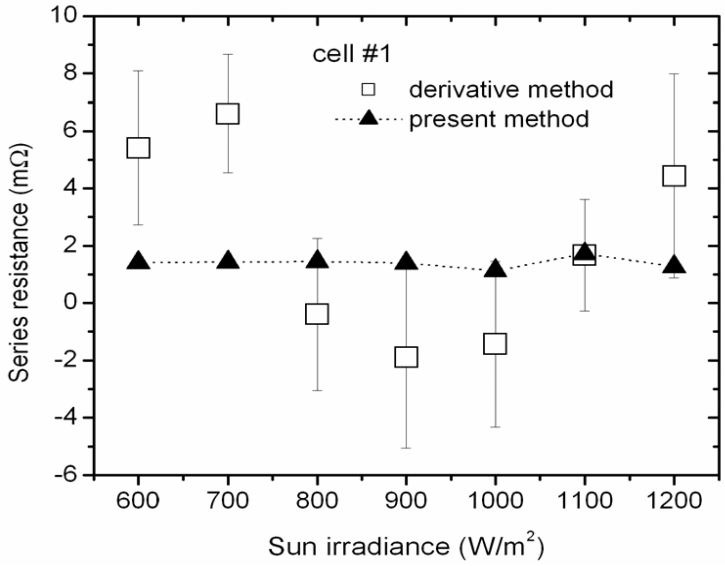

Figure 5.8 Squares: Series resistances values obtained for the same cell of fig. 8 as function of the sun irradiance of the analyzed characteristic obtained by the derivative method. Triangles: the same but obtained by the present method.

Despite the great data dispersion, the average value is still consistent with the one found by present method and the I.E.C. method, but the large error in the single measurement makes the derivative method unsuitable for the analysis of the present data. Following the Ishibashi [4] improvement of the derivative method, similar results have been found for cell #2, while R_{sh} values are evaluated quite satisfactorily.
We have estimated that in order to obtain an accuracy similar to that one obtained by novel present method (standard deviation of the order of few $10^{-4}\Omega$) the accuracy in the voltage measurement in the *I-V* curve must be of the order of few 10^{-4}V (instead of some mV of the present experimental case). It has been

also tried to obtain less dispersion in the data of the derivative *dI/dV* by fitting a polynomial function to the experimental *I-V* curve and then performing the derivative, as suggested in the Ishibashi paper [4]. Although in this case the data fluctuation becomes negligible, we found a large dependence of the result on the chose of the polynomial degree. Moreover, with this procedure, the final plot of *(dI/dV)* versus $(I_{sc}-I)-1$, is not a real straight line, posing severe difficulties in the linear extrapolation of the curve for the determination of R_s at the ordinate axis intercept.

References

[1] Aldert van der Ziel, *Solid State Physical Electronics*, Nick Holonyak ed. Prentice Hall Inc. Electrical Engineers Series 3th ed. N.J. USA (1976).

[2] Ken-ichi Kurabe and Hiroyuki Matsunami , Jpn. J. Appl. Phys. **44**, 8314 (2005).

[3] I.E.C. - International Electrotechnical Commission, *Procedures for Temperature and Irradiance Corrections to Measured I-V Characteristics of Crystalline Silicon Photovoltaic Devices*, 60891 (1992).

[4] Ken-ichi Ishibasi, Yasuo Kimura and Michio Niwano, J. Appl. Phys. 103, 094597 (2008).

[5] T. Easwarakhanthan, J. Bottin, I. Bouhouch, and C. Boutrit, Int. J. Sol.Energy **4**, 1 (1986).

[6] M. Chegaar, Z. Ouennouchi, and A. Hoffmann, Solid-State Electron. **45**,293 (2001).

[7] A. Kaminski, J. J. Marchand, and A. Laugier, Solid-State Electron. **43**,741 (1999).

[8] M. Murayama and T. Mori, Jpn. J. Appl. Phys., Part 1 **45**, 542 (2006).

[9] M. Murayama and T. Mori, *Thin Solid Films* 509, 123 (2006).

Summary and Conclusions

This thesis gives, at first, a collocation of photovoltaic technology inside the picture of world energy production. The need of a transition to a renewables-intensive energy market is reported as a scientific evidence deriving from economical and environmental data analysis. The present state-of-art of photovoltaic technology in terms of research development, manufacturing cost, market status and forecast is illustrated.

In spite of emerging new technologies promising higher efficiencies and lower production costs, standard first generation devices (single junction, silicon wafer-based cells) still represent the majority of available photovoltaic equipments because of their cost-effectiveness. However, the necessity to produce more and more competitive photovoltaic cells requires a continuous progress regarding cell design in order to optimize structural parameter toward efficiency improvement and cost reduction. A complete study of all structural parameters characterizing silicon wafer-based photovoltaic cells has been performed by means of a simulation program purposely realized. The simulation program has been used to analyze the most important physical and geometrical factors determining silicon cells performance (as material quality, doping levels, layers thickness) with the purpose of maximize photogeneration and minimize electrical losses. Obtained results quantify the effect of semiconductor quality demonstrating that most effectiveness silicon (in terms of costs/benefits ratio) is the typical Czochralski-grown. It has been also illustrated that best performances could be obtained for an emitter as thin as possible (in the order of few thousands of nanometres) and heavily doped (doping concentration $>10^{18}cm^{-3}$). Moreover, has been shown that base thicknesses in the range of 200÷300μm and doping levels within the interval $10^{15}\div10^{16}cm^{-3}$ optimize bulk design guaranteeing highest efficiencies. Finally, simulations highlight the importance of parasitic resistance effects on device electrical characteristic influencing drastically cell performance.

Simulations results have been used inside an industrial R&D project arisen from a collaboration between Meridionale Impianti (M.I.) S.p.A., UniCt (Catania's University), Advanced Technology Solutions (A.T.S.) S.r.l. and Meridionale Impianti Welding Technology (M.I.W.T) S.r.l.. The project purpose was the development of innovative processes and new equipments aimed at production of high efficiency and low-costs first generation silicon photovoltaic cells. It included a pre-competitive development and an industrial research. Thus, the entire industrial standard process used for realize a silicon PV cell has been studied and a revision of every single manufacturing step has been carried out in order to attain a competitive manufacturing line. Data obtained by research and simulation activities have allowed to create a prototype productive line, designed with the principle purposes of product quality, manufacturing cost reduction and energy saving.

The main innovation introduced regards the use of a ZnO film deposited by a Pulsed Plasma Deposition method (PPD) as both front contact and passivation layer. Optical and electrical characteristics of the deposited layer have been studied to define best process equipment set up and to optimize film thickness. The effects of the ZnO layer on photovoltaic cell electrical behavior (connected especially to the diminishing of parasitic series resistance value) have been evaluated by the comparison of two prototype cells. It has been demonstrated that innovative process flow with ZnO could improve cell efficiency. Moreover, obtained results highlight the importance of the innovative technique investigated since it is very advantageous because also simplify entire PV cell process flow. ZnO deposition performed by PPD developed inside present project opens interesting prospects in the sphere of process flow simplification and it necessities of a dedicated industrialization program directed towards large scale production.

The difficulties occurred during the estimation of low series resistances (in the order of few mΩ), in terms of accuracy and repeatability, using standard measurement methods yielded to the development of a new measurement procedure in order to overcome the intrinsic limits of other methods.

The presented method does not make use of any particular assumption, so that it can be virtually used for any kind of cell. It is very precise, since it is able to evaluate with good precision and reproducibility series resistance values as low as 1mΩ if the precision of voltage and current measurements in the cell characteristic is of the order of few mV and mA respectively. Moreover the measure of the series resistance is not precluded or made difficult by the presence of a low value shunt resistance. These two facts represent themselves a large improvement of the capabilities and potentialities on respect of the other nowadays used methods.

In conclusion, in the present thesis work, I have highlighted the relevance of conventional silicon technology based solar cell in the world economic scenario and I have described a real pre-industrial production line, locally developed, pointing out some crucial points on the way of making photovoltaic electrical energy production economically competitive with fossil-produced electricity.